

DTIC FILE COPY

2

**RADC-TR-90-377
Final Technical Report
December 1990**



AD-A232 125

**SCATTERING FROM THIN APERTURES IN
COATED CONDUCTORS USING FDTD**

University of Kansas

Kenneth R. Demarest and Panayiotis A. Tirkas

**DTIC
ELECTE
MAR 6 1991
S D D**

APPROVED FOR PUBLIC RELEASE; DISTRIBUTION UNLIMITED.

**Rome Air Development Center
Air Force Systems Command
Griffiss Air Force Base, NY 13441-5700**

91 2 28 069

This report has been reviewed by the RADC Public Affairs Division (PA) and is releasable to the National Technical Information Service (NTIS). At NTIS it will be releasable to the general public, including foreign nations.

RADC-TR-90-377 has been reviewed and is approved for publication.

APPROVED:



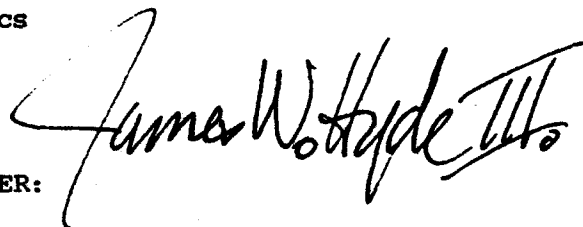
KEITH D. TROTT, Maj, USAF
Project Engineer

APPROVED:



JOHN K. SCHINDLER
Director of Electromagnetics

FOR THE COMMANDER:



JAMES W. HYDE III
Directorate of Plans & Programs

If your address has changed or if you wish to be removed from the RADC mailing list, or if the addressee is no longer employed by your organization, please notify RADC (EECT) Hanscom AFB MA 01731-5000. This will assist us in maintaining a current mailing list.

Do not return copies of this report unless contractual obligations or notices on a specific document require that it be returned.

REPORT DOCUMENTATION PAGE

Form Approved
OMB No. 0704-0188

Public reporting burden for this collection of information is estimated to average 1 hour per response, including the time for reviewing instructions, searching existing data sources, gathering and maintaining the data needed, and completing and reviewing the collection of information. Send comments regarding this burden estimate or any other aspect of this collection of information, including suggestions for reducing this burden, to Washington Headquarters Service, Directorate for Information Operations and Reports, 1215 Jefferson Davis Highway, Suite 1204, Arlington, VA 22202-4302, and to the Office of Management and Budget, Paperwork Reduction Project (0704-0188), Washington, DC 20503.

1. AGENCY USE ONLY (Leave Blank)		2. REPORT DATE December 1990		3. REPORT TYPE AND DATES COVERED Final Jun 88 to Sep 89	
4. TITLE AND SUBTITLE SCATTERING FROM THIN APERTURES IN COATED CONDUCTORS USING FDTD				5. FUNDING NUMBERS C - F30602-88-D-0027 PE - 61102F PR - 2305 TA - J4 WU - P4	
6. AUTHOR(S) Kenneth R. Demarest, Panayiotis A. Tirkas					
7. PERFORMING ORGANIZATION NAME(S) AND ADDRESS(ES) University of Kansas Radar Systems and Remote Sensing Lab 2291 Irving Hill Drive Lawrence KS 66045-2969				8. PERFORMING ORGANIZATION REPORT NUMBER	
9. SPONSORING/MONITORING AGENCY NAME(S) AND ADDRESS(ES) Rome Air Development Center (EECT) Hanscom AFB MA 01731-5000				10. SPONSORING/MONITORING AGENCY REPORT NUMBER RADC-TR-90-377	
11. SUPPLEMENTARY NOTES RADC Project Engineer: Keith D. Trott, Maj, USAF/EECT/(617) 377-4239					
12a. DISTRIBUTION/AVAILABILITY STATEMENT Approved for public release; distribution unlimited				12b. DISTRIBUTION CODE	
13. ABSTRACT (Maximum 200 words) The Finite-Difference Time-Domain (FDTD) technique is applied to scattering problems involving thin dielectric sheets, conductor-backed dielectric sheets and conductor-backed dielectric sheets containing cracks in the dielectric coating. The FDTD technique is first applied in a "brute force" method to solve the scattering problems. Then, coarse cells are used whereby the dimensions of the scatterer can be smaller than the dimensions of the FDTD unit cell. This approach, referred to as the "thin equation" approach, is computationally more efficient than the "brute force" method. Numerical results are shown in the frequency domain. Specifically, radar cross section (RCS) and near-field results obtained using a two-dimensional FDTD code are presented.					
14. SUBJECT TERMS FDTD Numerical Methods Scattering Cracks Gaps				15. NUMBER OF PAGES 100	
				16. PRICE CODE	
17. SECURITY CLASSIFICATION OF REPORT UNCLASSIFIED		18. SECURITY CLASSIFICATION OF THIS PAGE UNCLASSIFIED		19. SECURITY CLASSIFICATION OF ABSTRACT UNCLASSIFIED	
				20. LIMITATION OF ABSTRACT SAR'	

CONTENTS

	Executive Summary	1
1	Introduction	3
2	Review of FDTD Technique	5
	2.1 Yee's Formulation	5
	2.2 Integral Equation Approach	6
	2.3 Features of Present FDTD Codes	8
	2.4 Limitations of the FDTD Technique	10
3	Near-Field to Far-Field Transformations	12
	3.1 Introduction	12
	3.2 Two-Dimensional Transformation	13
	3.2.1 Application to TM Polarization	15
	3.2.2 Application to TE Polarization	17
	3.3 Three-dimensional Transformation	19
	3.4 Amplitude and Phase Estimation	20
	3.5 2-D Numerical Results	22
4	Modeling of Dielectric Structures	25
	4.1 Numerical Techniques Applied to Dielectrics	25
	4.2 Application of FDTD to Dielectric Structures	26
	4.3 Modifications for Thin Dielectric Slabs	28
	4.4 Numerical Results	31
5	Modeling of Conductor-Backed Dielectric Sheets	43
	5.1 Introduction	43
	5.2 Brute Force Method	43
	5.3 Thin Conductor-Backed Dielectric Sheets	44
	5.4 Numerical Results	47
6	Conductor-Backed Dielectrics With Cracks	57
	6.1 Introduction	57
	6.2 Brute Force Modeling of 2-D Cracks	57
	6.3 Two-Dimensional Thin Crack Model	63
	6.4 Three-Dimensional Thin Crack Model	78
7	Conclusions	83
	Appendix	85
	References	89

Executive Summary
by
Kenneth R. Demarest, Principal Investigator

This final report describes the findings of our group during the contract period 6/2/88 through 8/30/89 under contract F30602-88-D-0027, Task Assignment No. E-8-7051. The purpose of this contract was to develop analytical and numerical techniques capable of predicting the electromagnetic scattering characteristics of conductor-backed dielectric sheets containing cracks in the dielectric. The method chosen was the Finite-Difference Time-Domain (FDTD) technique. This choice was based on the well known attractive characteristics of this technique, particularly when dealing with arbitrarily shaped, dielectric structures.

The major effort during the contract period was to extend the FDTD technique to efficiently model very thin conductor backed dielectric sheets, with and without cracks. Although the standard FDTD technique can, in theory, model such sheets of all thicknesses, it becomes increasingly unattractive for very thin sheets since the spatial grid size must be made small enough to fully resolve the geometry being modeled. In order to efficiently model fractional wavelength dielectric coatings and cracks, augmentations to the standard FDTD technique must be made.

The modeling philosophy adopted to address this problem was to develop models that would allow relatively large spatial cells to be used. To do this, the near field characteristics of the thin sheets and the cracks would be built into those cells that contain them, thus allowing these cells to be considerably larger than the sheets and cracks themselves. This philosophy is an outgrowth of the integral equation view of FDTD [1].

The models for large cells containing dielectric sheets and conductor-backed dielectric sheets were initiated in a previous RADC contract: No. F30602-81-C-0205, task number E-7-7064 [2]. These models were then incorporated in a standard FDTD code and tested to establish their validity. Comparisons of the large cell FDTD results, both for two- and three-dimensional slabs, with physical optics and the method of moments established that the large cell approach is accurate and numerically efficient [3,4].

With the large cell approach for dielectric and conductor-backed dielectric sheets thus established, the work was able to proceed to the development of large cell techniques for conductor-backed dielectric slabs containing cracks. This extension represented the most challenging aspect of the contracted work, since the fields in the vicinity of a dielectric discontinuity are highly nonlinear and not as well known as for perfectly conducting geometries.



A-1

J

des
of

backed dielectric slabs containing cracks. This extension represented the most challenging aspect of the contracted work, since the fields in the vicinity of a dielectric discontinuity are highly nonlinear and not as well known as for perfectly conducting geometries.

It was very quickly realized that the thin crack model developed in [2] is not fully capable of representing the fields in the region just outside the crack region, and thus not capable of correctly predicting the response of the crack in an FDTD code. Fortunately, the very simulations that exposed this flaw also pointed the way to the development of a more rigorous model. This technique was implemented in our FDTD code for two dimensional geometries and showed excellent agreement with "brute force" FDTD simulations, but at a fraction of the computational cost.

Two FDTD computer codes were developed under this contract — one for two-dimensional scatters [31] and one for three-dimensional scatters [5]. Both codes are similar in structure, but the two-dimensional code is more fully developed from the standpoint of the thin-dielectric scattering of interest in this contract. The following table summarizes the capabilities of the two codes,

	2-D Code	3-D Code
Full cell conductors	✓	✓
Full cell lossy dielectrics	✓	
Thin conductor-backed dielectrics	✓	✓
Thin cracks	✓	
Arbitrary plane wave incidence	✓	✓
Far-field results	✓(steady-state)	✓(transient)

This technical report to follow describes in detail the modeling philosophy used to address the problem of scattering from thin dielectric coatings on conducting surfaces, with and without cracks. It consists of four major components. In the first, the finite-difference time-domain (FDTD) technique is reviewed, with particular emphasis on the "smart cell" philosophy of modeling fine detail. This is followed by three sections that present the modeling details and results for the three geometries of interest: thin dielectric slabs, thin conductor backed dielectric slabs, and thin conductor backed dielectric slabs with cracks. In each of these sections, numerous results are given and each compared with other techniques to establish the limits of their models.

Chapter 1: Introduction

Recent advances in aircraft and radar technology have given rise to changes in aircraft construction. Such changes include the use of dielectric structures inside and outside the aircraft, replacing metal structures which have been traditionally used. The impetus for the use of these materials often stems from their desirable mechanical properties (high strength, low weight, etc.), as well as possible reductions in radar cross section. The analysis of the electromagnetic scattering properties of such dielectric structures is the subject in this report.

A dielectric structure of interest is the thin dielectric sheet. A thin dielectric sheet can either be free standing or conductor-backed. The former can be used in aerodynamic control surfaces such as fins, whereas the latter can be used in fuselage construction using thin, conductor-backed, dielectric panels.

A challenging problem of particular interest in this study involves scattering from conductor-backed dielectric structures that contain slots or cracks in the dielectric material. Such structures are difficult to model because they combine two different problems- the volume scattering of the dielectric and the nonlinear field behavior near the sharp discontinuities of the crack. In spite of the importance of this particular structure, little progress has been made in the development of analytical or numerical solutions of its scattering properties.

Two techniques that have been used to solve problems involving dielectric structures are the Method of Moments (MoM) [7], and the Finite-Difference Time-Domain technique (FDTD) [8]. Both techniques have proved very successful, and both have their drawbacks. It has recently been shown that the FDTD technique has certain advantages over the MoM when dielectrics are involved [9]. For example, while FDTD allows accurate modeling of dielectric structures without requiring very accurate air-dielectric boundary specifications, the MoM does not. Other advantages of the FDTD technique over the MoM stem from the overall savings in the number of computer operations required in order to solve a given electrical problem.

The FDTD technique has recently been advanced so that a wide range of geometries can be modeled. Kunz and Simpson [10] developed a technique to increase the resolution of the FDTD technique by introducing a finer subgrid model. Taflov and Umashankar [1] introduced the integral equation approach in the FDTD technique, in which detailed analysis of the electromagnetic fields penetrating narrow slots and lapped joints can be performed. Demarest [11] used the FDTD technique to model narrow apertures in conducting scatterers, whereas Holland and

Simpson [12] applied the FDTD technique to analyze electromagnetic pulse coupling to thin struts and wires.

One of the major objectives of this study is to further develop the FDTD technique to allow modeling of thin dielectric structures (free standing, conductor-backed, and conductor-backed containing dielectric cracks). Before attempting to do this, a brief overview of the FDTD technique is given in Chapter 2. This overview includes some recent advances, limitations, and controversial issues in FDTD applications and techniques.

Chapter 3 deals with the implementation of a near-field to far-field transformation. This transformation allows the estimation of the far-field response and radar cross section (RCS) of the structures under consideration. The amplitude and phase information required by this transformation is obtained using a least squares estimation method.

In Chapter 4, it is shown how the FDTD technique can be applied to solve scattering problems containing dielectric sheets. The modifications required to allow modeling of thin dielectric sheets of thickness less than the cell size of the FDTD grid are also considered. Chapter 4 is concluded with some radar cross section results obtained from dielectric sheets.

Chapter 5 deals with the modeling of conductor-backed dielectric structures. This modeling is done initially by using very small cells to model the thin dielectric coating on top of the perfect conductor, and then extended to cover modeling using cell sizes much larger than the dielectric thickness. Numerical results obtained from both methods are compared to test the validity of the thin structure model.

Chapter 6 is introduced with a study of the near-field physics of dielectric cracks using a very fine resolution FDTD grid. The results of this study are used to verify a simple formulation of the fields above a dielectric crack for a coarse FDTD code. This approach is applied initially to two-dimensional problems and, once its validity is established, is extended to apply to three-dimensional problems. Finally, some numerical examples are given for both cases.

Chapter 7 summarizes the results and conclusions of this report. Possible applications of this study are also discussed. An appendix and a list of references is included at the end.

Chapter 2: Review of the FDTD Technique

2.1 Yee's Formulation

The FDTD technique was first introduced to the electromagnetic community by Yee [8]. This is a popular technique that solves Maxwell's time-dependent curl equations by converting them to difference equations and applying the proper boundary conditions. Maxwell's equations in an isotropic medium are

$$\frac{\partial \mathbf{B}}{\partial t} + \nabla \times \mathbf{E} = 0 \quad (2.1a)$$

$$\frac{\partial \mathbf{D}}{\partial t} - \nabla \times \mathbf{H} = -\mathbf{J} \quad (2.1b)$$

$$\mathbf{D} = \epsilon \mathbf{E} \quad (2.1c)$$

$$\mathbf{B} = \mu \mathbf{H} \quad (2.1d)$$

where \mathbf{E} is the electric field in volts/meter, \mathbf{H} is the magnetic field in amperes/meter, \mathbf{J} is the current density in amperes/meter², ϵ is the electrical permittivity in farads/meter, and μ is the magnetic permeability in henrys/meter. \mathbf{E} , \mathbf{H} , \mathbf{J} , μ , and ϵ are assumed to be given functions of space and time. In a rectangular coordinate system equations (2.1a) and (2.1b) can be converted into a set of scalar differential equations and, by using a central difference scheme, converted to a set of difference equations. With this approach the continuous electromagnetic fields in a finite volume of space are sampled at specific points in space and time. The electric and magnetic fields are interlaced in both time and space.

In two-dimensional problems it is assumed that the field values do not depend on the z coordinate of a point, so the partial derivatives of the fields with respect to z are zero. It is also customary to decompose any electromagnetic field into Transverse Electric (TE) and Transverse Magnetic (TM) wave modes and analyze each mode separately. TE and TM modes are defined with respect to the infinite dimension of the scatterer, i.e, they are transverse to z . These two modes are characterized by [8]:

1) Transverse Electric (TE)

$$H_x = H_y = 0, E_z = 0,$$

$$-\mu \frac{\partial H_z}{\partial t} = \frac{\partial E_y}{\partial x} - \frac{\partial E_x}{\partial y},$$

$$\frac{\partial H_z}{\partial y} = \epsilon \frac{\partial E_x}{\partial t}, \quad -\frac{\partial H_z}{\partial x} = \epsilon \frac{\partial E_y}{\partial t} \quad (2.2)$$

and

2) Transverse Magnetic (TM)

$$E_x = E_y = 0, H_z = 0,$$

$$\epsilon \frac{\partial E_z}{\partial t} = \frac{\partial H_y}{\partial x} - \frac{\partial H_x}{\partial y},$$

$$\mu \frac{\partial H_x}{\partial t} = -\frac{\partial E_z}{\partial y}, \quad \mu \frac{\partial H_y}{\partial t} = \frac{\partial E_z}{\partial x} \quad (2.3)$$

Equations (2.2) and (2.3) can easily be converted into difference equations using central differencing. The resulting equations can be applied over an FDTD grid to model scattering by two-dimensional structures.

Wave propagation is modeled by advancing the electric and magnetic fields at equally spaced points in time. Scattering is modeled by imposing the proper boundary conditions on the surface of the scatterer.

2.2 Integral Equation Approach

It has been shown [1] that a more effective view of FDTD technique is obtained by starting with the integral form of Maxwell's time-dependent equations and applying them over small surfaces of the solution space. In integral form, Maxwell's equations can be stated as:

$$\oint_C \mathbf{H} \cdot d\mathbf{l} = I + \frac{\partial}{\partial t} \int_S \epsilon \mathbf{E} \cdot d\mathbf{S} \quad (2.4a)$$

$$\oint_C \mathbf{E} \cdot d\mathbf{l} = -\frac{\partial}{\partial t} \int_S \boldsymbol{\mu} \cdot d\mathbf{S} \quad (2.4b)$$

where equation (2.4a) is referred to as Ampere's law and equation (2.4b) as Faraday's law.

The FDTD approach proceeds to solve for the electric and magnetic fields resulting from a particular incident field (or source) interacting with a scatterer by dividing both time and space into a numerical grid as in the Yee approach. A planar cut of a three-dimensional FDTD grid showing the integral contours used for advancing the electric and magnetic fields is shown in figure 2.1.

If the cell under consideration contains only homogeneous media, the evaluation of equations (2.4a) and (2.4b) proceeds by assuming that the dimensions of the cell are small enough (less than 1/10) in each direction so that the electric and magnetic fields can be considered linear functions of position. Under these assumptions, it is shown in [2] that the resulting equations for advancing the electric and magnetic fields are exactly the same as those obtained by applying Yee's approach.

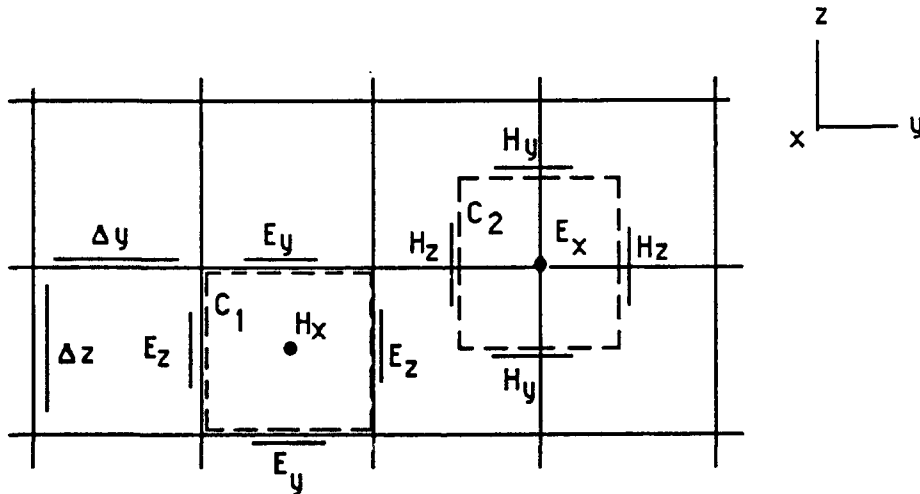


Figure 2.1 FDTD grid showing the integral contours for advancing the x-directed electric and magnetic fields in homogeneous media.

Application of Faraday's law over contour C_1 (see figure 2.1) results in the following equation for advancing the x-directed magnetic field in homogeneous material:

$$H_x^{n+1/2}(I,J,K) = H_x^{n+1/2}(I,J,K) + \frac{\Delta t}{\mu} \left\{ \frac{1}{\Delta y} [E_z^n(I,J,K) - E_z^n(I,J,K)] + \frac{1}{\Delta z} [E_y^n(I,J,K) - E_y^n(I,J,K)] \right\} \quad (2.5)$$

where the I, J, K indices indicate that the field point is associated with the I, J, Kth cell. Δy and Δz are the unit cell dimensions in the y and z direction respectively and Δt is the time increment. The superscripts $(n+1/2)$, $(n-1/2)$, and n indicate that the field under consideration is evaluated at time $t=(n+1/2)\Delta t$, $t=(n-1/2)\Delta t$, and $t=n\Delta t$ respectively.

Once the values of the magnetic fields at time $t=(n+1/2)\Delta t$ have been updated in each cell, an application of Ampere's law in each cell yields the electric fields at $t=(n+1)\Delta t$. A representative expression for advancing an x-directed electric field in a cell containing only homogeneous material and no currents is

$$E_x^{n+1}(I,J,K) = E_x^{n+1}(I,J,K) - \frac{\Delta t}{\epsilon} \frac{1}{\Delta y} \left\{ H_z^{n+1/2}(I,J,K) - H_z^{n+1/2}(I,J,K) + \frac{1}{\Delta z} \left[H_y^{n+1/2}(I,J,K) - H_y^{n+1/2}(I,J,K) \right] \right\} \quad (2.6)$$

Similar equations for the other four components of the electric and magnetic fields can be derived following the same procedures.

2.3 Features of Current FDTD Codes

The FDTD technique, whether applied to two-dimensional or three-dimensional structures, sequentially evaluates the magnetic fields over the entire solution space, and then the electric fields at half-time steps. This process is repeated for many time steps. In this way, time marching solutions to electromagnetic scattering problems are obtained.

Because no computer can store an unlimited amount of data, the computation zone of the FDTD technique must be limited in size, but still large enough to enclose the target of interest. To close off the outer boundary of the computation zone, the FDTD technique must employ a radiation boundary condition (RBC) to simulate the field sampling space extending to infinity by suppressing reflections off the outer boundary. At present the most commonly used RBC is the second order technique developed by Mur [13], utilizing the wave equation in cartesian coordinates. A similar RBC can be obtained by utilizing the dispersion relation for the one-way wave equation [14]. Having an efficient RBC in the FDTD code results in a lower computational noise floor because of the reduced reflections from the outer boundary. An efficient RBC also increases the modeling dynamic range which is important for certain classes of scatterers, like dielectric structures.

The total solution space is often divided into two regions. The first one is the total field region where the modeled structure is embedded, and where total (incident + scattered) electric and magnetic fields are time stepped. The second one is a scattered field region which surrounds the total field region. Here, only scattered electric and magnetic fields are time stepped. One benefit of this scheme is that a connecting condition between the total field and the scattered field regions allows the generation of an arbitrary incident plane wave having a user specified time waveform, angle of incidence, and polarization [14]. This field region zoning has been found to provide three more basic advantages [14]:

- 1) wide computational dynamic range,
- 2) simple programming of dielectric structures, and
- 3) far-field response.

A wide computational dynamic range is obtained because low field levels within cavities (i.e, metal, conductor-backed dielectric cracks) or deep shadows can be computed directly in total field regions. These low level fields are not contaminated by noise subtraction, as in scattered-field type codes, resulting from relatively large incident and scattered field components.

Another benefit of the use of separate total field and scattered field regions is encountered when modeling dielectrics. This is because when the dielectric is located within a total field region, the code does not have to calculate the incident field at all points within the dielectric.

Finally, providing a scattered field region allows the location of a scattered-field virtual surface, which is required for the near-field to far-field transformation. A virtual surface between the total-field/scattered-field boundary and the outer boundary is chosen on which the equivalence principle is applied to achieve this transformation. A detailed explanation of the near-field to far-field transformation will be given in chapter 3.

A pictorial representation of the outer boundary, the total-field/scattered-field boundary, and the virtual surface on which the equivalence principle is applied, is illustrated in figure 2.2. The total-field and scattered-field regions are also shown in the following figure.

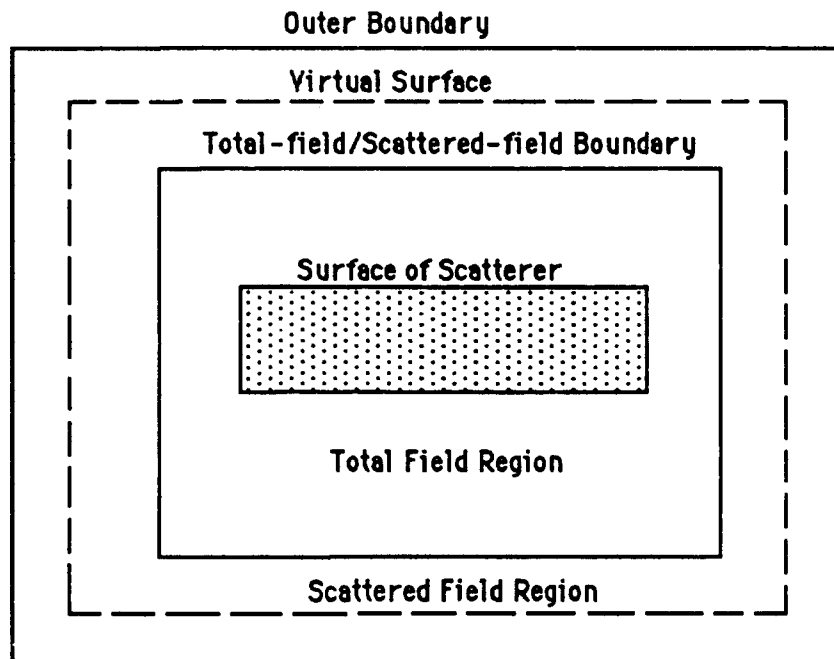


Figure 2.2 Zoning of the problem space in FDTD technique

2.4 Limitations of the FDTD Technique

FDTD is an established technique for modeling complex scatterers both in the frequency and time domain. In spite of its success, however, the method also has its weaknesses. One such weakness is its relative inability to model geometries that are both electrically large and yet contain fine details. Such details could include sharp points, small apertures, and thin dielectric sheets. Small substructures such as these cause problems with the FDTD technique because the fields in the vicinity of these objects exhibit rapid spatial variations.

Although fine detail can be modeled by using a finer spatial grid, this can also be a source of problems. First, if cells small enough to solve the fine detail are used throughout the problem space, the total number of cells may be enormous. Therefore, small cells will tremendously increase the number of unknown fields in the FDTD code. Second, if the cell dimensions are small, the time increment used will also have to be small to satisfy the Courant stability condition [8]. This would mean that the computational efficiency of the FDTD technique would be greatly reduced. Fine subgrid models can also be used, but there can be problems of numerical noise being transferred across the fine/coarse grid boundaries.

An alternative method of dealing with the problem of fine detail in FDTD codes is to build the near-field physics of the fine detail in question into those cells that contain them, thus allowing the cell size in the solution space to be uniform and relatively large [3]. The reasoning behind this technique is that while the "normal" FDTD equations for advancing the fields assume a smooth linear variation in each cell, these "smart" cells can have a specified nonlinearity built in and still be large. This approach has been used with success in modeling thin dielectric structures.

Another limitation of the FDTD technique is its inability to model targets that include curved surfaces. This is so because the technique uses square (two-dimensional) or cubic (three-dimensional) cells as its building blocks. However, recent developments [1] have shown that this problem can be overcome by applying the integral form of Maxwell's equations on smoothly curved conducting surfaces.

Chapter 3: Near-Field to Far-Field Transformations

3.1 Introduction

Neither the far-field response, nor the radar cross section of a scatterer, is provided directly by the FDTD technique. A near-field to far-field transformation can be achieved by applying the equivalence principle [15] around a scattered field virtual surface, as shown in figure 3.1.

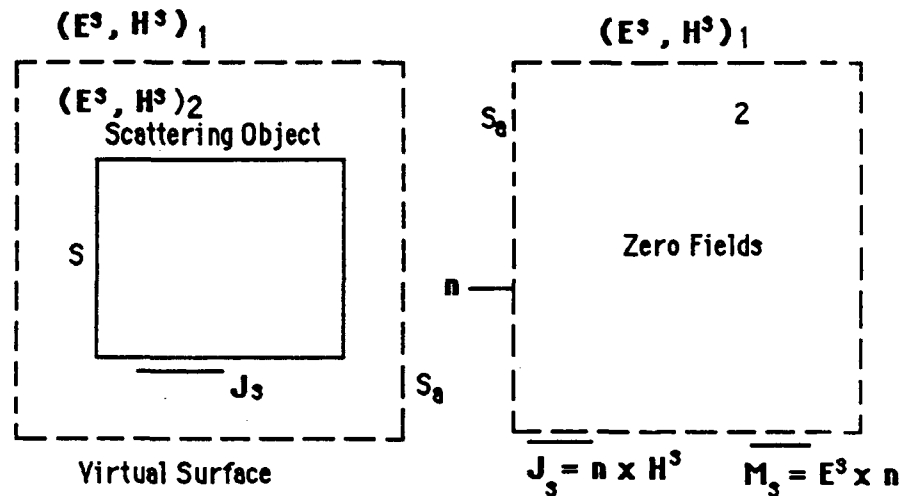


Figure 3.1 General formulation of the equivalence principle

When E^s and H^s are known scattered fields surrounding the scatterer along the closed surface S_a , the equivalent tangential electric current J_s and equivalent magnetic current M_s can be defined as

$$J_s(\mathbf{r}) = \mathbf{n} \times \mathbf{H}^s(\mathbf{r}) \quad (3.1)$$

$$M_s(\mathbf{r}) = -\mathbf{n} \times \mathbf{E}^s(\mathbf{r}) \quad (3.2)$$

where \mathbf{n} is the outward unit normal vector at the surface S_a , and E^s and H^s are the scattered fields on the surface. The equivalent currents defined by equations (3.1) and (3.2) on the closed surface S_a will produce the same scattered fields (E^s, H^s) external to S_a as in the original problem.

This approach is applied to extrapolate the near fields of the FDTD technique to the far-field radiation zone for both two-dimensional and three-dimensional problems. The two-dimensional transformation is implemented in the frequency domain, whereas the three-

dimensional transformation is implemented in the time domain. For the two-dimensional case the steady-state information required is obtained using a least squares estimation method.

A somewhat different approach for obtaining the far-field response directly in the time domain, for two-dimensional structures, is reported by Britt [15]. The closed contour (virtual surface) used for the integration of the equivalent currents is different in this case from the one used in figure 3.1. Instead of enclosing the target, one of the faces of Britt's contour encloses the far-field observation point. The contribution from this face to the far-field is assumed to be negligible.

3.2 Two-Dimensional Transformation

Once the steady-state equivalent currents along the virtual surface S_a are calculated, the electric and magnetic potentials for two-dimensional problems can be evaluated using the equations [14]

$$A(\rho) = \frac{1}{4j} \int \int_S J(\rho') H_0^{(2)}(k|\rho - \rho'|) ds' \quad (3.3)$$

$$F(\rho) = \frac{1}{4j} \int \int_S M(\rho') H_0^{(2)}(k|\rho - \rho'|) ds' \quad , \quad (3.4)$$

where the integration extends over the cross section of the source, or in this case over the closed surface S_a . In equations (3.3) and (3.4), $H_0^{(2)}$ is the zero order Hankel function of the second kind and k is the wavenumber. The primed coordinates represent the location of the source, whereas the unprimed coordinates represent the location of the observer. For $k|\rho - \rho'|$ large, the Hankel function in equations (3.3) and (3.4) can be approximated by

$$H_0^{(2)}(k|\rho - \rho'|) \approx \sqrt{\frac{2j}{\pi k|\rho - \rho'|}} e^{-jk|\rho - \rho'|} \quad (3.5)$$

Furthermore, when $\rho \gg \rho'$ as shown in figure 3.2, then

$$|\rho - \rho'| \approx \rho - \rho' \cos(\phi - \phi') \quad (3.6)$$

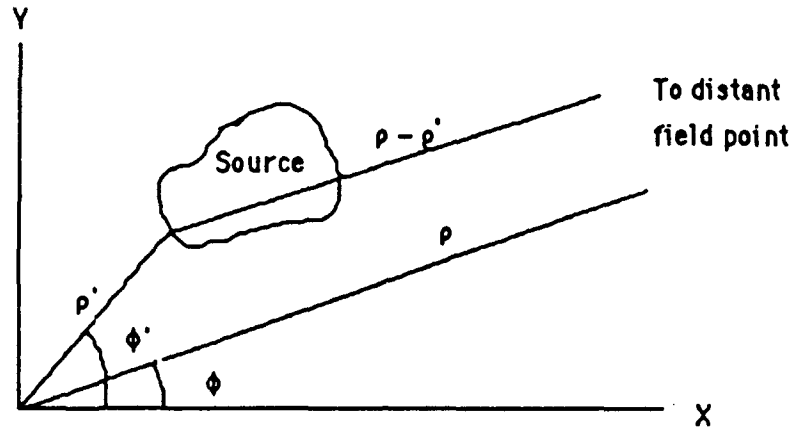


Figure 3.2 Geometry for determining the far fields

The second term in (3.6) must be retained in the phase factor, $\exp(-k j |\rho - \rho'|)$, but not in the magnitude factor, $|\rho - \rho'|^{-1/2}$, of equation (3.5).

Applying all the previous assumptions to equations (3.3) and (3.4) the electric and magnetic vector potentials simplify to

$$\mathbf{A}(\rho) = \frac{e^{-jk\rho}}{\sqrt{8j\pi k\rho}} \int \int_{S_a} \mathbf{J}(\rho') e^{jk\rho' \cos(\phi - \phi')} ds' \quad (3.7)$$

$$\mathbf{F}(\rho) = \frac{e^{-jk\rho}}{\sqrt{8j\pi k\rho}} \int \int_{S_a} \mathbf{M}(\rho') e^{jk\rho' \cos(\phi - \phi')} ds' \quad (3.8)$$

However,

$$k\rho' \cos(\phi - \phi') = k\rho' \cos \phi \cos \phi' + k\rho' \sin \phi \sin \phi' \quad (3.9)$$

Converting (3.9) from cylindrical to rectangular coordinates using the transformation

$$x' = \rho' \cos \phi', \quad y' = \rho' \sin \phi', \quad \rho' = \sqrt{(x'^2 + y'^2)}, \quad (3.10)$$

one obtains the following expression in rectangular coordinates:

$$k\rho' \cos(\phi - \phi') = k(x' \cos \phi + y' \sin \phi) \quad (3.11)$$

Replacing (3.11) into (3.7) and (3.8) and realizing that the surface integrals are actually line integrals applied over the closed surface S_a (for two-dimensional problems), the final expressions of the electric and magnetic vector potentials are

$$\mathbf{A} = K_c \int_{S_a} \mathbf{J}(x',y') e^{jk(x' \cos \phi + y' \sin \phi)} dl' \quad (3.12)$$

$$\mathbf{F} = K_c \int_{S_a} \mathbf{M}(x',y') e^{jk(x' \cos \phi + y' \sin \phi)} dl' \quad (3.13)$$

where

$$K_c = \frac{e^{-jk\rho}}{\sqrt{8j\pi k\rho}} = \frac{e^{-jk\rho}}{\sqrt{8\pi k\rho}} e^{-j\pi/4}$$

3.2.1 Application to TM Polarization (E_z, H_x, H_y)

The FDTD grid for TM polarization is shown in figure 3.3. In this figure some of the fields involved in the calculation of the equivalent electric and magnetic currents are shown.

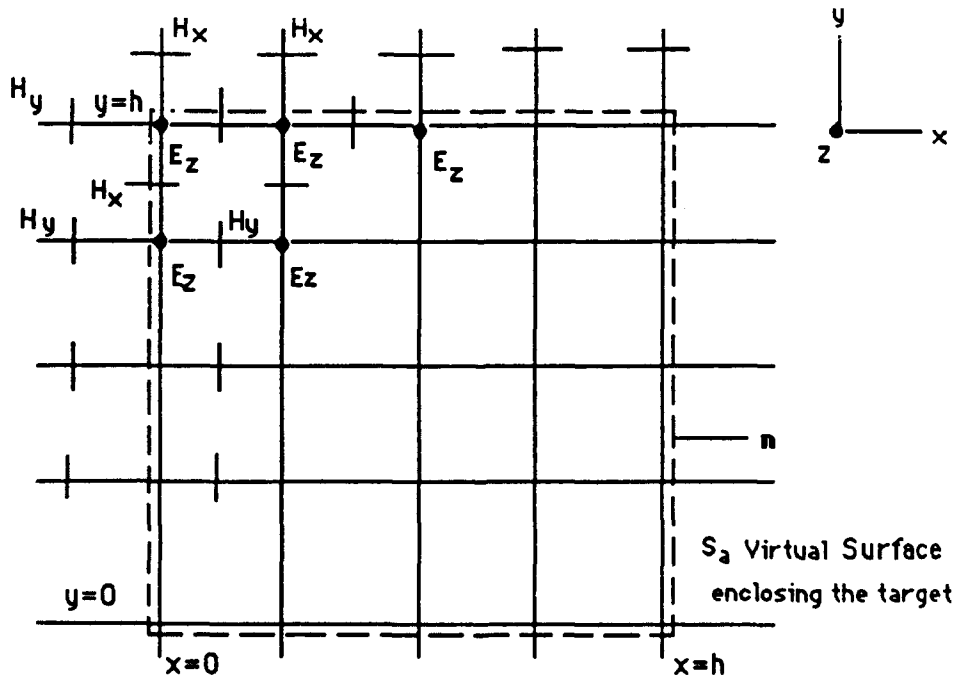


Figure 3.3 FDTD grid for TM polarization

The equivalent electric and magnetic currents at each lattice point on the virtual surface surrounding the target can be found as follows:

(a) $x = h$ face

$$\begin{aligned} \mathbf{J}_z(x', y') &= \hat{X} \times \mathbf{H}_y \hat{y} = \hat{z} H_y \\ \mathbf{M}_y(x', y') &= -\hat{X} \times \mathbf{E}_z \hat{y} = -\hat{y} E_z \end{aligned}$$

(b) $x = 0$ face

$$\begin{aligned} \mathbf{J}_z(x', y') &= -\hat{X} \times \mathbf{H}_y \hat{y} = -\hat{z} H_y \\ \mathbf{M}_y(x', y') &= \hat{X} \times \mathbf{E}_z \hat{y} = -\hat{y} E_z \end{aligned}$$

(c) $y = h$ face

$$\begin{aligned} \mathbf{J}_z(x', y') &= \hat{y} \times \mathbf{H}_x \hat{x} = \hat{z} H_x \\ \mathbf{M}_x(x', y') &= -\hat{y} \times \mathbf{E}_z \hat{z} = -\hat{x} E_z \end{aligned}$$

(d) $y = 0$ face

$$\begin{aligned} \mathbf{J}_z(x', y') &= -\hat{y} \times \mathbf{H}_x \hat{x} = \hat{z} H_x \\ \mathbf{M}_x(x', y') &= -\hat{y} \times \mathbf{E}_z \hat{z} = \hat{x} E_z \end{aligned} \tag{3.14}$$

It should be noted at this point that the location of the magnetic field points do not coincide with the virtual surface where the equivalence principle is applied. In order to avoid violating the equivalence principle, new magnetic field locations are defined on the virtual surface S_a , by averaging the values just inside and outside the virtual surface. In this way, consistency is retained in applying the equivalence principle since both \mathbf{E} and \mathbf{H} are found on the same surface, and therefore more accurate results are obtained. Also, care should be taken in handling the corners where the \mathbf{E}_z fields are located. For example, consider an \mathbf{E}_z field that is located where the $x = h$ and $y = h$ faces of figure 3.3 intersect each other. Since this point is common to both faces, the field located at this point could give rise to a magnetic current that is x -directed or y -directed. In order to resolve this problem, the amplitude of the electric field at this particular field point is divided into two equal parts, with one half contributing to the x -directed magnetic current and the other half to the y -directed magnetic current.

Once the equivalent electric and magnetic currents are established on the four faces of the surface S_a as shown in figure 3.3, the electric vector potential (A_z) and the magnetic vector potentials (F_x, F_y) can be evaluated using equations (3.12) and (3.13), respectively. Transforming these potentials from rectangular back to cylindrical coordinates, one obtains

$$F_\phi = -F_x \sin \phi + F_y \cos \phi$$

$$A_z = A_z \quad (3.15)$$

Finally, the far fields can be evaluated using the following relations:

$$E_z^S(\phi) = -j\omega\mu A_z + jkF_\phi \quad (3.16)$$

$$H_\phi^S(r) = -E_z^S(\phi)/\eta, \quad (3.17)$$

where η represents the intrinsic impedance of free space (120 π Ohms). The radar cross section of the scatterer can be evaluated using

$$RCS(\Phi) = \lim_{\rho \rightarrow \infty} 2\pi\rho \frac{|E_z^S(\phi)|^2}{|E_z^i|^2} \quad (3.18)$$

where E_z^i represents the amplitude of the incident field.

3.2.2 Application to TE polarization (E_x, E_y, H_z)

The FDTD grid for TE polarization is shown in figure 3.4.

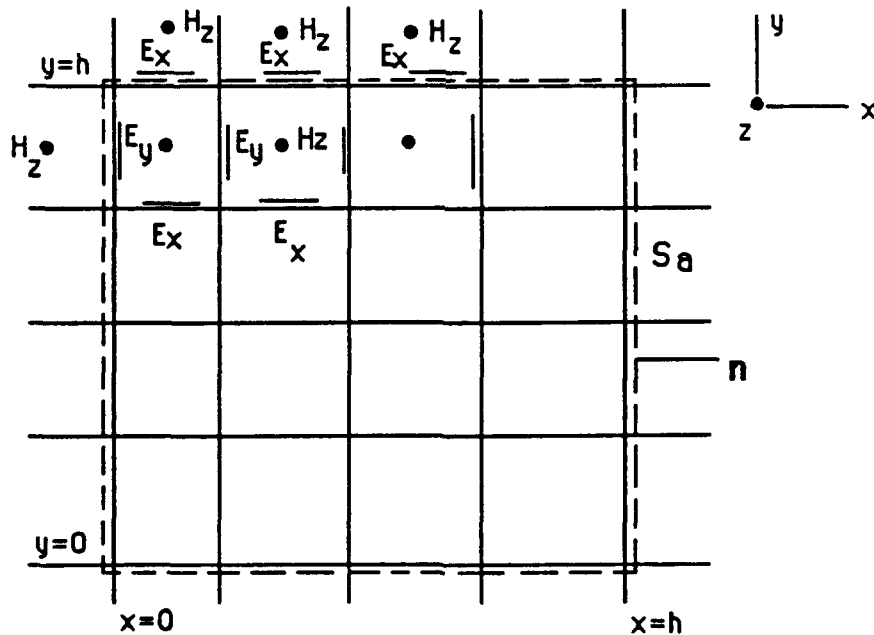


Figure 3.4 FDTD grid for TE polarization

The equivalent electric and magnetic currents at each lattice point on the virtual surface surrounding the target can be found in a fashion similar to the TM polarization case as follows:

(a) $x = h$ face

$$\begin{aligned} \mathbf{J}_y(x', y') &= \hat{\mathbf{X}} \times \mathbf{H}_z \hat{\mathbf{z}} = -\hat{\mathbf{y}} H_z \\ \mathbf{M}_z(x', y') &= -\hat{\mathbf{X}} \times \mathbf{E}_y \hat{\mathbf{y}} = -\hat{\mathbf{z}} E_y \end{aligned}$$

(b) $x = 0$ face

$$\begin{aligned} \mathbf{J}_y(x', y') &= -\hat{\mathbf{X}} \times \mathbf{H}_z \hat{\mathbf{z}} = -\hat{\mathbf{y}} H_z \\ \mathbf{M}_z(x', y') &= \hat{\mathbf{X}} \times \mathbf{E}_y \hat{\mathbf{y}} = \hat{\mathbf{z}} E_y \end{aligned}$$

(c) $y = h$ face

$$\begin{aligned} \mathbf{J}_x(x', y') &= \hat{\mathbf{y}} \times \mathbf{H}_z \hat{\mathbf{z}} = \hat{\mathbf{x}} H_z \\ \mathbf{M}_z(x', y') &= -\hat{\mathbf{y}} \times \mathbf{E}_x \hat{\mathbf{z}} = -\hat{\mathbf{x}} E_x \end{aligned}$$

(d) $y = 0$ face

$$\begin{aligned} \mathbf{J}_x(x', y') &= \hat{\mathbf{y}} \times \mathbf{H}_z \hat{\mathbf{z}} = -\hat{\mathbf{x}} H_z \\ \mathbf{M}_z(x', y') &= -\hat{\mathbf{y}} \times \mathbf{E}_x \hat{\mathbf{z}} = -\hat{\mathbf{x}} E_x \end{aligned} \quad (3.19)$$

Once the above equivalent currents are established on the four faces of the FDTD problem space shown in figure 3.4, the electric vector potentials (A_x, A_y) and the magnetic vector potential (F_z) can be evaluated using the equations (3.12) and (3.13), respectively. Transforming these potentials from rectangular to cylindrical coordinates, one obtains

$$\begin{aligned} A_\phi &= -A_x \sin \phi + A_y \cos \phi \\ F_z &= F_z. \end{aligned} \quad (3.20)$$

Finally, the far-field response can be evaluated using

$$E_\phi^S(\phi) = -j\omega\mu F_\phi - jkF_z \quad (3.21)$$

$$H_z^S(\phi) = E_\phi^S(\phi)/\eta. \quad (3.22)$$

In the same manner as the TM case, the radar cross section of the scatterer can be found using the equation

$$\text{RCS}(\Phi) = \lim_{\rho \rightarrow \infty} 2\pi\rho \left| \frac{E_\phi^S(\phi)}{E^i} \right|^2 \quad (3.23)$$

where E^i can be an E_x component, an E_y component, or a combination of the two.

3.3 Three-Dimensional Transformation

A procedure similar to the one followed in two-dimensional problems can also be applied to three-dimensional problems. Once the equivalent currents along the virtual surface S_a are established, the vector potentials for three-dimensional problems can be evaluated using the equations [15, p. 100]

$$A(\mathbf{r}) = \frac{1}{4\pi} \iiint_V \frac{\mathbf{J}(\mathbf{r}') e^{-jk|\mathbf{r}-\mathbf{r}'|}}{|\mathbf{r}-\mathbf{r}'|} dv' \quad (3.24)$$

$$\mathbf{F}(\mathbf{r}) = \frac{1}{4\pi} \iiint_V \frac{\mathbf{M}(\mathbf{r}') e^{-jk|\mathbf{r}-\mathbf{r}'|}}{|\mathbf{r}-\mathbf{r}'|} dv' \quad (3.25)$$

Considering only the far-field region ($r \gg r'_{\max}$) as shown in figure 3.5, the following approximation can be made

$$|\mathbf{r}-\mathbf{r}'| \approx r - r' \cos \xi \quad (3.26)$$

where ξ is the angle between \mathbf{r} and \mathbf{r}' . Furthermore, the second term of equation (3.26) can be neglected in the magnitude term of equations (3.24) and (3.25), but not in the phase term.

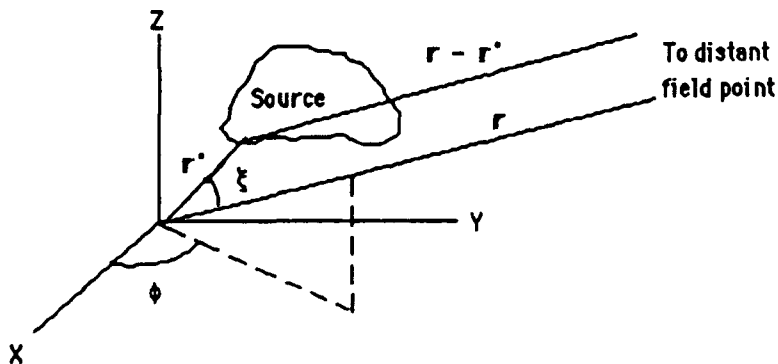


Figure 3.5 Geometry for calculating the far fields

Applying the above assumptions and realizing that the volume integrals are actually surface integrals over the closed surface S_a , (3.24) and (3.25) simplify to:

$$\mathbf{A} = \frac{e^{-jkr}}{4\pi r} \iint_{S_a} \mathbf{J}(r') e^{jkr' \cos \xi_{ds'}} \quad (3.27)$$

$$\mathbf{F} = \frac{e^{-jkr}}{4\pi r} \iint_{S_a} \mathbf{M}(r') e^{jkr' \cos \xi_{ds'}} \quad (3.28)$$

Equations (3.27) and (3.28) are Fourier transformable, allowing the evaluation of the vector potentials directly in the time domain. Therefore, for three-dimensional problems, it is not necessary to convert the time-domain fields into the frequency domain before evaluating the far-field response. In this way, time marching vector potentials are obtained, which are then used to find the far-field response of three-dimensional structures directly in the time domain. For more information on the implementation of the three-dimensional transformation the reader is referred to [5].

3.4 Amplitude and Phase Estimation

A least squares estimation method [16] can be used to obtain accurate information about the magnitude and phase of sinusoidal steady-state problems. This information is used in the two-dimensional near-field to far-field transformation, as well as to plot the amplitude distribution of selected field points in the near-field region. Given the form of a two parameter model to be

$$X_t = A \cos \omega t + B \sin \omega t + \epsilon_t \quad (3.29)$$

where X_t is the t^{th} data value and ϵ_t is the t^{th} residual needed to make the equality exact, the least squares method proceeds by minimizing the mean square error, as expressed in the following equation:

$$T(A,B) = \sum_{t=0}^{n-1} (X_t - A \cos \omega t - B \sin \omega t)^2 \quad (3.30)$$

Taking the partial derivatives of $T(A, B)$ with respect to A , and B and setting them equal to zero, results in

$$\frac{\partial T}{\partial A} = -2 \sum_{t=0}^{n-1} \cos \omega t (X_t - A \cos \omega t - B \sin \omega t) = 0 \quad (3.31)$$

$$\frac{\partial T}{\partial B} = -2 \sum_{l=0}^{n-1} \sin \omega t (X_l - A \cos \omega t - B \sin \omega t) = 0 \quad (3.32)$$

Rearranging and solving the resulting system of two equations with two unknowns for A, and B, the following solution is obtained:

$$A = \frac{1}{\Delta} \left\{ \sum_{l=0}^{n-1} X_l \cos \omega t \sum_{l=0}^{n-1} (\sin \omega t)^2 - \sum_{l=0}^{n-1} X_l \sin \omega t \sum_{l=0}^{n-1} \cos \omega t \sin \omega t \right\} \quad (3.33)$$

$$B = \frac{1}{\Delta} \left\{ \sum_{l=0}^{n-1} X_l \sin \omega t \sum_{l=0}^{n-1} (\cos \omega t)^2 - \sum_{l=0}^{n-1} X_l \cos \omega t \sum_{l=0}^{n-1} \cos \omega t \sin \omega t \right\}, \quad (3.34)$$

$$\text{where } \Delta = \sum_{l=0}^{n-1} (\cos \omega t)^2 \sum_{l=0}^{n-1} (\sin \omega t)^2 - \left(\sum_{l=0}^{n-1} \cos \omega t \sin \omega t \right)^2$$

The summations involving only trigonometric functions can be evaluated as [16]

$$\sum_{l=0}^{n-1} (\cos \omega t)^2 = \frac{n}{2} (1 + D_n(2\omega) \cos(n-1)\omega) \quad (3.35)$$

$$\sum_{l=0}^{n-1} \cos \omega t \sin \omega t = \frac{n}{2} (1 + D_n(2\omega) \sin(n-1)\omega) \quad (3.36)$$

$$\sum_{l=0}^{n-1} (\sin \omega t)^2 = \frac{n}{2} (1 - D_n(2\omega) \cos(n-1)\omega) \quad \text{where } D_n(\omega) = \frac{\sin\left(\frac{n\omega}{2}\right)}{n \sin\left(\frac{\omega}{2}\right)} \quad (3.37)$$

The summations involving (X_l) are evaluated as the FDTD technique time steps the fields in the problem space.

Once A and B are evaluated the phasor form of selected points in the FDTD problem space can be found using the expressions

$$R = \sqrt{A^2 + B^2} \quad (3.38)$$

$$\phi = \text{Arctan}(-B/A), \quad (3.39)$$

where R represents the amplitude and ϕ the phase of a selected point in the FDTD grid. It is required that several periods of the waveform be time stepped (4-7 cycles) before this algorithm is applied, in order for the transient response to die out. Once the waveform reaches steady-state, the algorithm is invoked and accurate estimates of the amplitude and phase of the waveform are obtained. If a d.c term is expected to be present in the scattered fields, a three parameter model can

obtained. If a d.c term is expected to be present in the scattered fields, a three parameter model can be used to convert the time domain fields into the frequency domain. The third parameter involved will be the mean value of the scattered sinusoidal field. For the problems examined in this study the d.c term was found to be zero and hence, a two parameter model was chosen.

3.5 2-D Numerical Results

The near-field to far-field transformation is tested by evaluating the far-field response of an infinitely long filament of constant a-c current along the z-axis. To do this, the FDTD code uses a second order RBC as well as a total-field/scattered-field zoning scheme. The infinitely long filament of constant a-c current is simulated using the FDTD code by forcing four sinusoidally varying magnetic fields (of equal amplitude and phase) in the FDTD grid, as shown in figure 3.6.

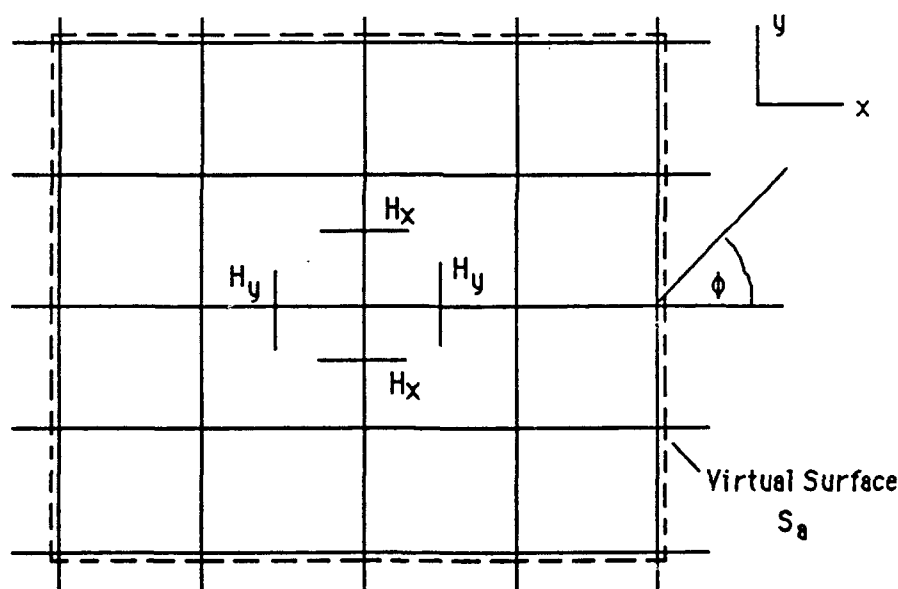


Figure 3.6 Implementation of an infinitely long filament of constant a-c current using the FDTD technique.

The far fields of this radiator should be independent of the look angle, ϕ , since the line source is symmetric in ϕ . In other words, the constant a-c current source should represent an isotropic radiator. This simulation was repeated for several FDTD cell sizes to analyze the behavior of the numerical error involved as the cell size of the FDTD grid decreases. The z-component of the electric field in the radiation zone is shown in figure 3.7 for different cell sizes. For a cell size

equal to $\lambda/10$ there are small variations (about 2%) from the exact value of the amplitude of the electric field as the look angle changes. However, much better results are obtained for smaller cell sizes.

The total numerical error estimated using this simulation is mainly due to the combined effects of:

- 1) the error produced from the amplitude and phase estimation of the data using the least squares method,
- 2) the error introduced when averaging the tangential magnetic field inside and outside the virtual surface in order to find an approximate value of the magnetic field on the virtual surface,
- 3) the error due to the fact that the FDTD code calculates average field values taken at sample points in the grid, while the equivalence principle requires surface currents over the extent of the whole FDTD unit cell.

In the following chapters, the FDTD technique is applied to scattering problems involving relatively thin dielectric structures. The general trend in the analysis is to apply the FDTD technique to solve the scattering problem initially in a "brute force" method. That is, very fine resolution cells are used despite the computational burden they have on the technique. Then, "smart" cells are developed where the structure under consideration has dimensions less than the cell size of the FDTD grid. This method will be referred to as the "thin equation" approach.

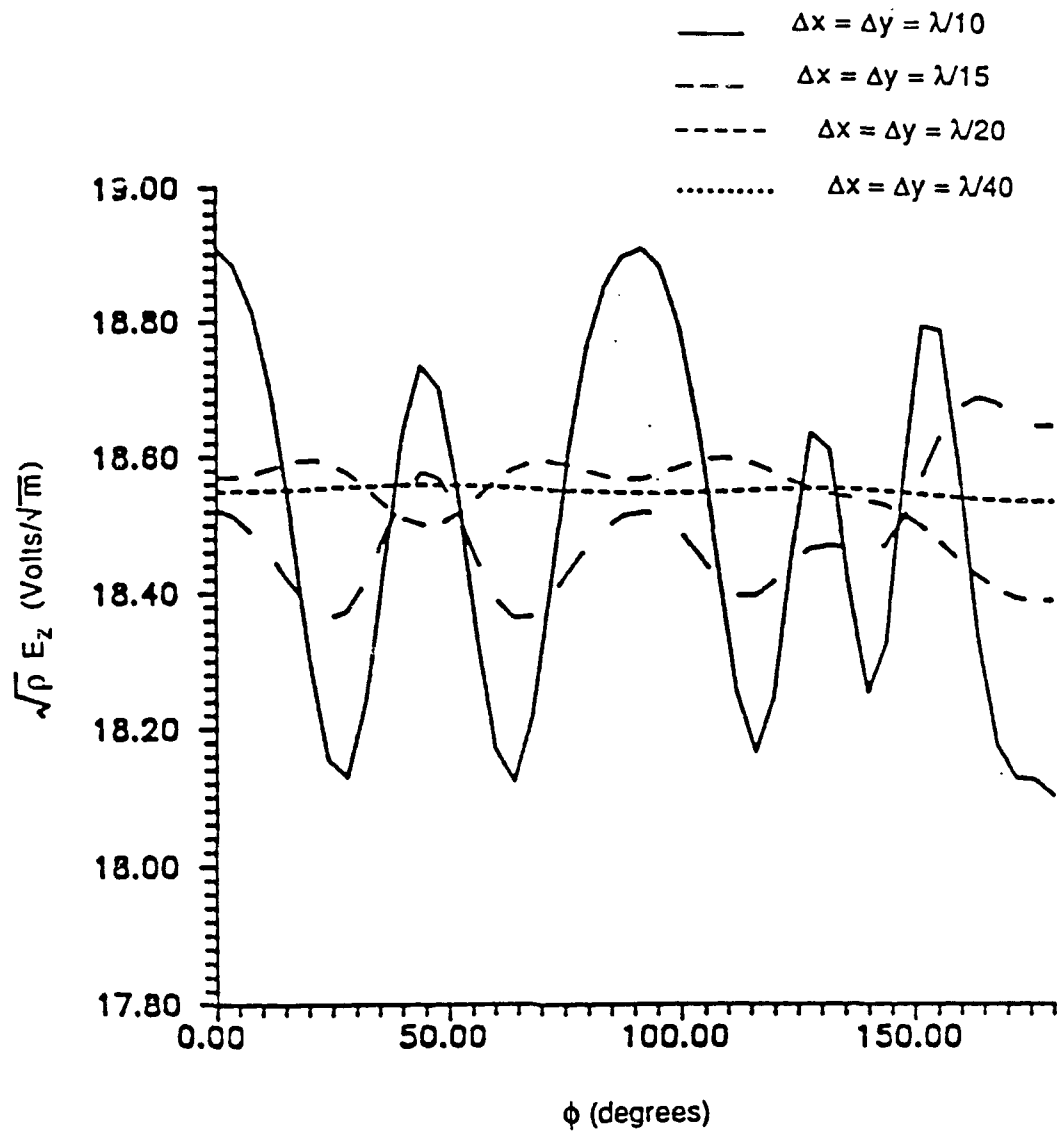


Figure 3.7 Far-field obtained using the FDTD code from an infinite line source of constant a-c current

Chapter 4: Modeling of Dielectric Structures

4.1 Numerical Techniques Applied to Dielectrics

There are several frequency domain analytical and /or numerical methods that can be applied to scattering by homogeneous dielectric structures. For structures whose boundary surfaces coincides with a given coordinate system, separation of variables can be applied and the scattered fields can be estimated in closed form. Analytical solutions have been obtained for simple structures such as a sphere and a circular cylinder [18]. For structures of arbitrary shape, either the volume [20], [17] or the surface [20] integral equation approach has been applied. For three-dimensional problems several authors have utilized different basis functions [22], [23], [24] based on the method of moments approach.

The volume integral equation approach is based on relating the induced polarization currents to the corresponding total fields, which consist of the scattered and incident fields. By associating an unknown polarization current to the cells composing the structure, the operator form of the integral equation can be converted into an equivalent matrix equation. Employing the volume equivalence principle and method of moments, scattering results can be obtained from structures such as dielectric cylinders, plane dielectric slabs, dielectric cylindrical shells, and biological tissue cylinders.

The surface integral equation approach is very well suited to analyzing homogeneous dielectric structures. This approach reduces the original problem to two equivalent problems, one for the external medium and one for the internal medium. The scattered fields inside and outside the dielectric are assumed to be produced by some unknown equivalent electric and magnetic surface currents radiating into unbounded media. These currents can be determined by solving a set of coupled integral equations, obtained by applying proper boundary conditions to the tangential components of the total electric and/or magnetic fields. One may use the same or different sets of equivalent currents for the internal and external problems.

Structures of arbitrary cross section can be analyzed, using either the volume or surface integral equations, in conjunction with the method of moments approach. This method is well suited for low frequency scattering problems, with structures extending to one or two wavelengths in three dimensions [24]. For planar surfaces, one can conveniently use "pulse expansion, point matching" in conjunction with the volume integral equation approach [22] to obtain far-field results that are as accurate as those obtained using "triangular patches" in conjunction with the surface integral

approach. However, pulse expansion functions give rise to charge distributions within the body which theoretically cannot exist in homogeneous dielectrics, thus resulting in erroneous near-fields [21].

A better alternative to frequency domain techniques is provided by the FDTD technique, which solves Maxwell's time-dependent integral equations directly in the time domain. It has recently been shown that FDTD has certain advantages over the MoM when dielectrics are involved [9]. A serious limitation of the traditional MoM technique is the need to invert a large matrix equation. This requires order N^3 computations and order N^2 storage, where N is the number of pulse basis functions (cells) used to subdivide the structure. FDTD requirements for storage and execution time are often less. Also, the FDTD technique allows the modeling of dielectric structures without requiring accurate air-dielectric boundary specifications [9]. In contrast, MoM requires very accurate air-dielectric boundary specifications, as well as the removal of the fictitious line charge sources that are generated when pulse basis point matching functions are used. These requirements prevent the application of efficient iterative techniques, like the fast-Fourier-transform conjugate gradient technique, to solve the linear system of equations and help reduce the computational and storage requirements [9].

4.2 Application of FDTD to Dielectric Structures

The analysis of scatterers containing solid dielectric components using the FDTD technique is very straightforward. When homogeneous dielectric material is present throughout the cells in which total fields are being evaluated, it is only necessary to provide the dielectric constant of the material filling the cells when applying Ampere's law (see equation 2.4a). Figure 4.1 shows a two-dimensional cut of a FDTD spatial grid containing a dielectric slab scatterer. The dielectric slab, of thickness d and permittivity ϵ , is represented by the shaded region.

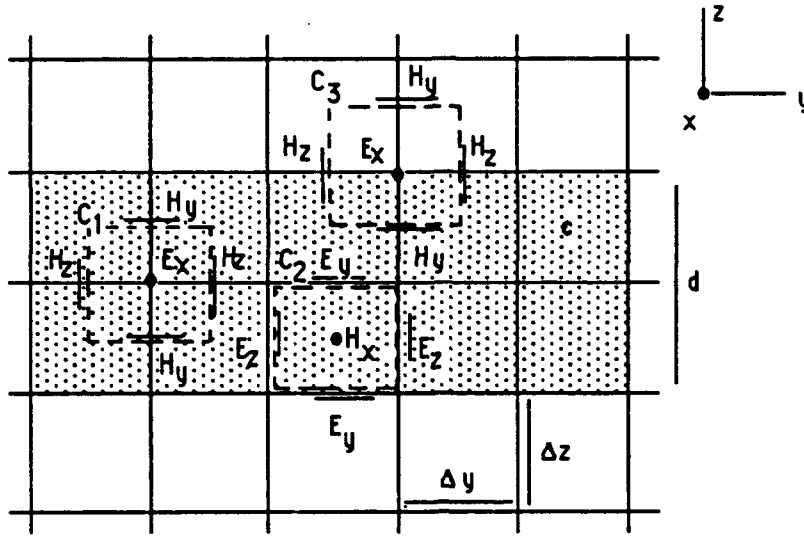


Figure 4.1 The orientation of a dielectric slab within the FDTD grid.

When applying Ampere's law over contour C_1 of figure 4.1, the only change that has to be made, assuming a lossless slab, is to replace ϵ_0 by $\epsilon_0\epsilon_r$ in updating the electric fields. In updating the magnetic fields by applying Faraday's law over contour C_2 of figure 4.1, no change need be made, assuming the magnetic permeability of the slab is the same as that of free space. Where there is an interface with free space, as shown in contour C_3 of figure 4.1, an average dielectric constant is assumed over the contour. Therefore, ϵ is replaced by $(\epsilon + \epsilon_0)/2$ in the equation used to update these fields.

If a homogeneous lossy material is to be modeled, the equations for updating the electric fields must be modified to take into account the electric loss. Assuming an electrical conductivity σ in mhos/meter and applying Ampere's law over contour C_1 (see figure 4.1), one obtains

$$\oint_{C_1} \mathbf{H} \cdot d\mathbf{l} = \sigma \iint_s \mathbf{E} \cdot d\mathbf{S} + \epsilon \frac{\partial}{\partial t} \iint_s \mathbf{E} \cdot d\mathbf{S} \quad (4.1)$$

Evaluating the surface integrals on the right hand side of (4.1) by assuming linear electric field distribution and replacing the partial derivative with respect to time by a central difference equation, the following expression is obtained:

$$\oint_{C_1} \mathbf{H} \cdot d\mathbf{l} = \sigma \mathbf{E}_x^{n+1/2} \Delta y \Delta z + \epsilon \left[\frac{\mathbf{E}_x^{n+1} - \mathbf{E}_x^n}{\Delta t} \right] \Delta y \Delta z \quad (4.2)$$

Assuming that

$$E_x^{n+1/2} = \frac{E_x^{n+1} - E_x^n}{2} \quad (4.3)$$

the final form of equation (4.2) can be written as

$$E_x^{n+1/2}(I,J,K) = \frac{1 - \frac{\sigma}{2\epsilon} \Delta t}{1 + \frac{\sigma}{2\epsilon} \Delta t} E_x^{n+1/2}(I,J,K) + \frac{\Delta t}{1 + \frac{\sigma}{2\epsilon} \Delta t} \int_{t_1} H \cdot dl \quad (4.4)$$

where the line integral in the second part of (4.4) can be evaluated as shown earlier. If the cell lies at an air-dielectric interface as shown in contour C_3 of figure 4.1, then σ is replaced by $\sigma/2$ and ϵ by $(\epsilon + \epsilon_0)/2$, as mentioned previously.

Similar equations can be derived for the remaining two electric fields (E_y , E_z). Since zero magnetic loss was assumed for the dielectric slab, the equations for advancing the H-fields do not have to be modified.

4.3 Modifications for Thin Dielectric Slabs

When a scatterer contains thin dielectric sheets, one can use cell dimensions that are small enough to resolve the sheet as a collection of solid cells of dielectric. This, however, requires cell dimensions throughout the problem space at least as small as the dielectric sheet thickness, resulting in high computational and storage requirements. In order to circumvent this undesirable situation, a model whereby the cell size can be allowed to be much larger than the slab thickness is desirable. The detailed derivation of such a model is found in [2].

Figure 4.2 shows a two-dimensional cut of a FDTD spatial grid containing a thin dielectric sheet scatterer. The dielectric, of thickness d and permittivity ϵ , is represented by the shaded region. The electric and magnetic field sample points pertinent to this discussion are labeled in this figure.

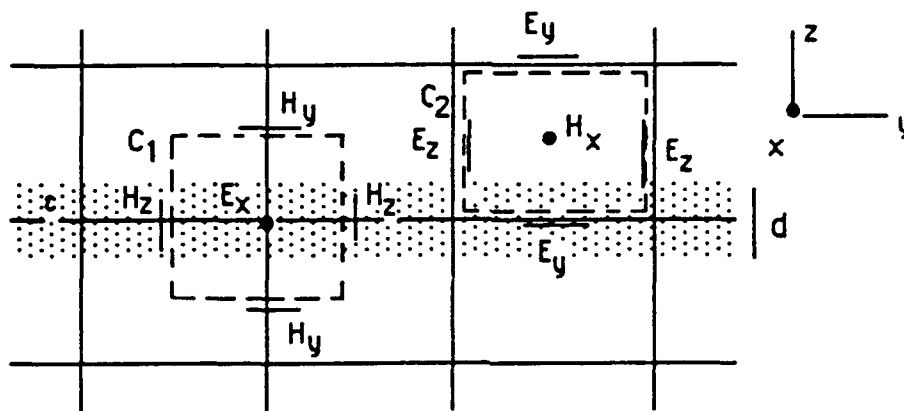


Figure 4.2 Orientation of a thin dielectric slab in the FDTD grid

Since the slab is electrically thin, all components of the magnetic and the tangential components of the electric fields can be considered linearly distributed within the dielectric. However, the normal component of the electric field exhibits a discontinuity across the dielectric interfaces. As a result, the calculations of the tangential magnetic fields adjacent to the slab have to be modified. Updating of the electric field inside the slab also has to be modified so as to take into account the effective dielectric constant within the cell.

Starting with Ampere's law and realizing that the slab is centered with respect to the contour over which the equation is applied, and that the x-directed electric field varies linearly throughout the contour, one obtains

$$\oint_{C_1} \mathbf{H} \cdot d\mathbf{l} = -\frac{\partial}{\partial t} \iint_S \epsilon \mathbf{E} \cdot d\mathbf{S} = -\frac{\partial}{\partial t} (\epsilon_{ave} E_x \Delta S) \quad (4.5)$$

where ϵ_{ave} represents the average dielectric constant in the cell. Integrating the magnetic fields over contour C_1 (see figure 4.2) and evaluating the partial derivative of the electric field with respect to time using central differencing, the following expression for updating the x-directed electric field is obtained:

$$E_x^{n+1}(I,J,K) = E_x^n(I,J,K) - \frac{\Delta t}{\epsilon_0 + (\epsilon - \epsilon_0) \frac{d}{\Delta z}} \left\{ \frac{1}{\Delta y} [H_z^{n+1/2}(I,J-1,K) - H_z^{n+1/2}(I,J,K)] + \frac{1}{\Delta z} [H_y^{n+1/2}(I,J,K) - H_y^{n+1/2}(I,J,K-1)] \right\} \quad (4.6)$$

A similar equation can be developed for the y-directed electric field.

In order to update the magnetic fields above and below the slab, Faraday's law (equation 2.4b) must be evaluated around a contour such as C_2 (see figure 4.2). Here the evaluation of the right hand side of equation (2.4b) proceeds exactly as if the dielectric were not there since it has been assumed that the magnetic field has distributed itself linearly throughout the cells. On the other hand, the evaluation of the line integral of E around the perimeter of the cell must be handled differently due to the discontinuity of the normal component of E at the air/dielectric interface. Figure 4.3 shows the behavior of E_z as a function of z in a cell that contains the dielectric slab. The function describing this behavior is

$$E_z = \begin{cases} \frac{\epsilon_0}{\epsilon} [E_z(I,J,K) + Az] & -\frac{\Delta z}{2} \leq z < -\frac{\Delta z}{2} + \frac{d}{2} \\ E_z(I,J,K) + Az & -\frac{\Delta z}{2} + \frac{d}{2} < z \leq \frac{\Delta z}{2} \end{cases} \quad (4.7)$$

where z is measured with respect to the center of the contour C_2 , and "A" is the slope of E_z .

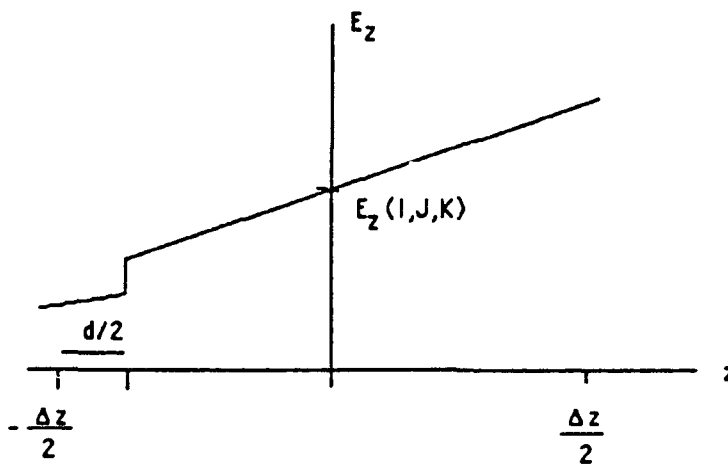


Figure 4.3 Behavior of the normal electric field along the z-direction

In order to evaluate the line integral of E_z in the left hand side of Faraday's law (equation 2.4b), knowledge of the slope "A" of the electric field under consideration is required. However, "A" can be estimated from known values of E_z on both sides of the slab. Thus:

$$A(I,J) = \frac{1}{\Delta z} [E_z^n(I,J,K) - E_z^n(I,J,K-1)] \quad (4.8)$$

where $A(I,J)$ denotes the slope of E_z along the lattice lines $x = I \Delta x$ and $y = J \Delta y$. Substituting (4.7) and (4.8) into Faraday's law and integrating around contour C_2 yields [2]:

$$\begin{aligned} H_x^{n+1/2}(I,J,K) = & H_x^{n-1/2}(I,J,K) \\ & + \frac{\Delta t}{\Delta y \Delta z \mu} \left\{ \left[\Delta z + \frac{d}{2} \left(\frac{\epsilon_0}{\epsilon} - 1 \right) \right] [E_z^n(I,J,K) - E_z^n(I,J+1,K)] \right. \\ & + [A(I,J) - A(I,J+1)] \frac{d}{4} \left(\frac{\epsilon_0}{\epsilon} - 1 \right) \left(\frac{d}{2} - \Delta z \right) \\ & \left. + \Delta y [E_y^n(I,J,K+1) - E_y^n(I,J,K)] \right\} \quad (4.9) \end{aligned}$$

A similar equation can be developed for H_y . If the slab becomes thicker than $\lambda/10$, it is best to model it as solid cubes.

4.4 Numerical Results

Numerical results obtained using the analysis outlined in the previous sections of this chapter are presented here. To begin with, figure 4.4 shows the radar cross section (RCS) of a lossy, thin dielectric slab versus the observation angle. The slab, of dimensions $2\lambda \times \lambda/40$, has a relative dielectric constant of $\epsilon_r = 4.5(1 - j1)$. The loss tangent in this case equals one (i.e, $\tan\delta = 1$). Here, results obtained using the brute force method are compared with results obtained using a MoM code provided by Richmond [30]. Excellent agreement within the main lobe and first sidelobe of the RCS pattern is illustrated when using the two methods. The slight disagreement in the second sidelobe level can be attributed to the inability of either the FDTD or the MoM codes to model the edges of the dielectric slab correctly.

A similar plot of the RCS versus the observation angle is exhibited in figure 4.5. The results were again obtained using the brute force method and the MoM. In this case, however, the dielectric slab has zero loss. Again, excellent agreement with the MoM is demonstrated within the mainlobe and first sidelobe of the RCS pattern. A much better agreement is obtained in predicting the second sidelobe levels of the RCS pattern, compared to the previous case. The FDTD technique, however, does not agree with the MoM in predicting the nulls of the RCS pattern (predicting about -32 dBsm instead of -40 dBsm as predicted by the MoM).

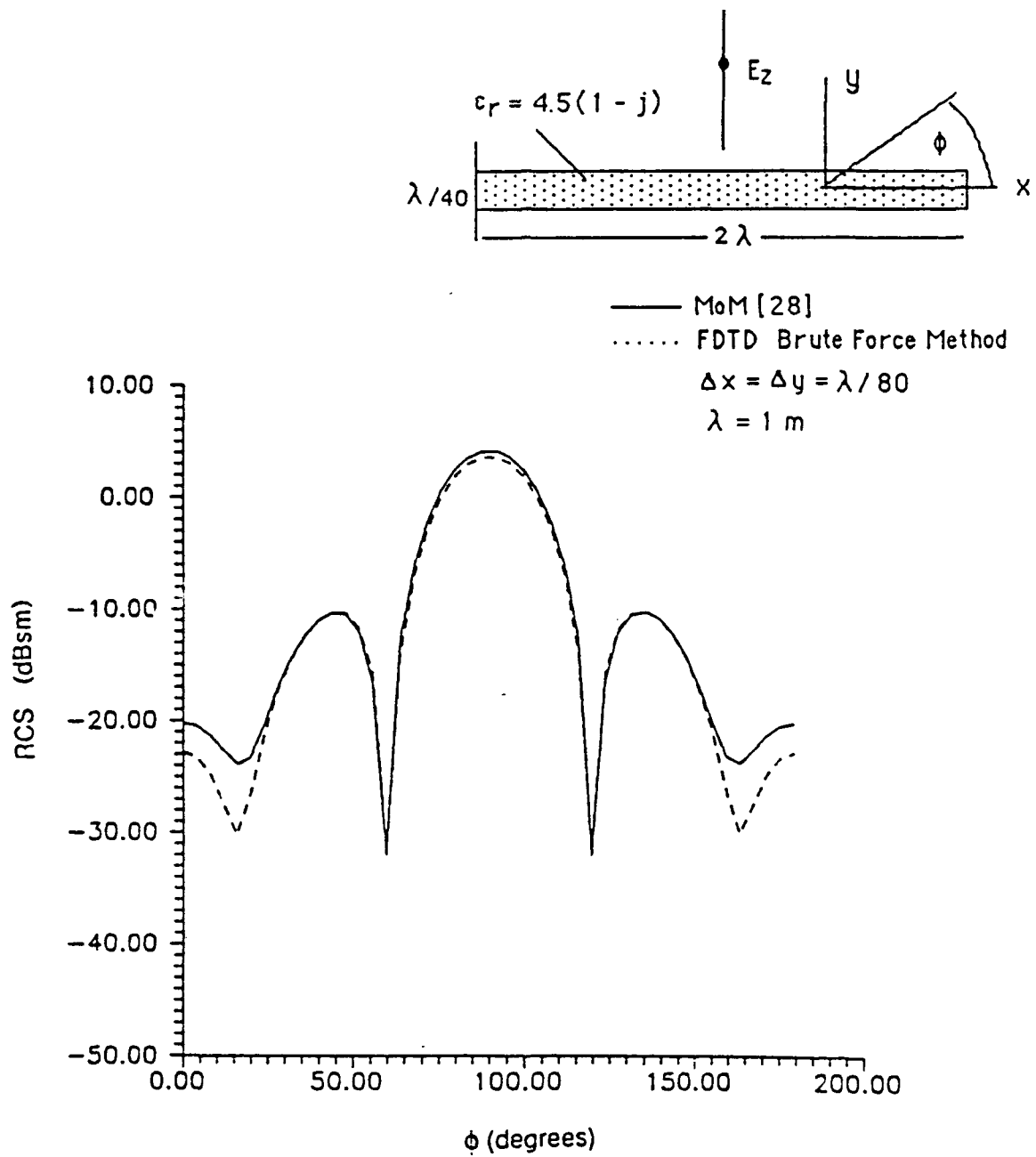


Figure 4.4 RCS of a lossy dielectric slab versus the observation angle obtained using the brute force FDTD method and the MoM (TM Polarization).

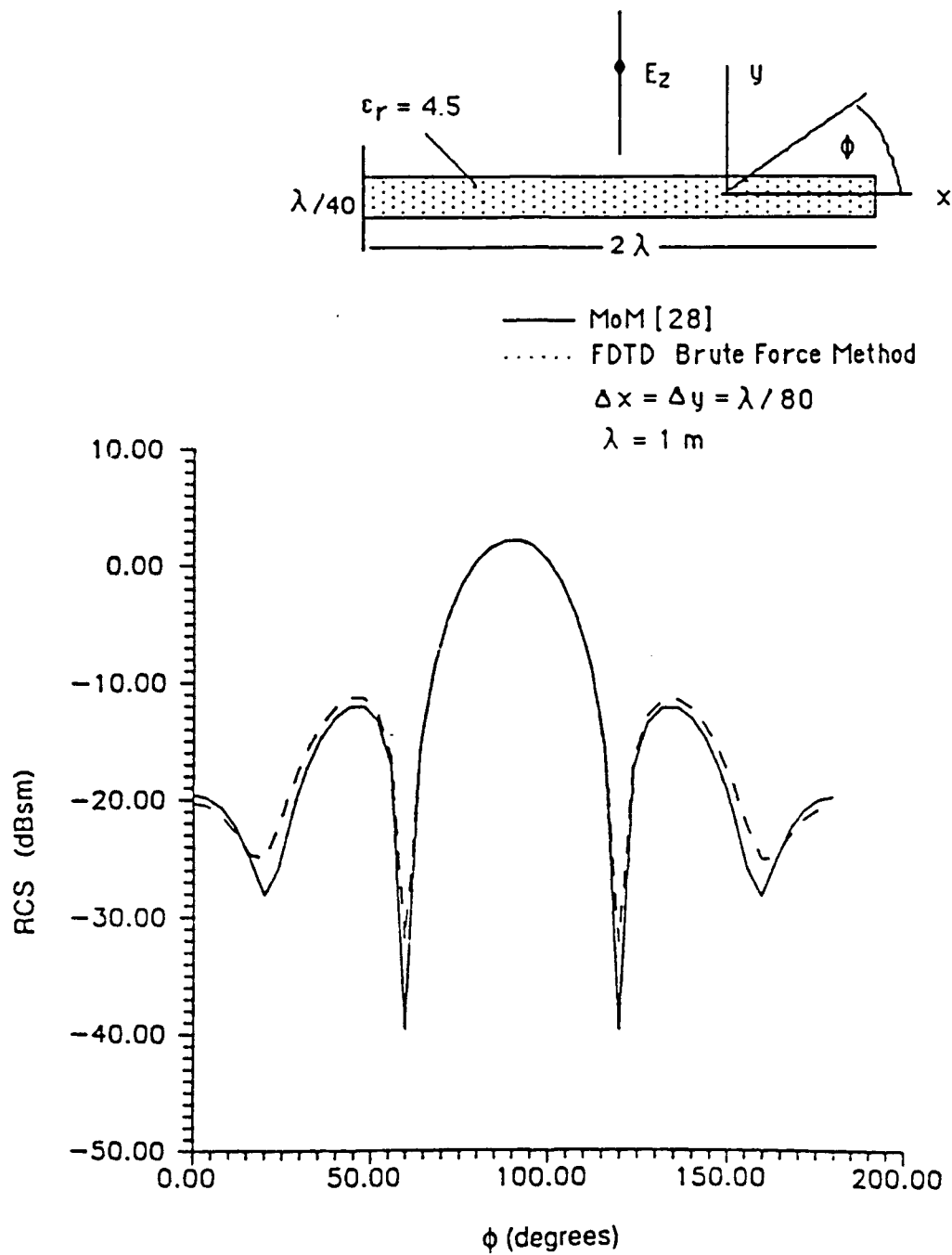


Figure 4.5 RCS of a lossless dielectric slab versus the observation angle obtained using the brute force FDTD method and the MoM (TM Polarization).

The RCS of a longer dielectric slab ($5\lambda \times \lambda/40$) versus observation angle is shown in figure 4.6. These results are also obtained using the brute force method and MoM. Good agreement is obtained in this case also between the FDTD technique and MoM despite the large dynamic range (40 dB) of this problem. The agreement indicated by this example can be attributed to the fact that the effect of the edges is smaller since a longer dielectric slab is used.

A comparison between the thin equation and brute force models of a thin, lossless dielectric slab versus the observation angle for TE polarization is illustrated in figure 4.7. The two curves show excellent agreement in predicting the mainlobe and first sidelobe of the RCS pattern. Figure 4.8 shows the distribution of the x-component of the electric field along the surface of dielectric slab. Again, there is good agreement between the two methods in the near-fields also.

Figure 4.9 compares the RCS of a dielectric slab for TM polarization, obtained using the thin equation approach, the brute force method, and the MoM. Although there is fair agreement between the three curves within the mainlobe of the RCS pattern, the results of the FDTD thin equation approach fail to predict the correct nulls of the RCS pattern. The difference between the curves at the null points is about 20 dB when compared to MoM, and 12 dB when compared to the brute force method. This problem was analyzed further using the brute force method in order to provide an explanation as to why the thin equation approach fails to predict the correct RCS of the dielectric slab for TM polarization. It was then found that the y-component of the magnetic field exhibited a distribution across the dielectric

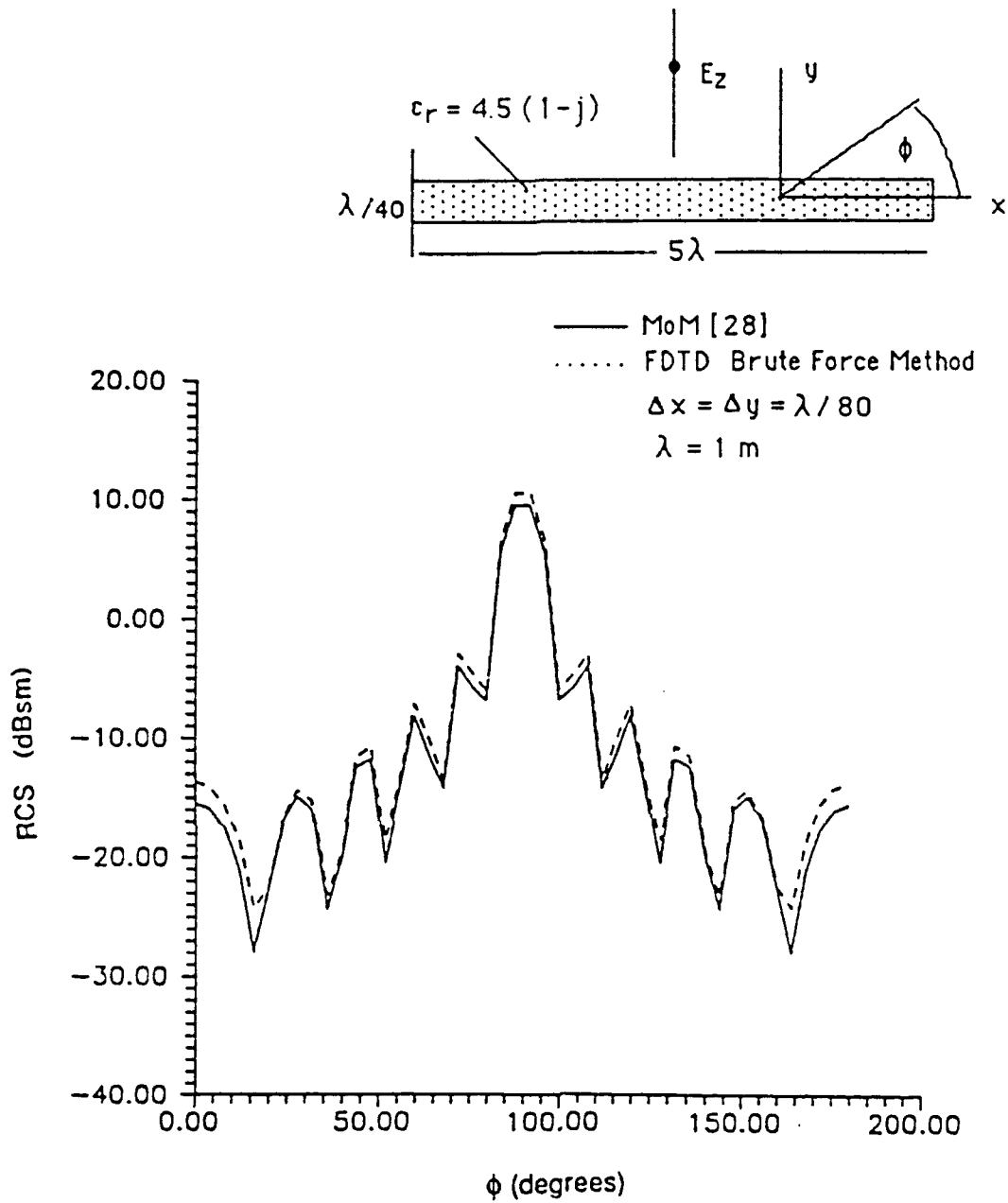


Figure 4.6 RCS of a lossy dielectric slab versus the observation angle obtained using the brute force FDTD method and the MoM (TM Polarization).

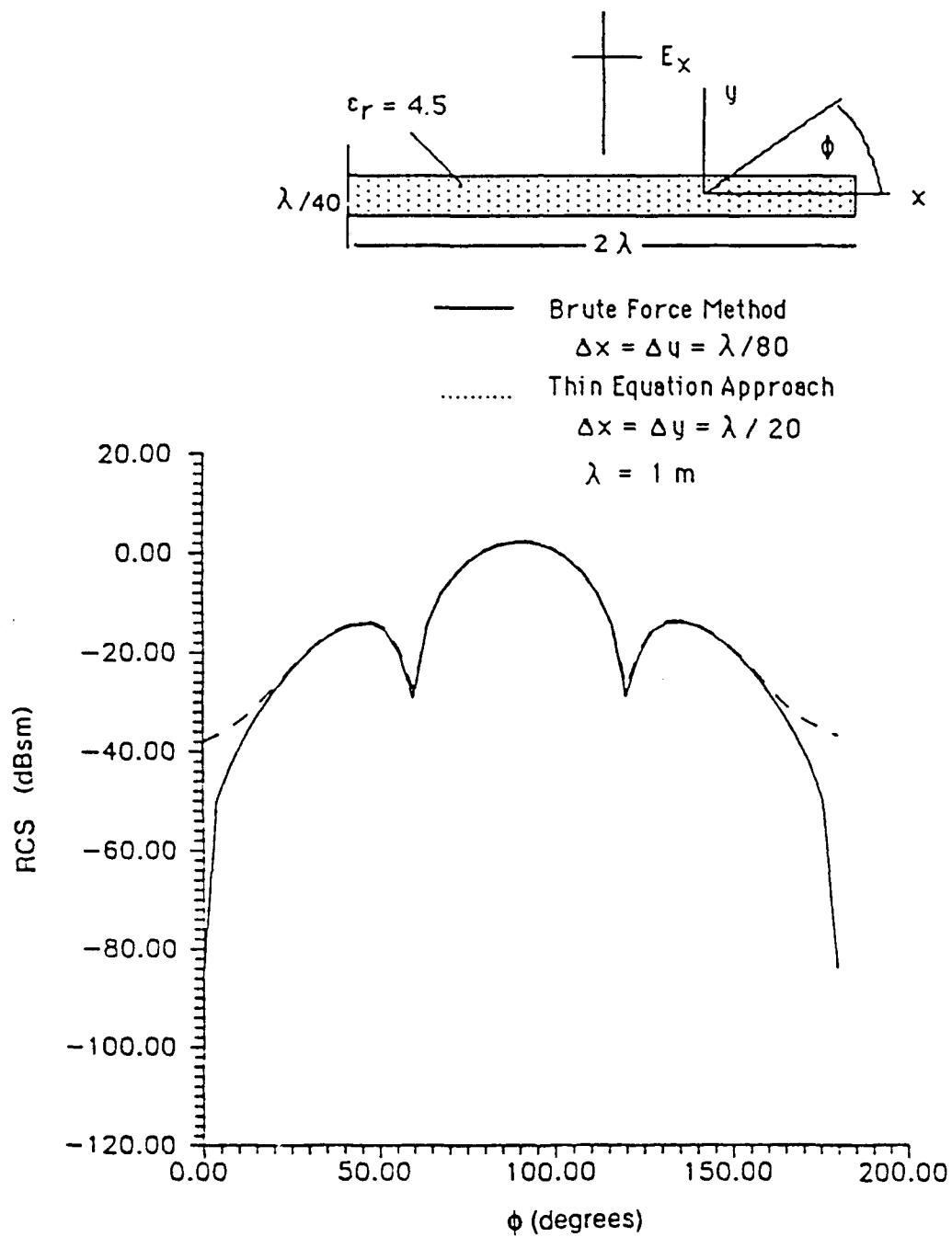
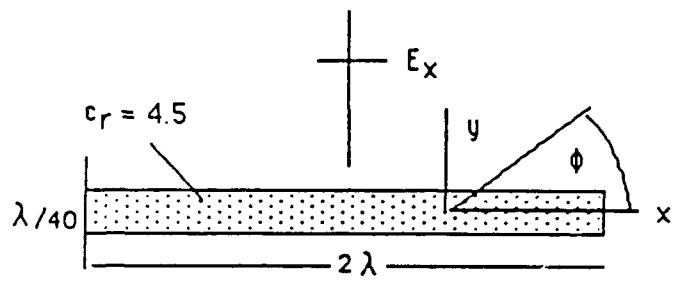


Figure 4.7 RCS of a lossless dielectric slab versus the observation angle obtained using the brute force and thin equation approaches (TE Polarization).



— Brute Force Method
 $\Delta x = \Delta y = \lambda / 80$
 XXXX Thin Equation Approach
 $\Delta x = \Delta y = \lambda / 20$
 $\lambda = 1 \text{ m}, |E^i| = 1$

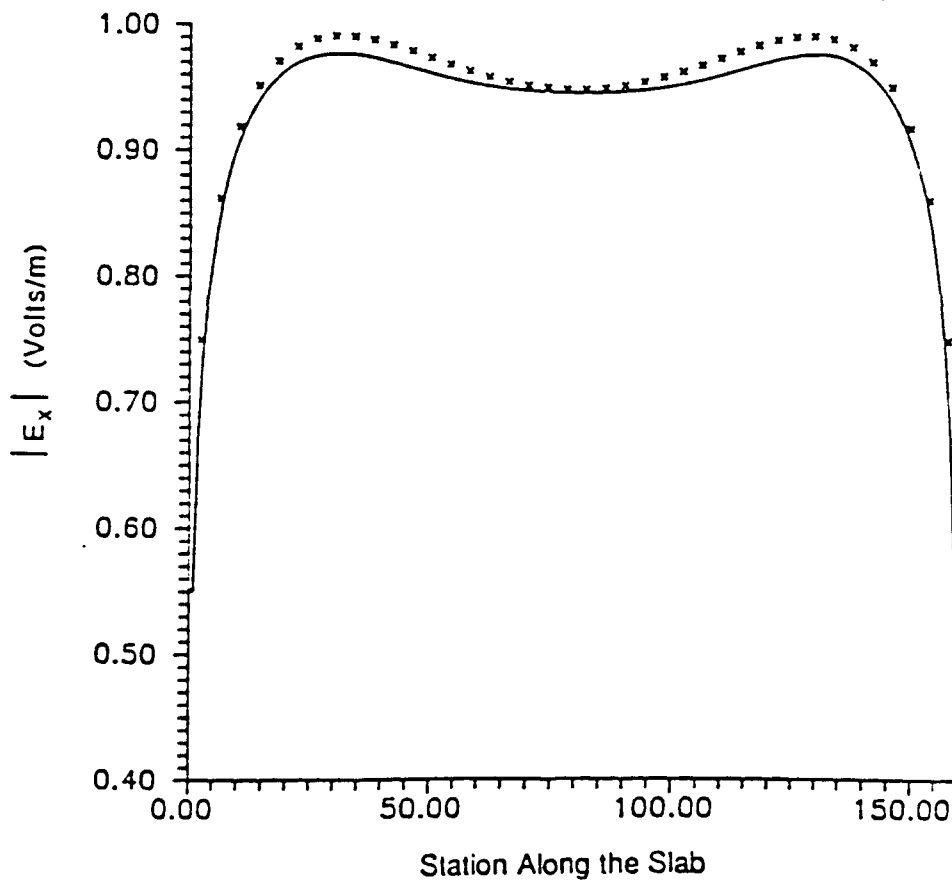


Figure 4.8 Near fields of a lossless dielectric slab versus the the position along the slab obtained using the brute force and thin equation approaches (TE Polarization).

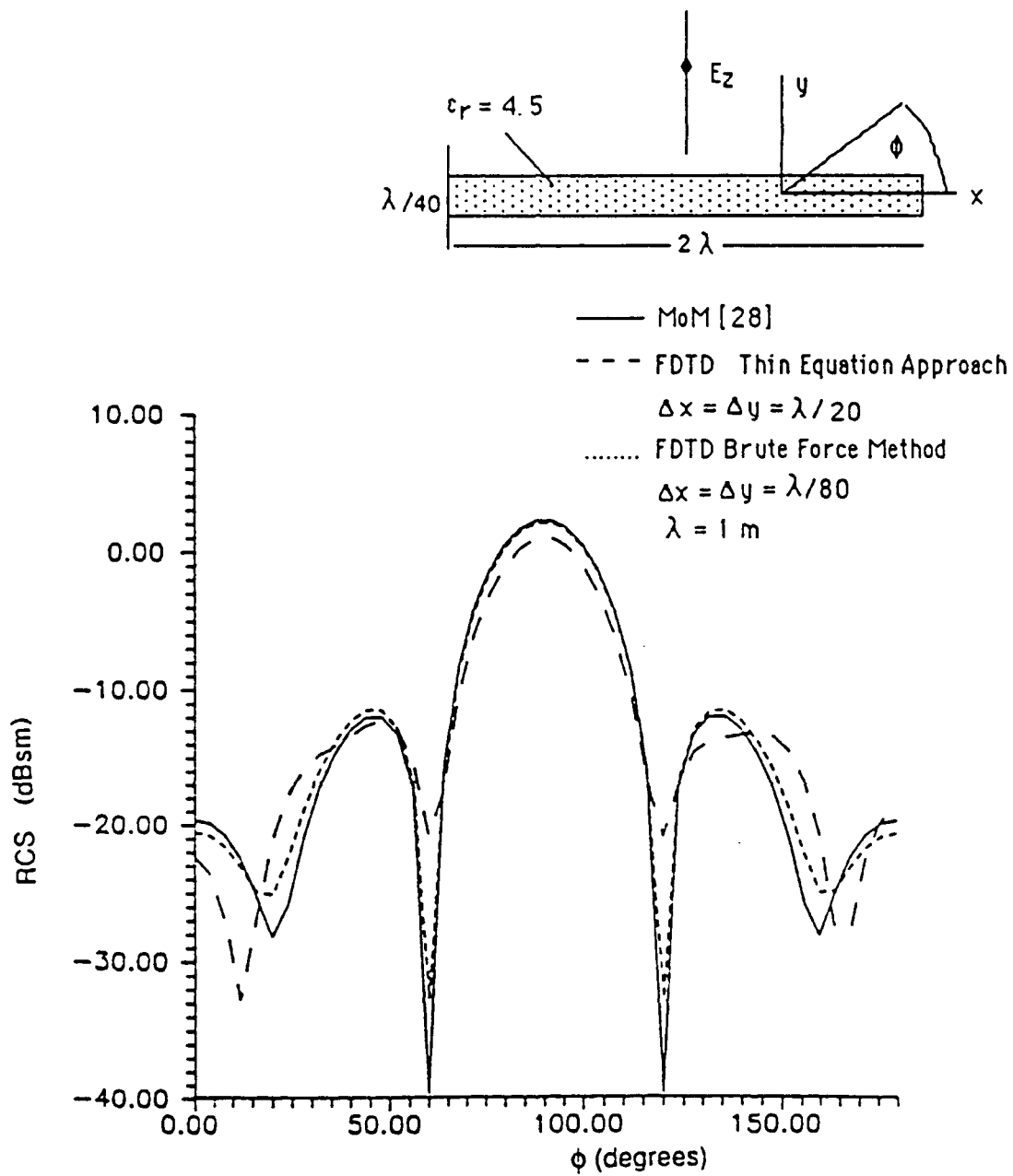


Figure 4.9 RCS of a lossless dielectric slab versus the observation angle obtained using the thin equation approach and the MoM (TM Polarization).

material that is not accounted for in the theoretical model. Instead of a linear distribution with a constant slope above and below the slab, it has a linear distribution but with a different slope above and below the dielectric material.

Figure 4.10 compares the RCS of a lossless to a lossy dielectric slab. The lossy dielectric slab projects a higher radar cross section than the lossless dielectric slab, especially at normal incidence. The lossless slab has a lower RCS than the lossy one because it allows the electromagnetic energy to propagate through without much reflection. On the other hand, the lossy dielectric slab is a better reflector of the electromagnetic energy.

Finally, figure 4.11 shows the transient backscatter from a three-dimensional thin dielectric plate of size 16m x 16m x 0.5m, and $\epsilon_r = 4.5$. This example compares the thin equation approach, the brute force method, and the physical optics method. The incident pulse is also shown in this figure. Note that the physical optics results lie between the results obtained using the thin equation approach and those obtained from the brute force method. For more scattering results obtained using a three-dimensional FDTD code, refer to [4].

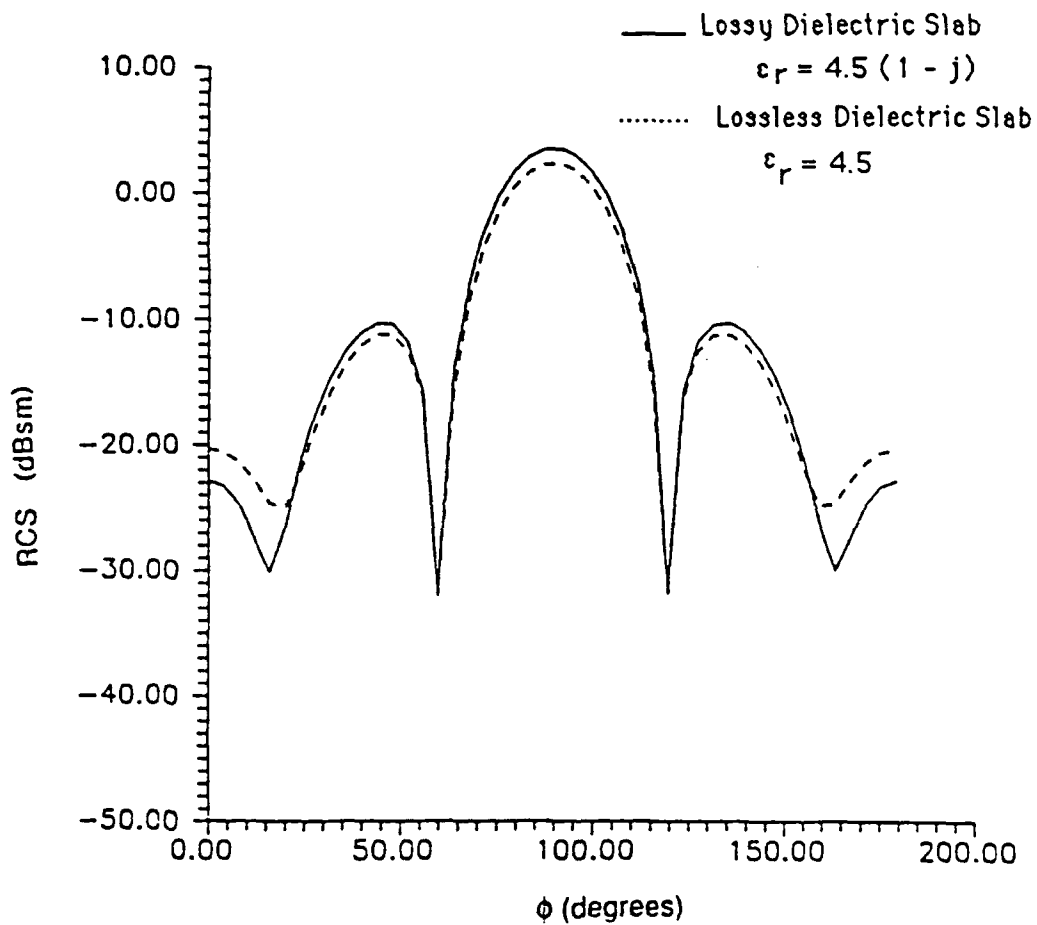
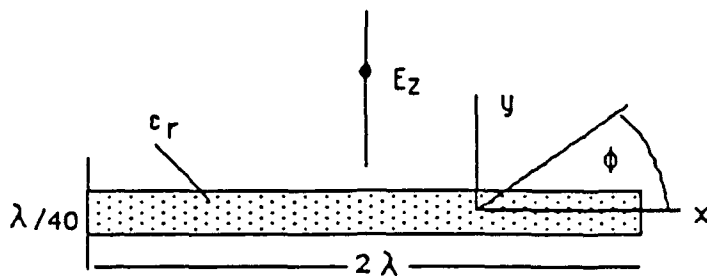


Figure 4.10 RCS of a lossy and lossless dielectric slab versus the observation angle obtained using the brute force method (TM Polarization).

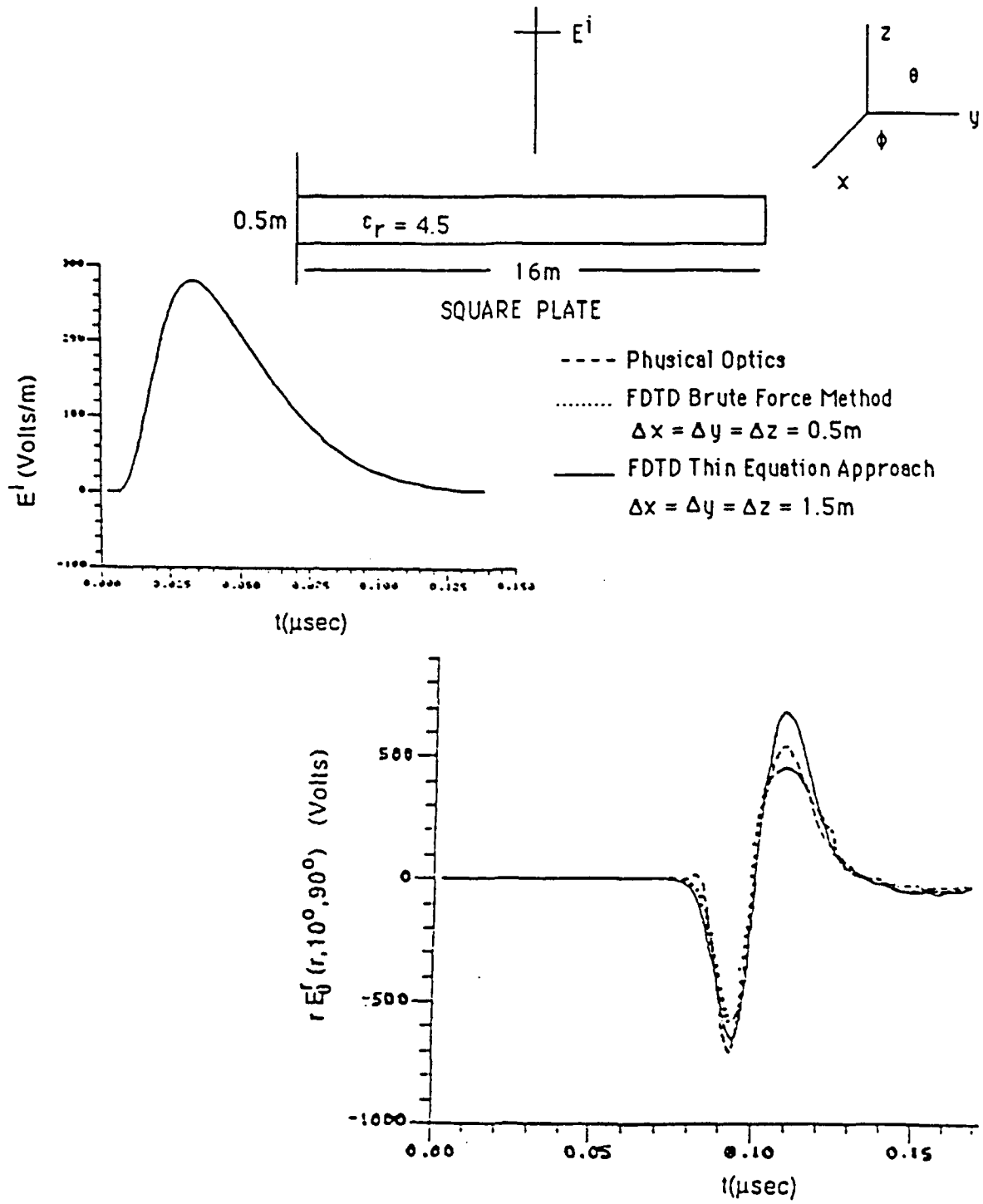


Figure 4.11 Transient backscattering from a three-dimensional thin plate.

Chapter 5: Modeling of Conductor-Backed Dielectrics

5.1 Introduction

The problem of electromagnetic scattering from structures coated with dielectric and/or magnetic materials has been studied for many years by using exact (series), approximate (high frequency, low frequency) and numerical techniques [26]. Exact analytical solutions have been derived for simple scatterers such as circular cylinders coated with lossy dielectric material [27]. An asymptotic high frequency estimation of monostatic radar cross section of a finite planar metallic structure coated with lossy dielectric material is obtained theoretically in [26]. The results are compared with experimental data, showing good agreement. Single-layered and multi-layered coated surfaces have been investigated using a transmission line approach [28].

Three major numerical methods that are applicable to scattering by layered dielectric materials are the Method of Moments (MoM), the Finite Element Method (FEM), and the Finite-Difference Time-Domain technique. In a recent publication [29], a new set of integral equations with reduced unknowns (two unknowns instead of three) was derived for modeling two-dimensional nonhomogeneous composite structures. This new set of integral equations was then solved using the MoM. Also, solutions to scattering problems involving coated dielectrics have been obtained using a hybrid FEM [31].

In this chapter the FDTD technique is used to analyze electromagnetic scattering by coated dielectric sheets. This analysis is done in two ways: 1) very small cells are used to model the thin dielectric coating on the top of a perfect conductor, and 2) coarse cells that are bigger than the size of the coated dielectric structure are used. The first method is referred to as the "brute force" method, whereas the second method is referred to as the "thin-equation" approach. Using the first method the dielectric coating can be either lossless or lossy. Using the second method only lossless dielectric coatings are considered.

5.2 Brute Force Method

Modeling of composite structures, such as coated dielectrics, is implemented in FDTD using a brute force method as shown in figure 5.1. In this figure the dielectric sheet is represented by the shaded region, whereas the conducting sheet is shown as the line beneath the dielectric.

Since the dielectric material occupies full cells, updating the electric and magnetic fields within these cells is done as in section 4.2, where bare dielectric sheets are analyzed. However, at the conductor/dielectric interface the proper boundary conditions on the magnetic and electric fields must be applied. These call for zero tangential electric fields and zero normal magnetic fields. Once the proper boundary conditions on the conductor/dielectric interface are applied, accurate modeling of coated dielectric sheets is obtained using the brute force method.

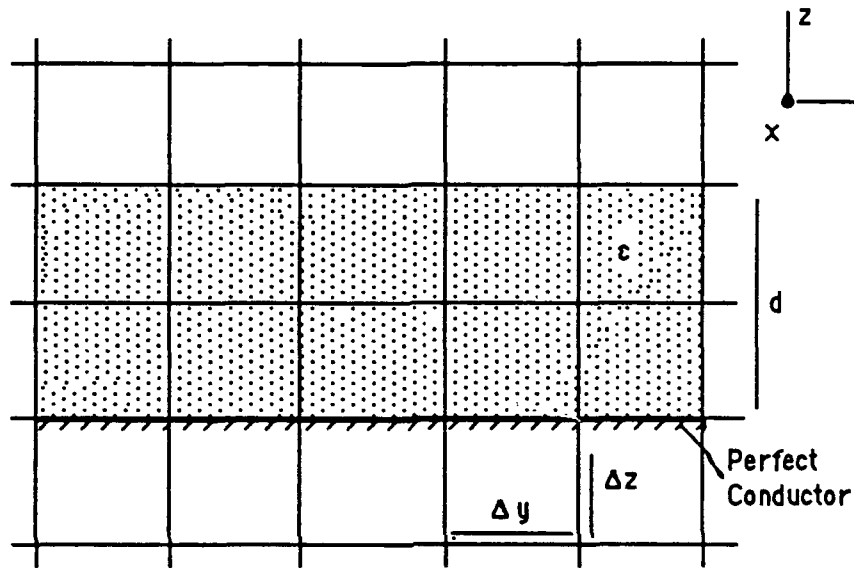


Figure 5.1 Brute force modeling of a dielectric sheet backed by a perfect conductor

5.3 Thin Conductor-Backed Dielectric Sheets

Modeling of thin dielectric slabs backed by a vanishingly thin conducting sheet is, in some ways, easier than modeling a thin dielectric slab. This is because the tangential electric and normal magnetic fields at the dielectric/conductor interface are known (i.e., they are zero).

The FDTD model for a thin, conductor-backed, dielectric sheet is shown in figure 5.2. The dielectric sheet is represented by the shaded region, whereas the conducting sheet is shown as the line beneath it. A typical contour used to evaluate the tangential electric fields at the air/dielectric interface is shown as C_1 . Here, the contour is shortened in the z -dimension as

compared to "normal" contours, due to the presence of the conducting sheet at the bottom. Ampere's law can be utilized along this contour to evaluate E_x along the air/dielectric interface if assumptions are made about the behavior of E_x and H_z within and along the contour.

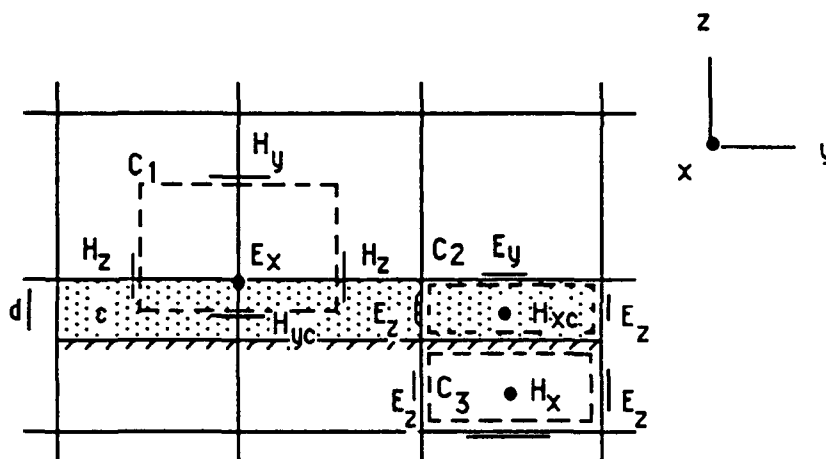


Figure 5.2 Orientation of a thin dielectric sheet backed by a perfect conductor

Since both E_x and H_z have zero values at the conductor surface and will vary linearly near and within the dielectric, H_z and E_x can be modeled as [2]

$$H_z = \begin{cases} 0 & -\frac{\Delta z}{d} < z < -d \\ H_z(I, J, K) \left[1 + \frac{z}{d}\right] & -d < z < \frac{\Delta z}{d} \end{cases} \quad (5.1)$$

and,

$$E_x = \begin{cases} 0 & -\frac{\Delta z}{d} < z < -d \\ E_x(I, J, K) \left[1 + \frac{z}{d}\right] & -d < z < \frac{\Delta z}{d} \end{cases} \quad (5.2)$$

where $H_z(I,J,K)$ and $E_x(I,J,K)$ represent the values of these fields at the air/dielectric interface. Also, z is measured with respect to the center of C_1 . Equations (5.1) and (5.2) are depicted in figure 5.3.

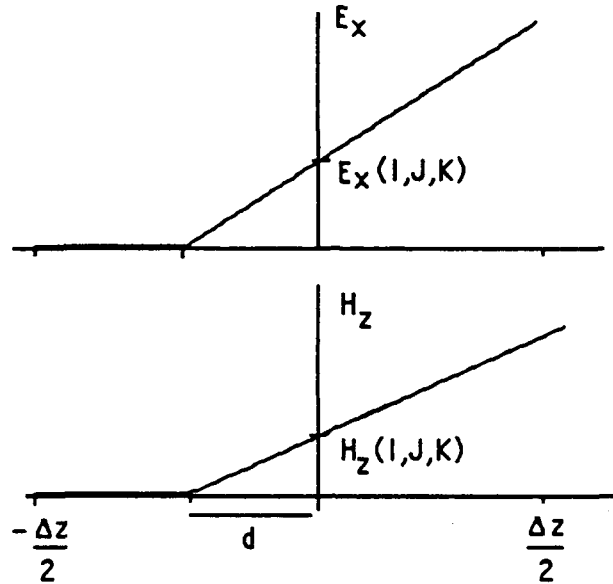


Figure 5.3 Assumed Variations along the z -direction of the tangential electric and normal magnetic fields.

Substituting (5.1) and (5.2) into Ampere's law (see equation 2.4a) and integrating about contour C_1 (see figure 5.2) one obtains

$$\begin{aligned}
 E_x^{n+1}(I,J,K) &= E_x^n(I,J,K) \\
 &- \frac{\Delta t}{\epsilon_0 \left[\epsilon_r \frac{3d}{8} + \frac{\Delta z}{2} + \frac{(\Delta z)^2}{8d} \right] \Delta y} \left\{ \left[H_z^{n+1/2}(I,J-1,K) \right. \right. \\
 &\quad \left. \left. + \left(\frac{\Delta z^2}{8d} + \frac{\Delta z}{2} + \frac{3d}{8} \right) - H_z^{n+1/2}(I,J,K) + \Delta z \right] \right. \\
 &\quad \left. + \left[H_y^{n+1/2}(I,J,K) - H_{yc}^{n+1/2}(I,J) \right] \Delta y \right\} \quad (5.3)
 \end{aligned}$$

where $H_{yc}(I,J)$ is the y -directed magnetic field in the middle of the dielectric material.

The x-directed magnetic field in the middle of the dielectric material can be updated by applying Faraday's law over contour C_2 . The assumption in this case is that the normal electric field within the slab equals the electric field above the slab multiplied by the constant $(1/\epsilon_r)$ to take care of the boundary conditions. This is a reasonable assumption because the normal electric field approaches the surface of the perfect conductor with a zero slope. Taking into consideration all the above assumptions, the equation for advancing the x-directed tangential magnetic field in the slab can be shown to be

$$H_{xc}^{n+1/2}(I,J) = H_{xc}^{n-1/2}(I,J) + \frac{\Delta t}{\mu} \left\{ \frac{\epsilon_0}{c \Delta y} [E_z^n(I,J,K+1) - E_z^n(I,J+1,K+1)] + \frac{1}{d} E_y^n(I,J,K+1) \right\}. \quad (5.4)$$

Similar equations for the y-directed electric and magnetic fields can easily be derived by following the same procedure.

The evaluation of H_z at the air/dielectric interface needs no special attention since the integration contour takes place for a fixed value of z and the fields H_z , E_x , and E_y are continuous across the interface. Finally, the expressions for updating the tangential magnetic field components (H_x and H_y) below the conductor must be slightly modified to reflect the fact that the conductor sheet is protruding into the cells under the slab. In evaluating Faraday's law around contour C_3 (see figure 5.3), it is noticed that the point at which H_x is to be evaluated is not the center of the contour, giving rise to an ambiguity in its value since the slope of H_x at that point cannot be known exactly. Fortunately, since this point is close to a perfectly conducting surface, the slope of H_x with respect to z will be small and thus relatively unimportant. Thus, the algorithm for calculating H_x needs only to be modified by noting that the surface surrounded by C_3 is smaller by the multiplier $(1 - d/\Delta z)$.

5.4 Numerical Results

Numerical results that validate the thin equation approach are presented in this section. Along with these results the effect of a lossy dielectric material on the RCS of a conductor-backed dielectric structure is examined.

Figure 5.4 shows the RCS versus the observation angle of a two-dimensional conductor-backed dielectric slab. The dimensions of the slab are $1\lambda \times \lambda/40$, while the relative dielectric constant of the coating is 10 (i.e, $\epsilon_r = 10$). Results obtained using the brute force method and thin equation approach show excellent agreement. However, this is somewhat due to the fact that the dominant scatterer in this case is the perfect conductor, which is modeled exactly by both methods. The contribution of the lossless dielectric material to the far fields is very small compared to that of the perfect conductor.

Very good agreement is also obtained in the near-field distribution of the same structure when the brute force method and thin equation approach are used. These results are compared in figure 5.5. Also, in this figure the differences between the fields of the conductor with and without the coating are shown. This accuracy in predicting the near fields of a conductor-backed dielectric slab using a coarse grid is very important for the next chapter where the thin equation model of cracks will be developed. The equations derived for the thin conductor-backed dielectric case will be utilized in the next chapter where cracks are analyzed.

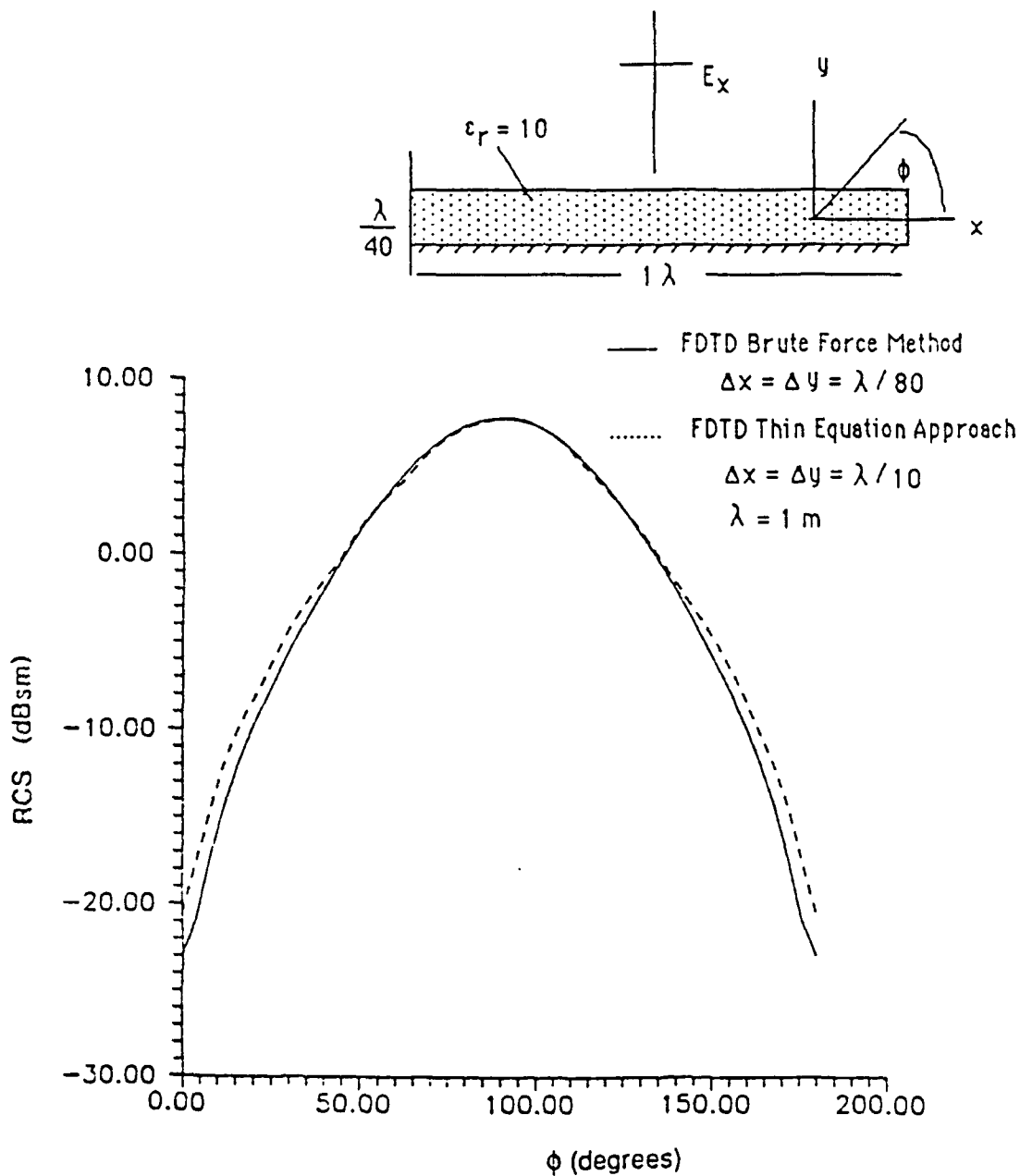


Figure 5.4 RCS of a lossless dielectric slab backed by a perfect conductor obtained using the brute force method and the thin equation approach (TE Polarization).

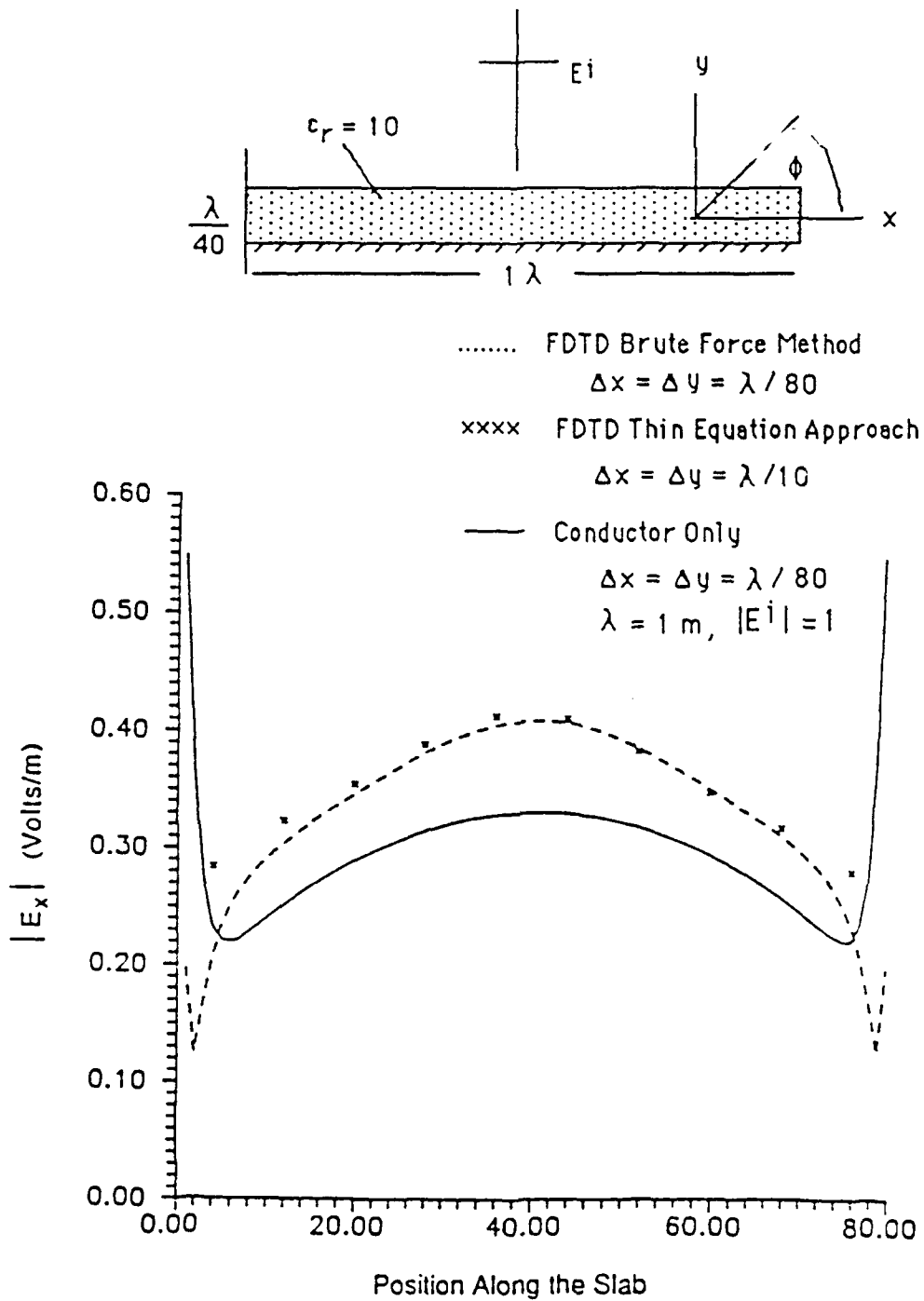


Figure 5.5 Near fields of a lossless dielectric slab backed by a perfect conductor versus the position along the slab. Also shown are the near fields of a bare perfect conductor sheet (TE Polarization).

These equations are used to update all the field points of the conductor-backed dielectric slab except those in the cell containing the crack.

Similar results for an oblique incidence angle (45 degrees) are exhibited in figures 5.6 and 5.7. In these examples, the relative dielectric constant was changed from 10 to 4.5. Good agreement is obtained in this case also between the brute force method and thin equation approach, both in the far fields and near fields. A cell size of $\lambda/20$ was used in this case, instead of $\lambda/10$ used in the previous example, to compensate for the additional numerical error introduced by dispersion effects. It is well known that the dispersion effect in the FDTD technique is known to be maximum when an oblique incidence angle of 45 degrees is used.

Figure 5.8 compares the RCS of a perfect conductor, when the conductor is bare, and when a thin layer of lossy dielectric material is deposited on top of it. The lossy dielectric material has an $\epsilon_r = 4.5 (1 - j)$. This figure illustrates that the RCS of the conductor is reduced by 3 dB at the maximum return point when the lossy coating of thickness $\lambda/20$ is deposited on its surface. These results were obtained using a TE polarized wave at an oblique incidence angle. Similar results at normal incidence are shown in figure 5.9.

The effect on the RCS of the conductor-backed dielectric slab when the polarization of the incident wave is changed is shown in figure 5.10. Less variation is exhibited in the RCS pattern for TM polarization than for TE polarization. Also, the RCS for TE polarization is lower than the one for TM polarization.

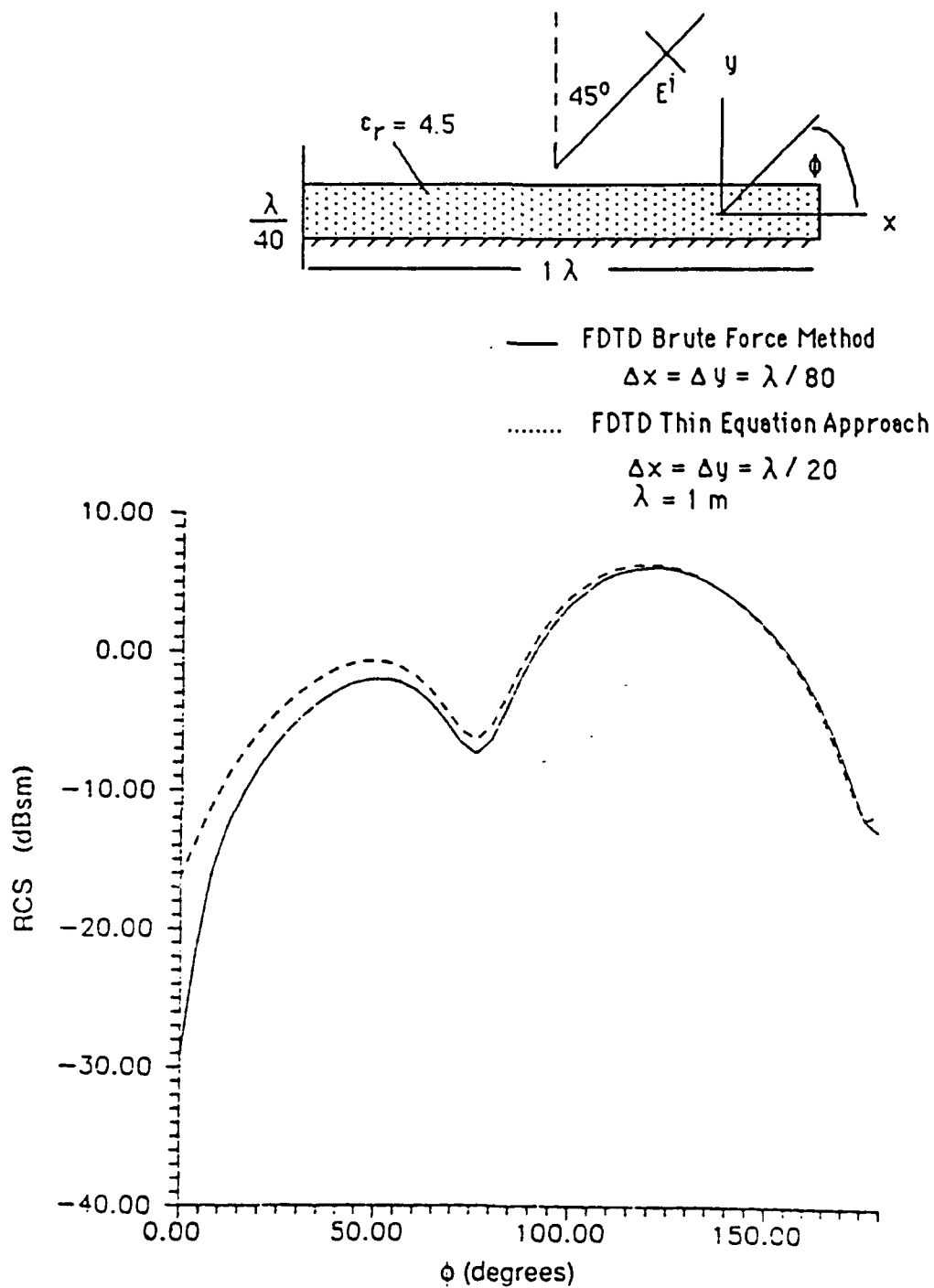


Figure 5.6 RCS of a lossless dielectric slab backed by a perfect conductor obtained using the brute force method and the thin equation approach (TE Polarization).

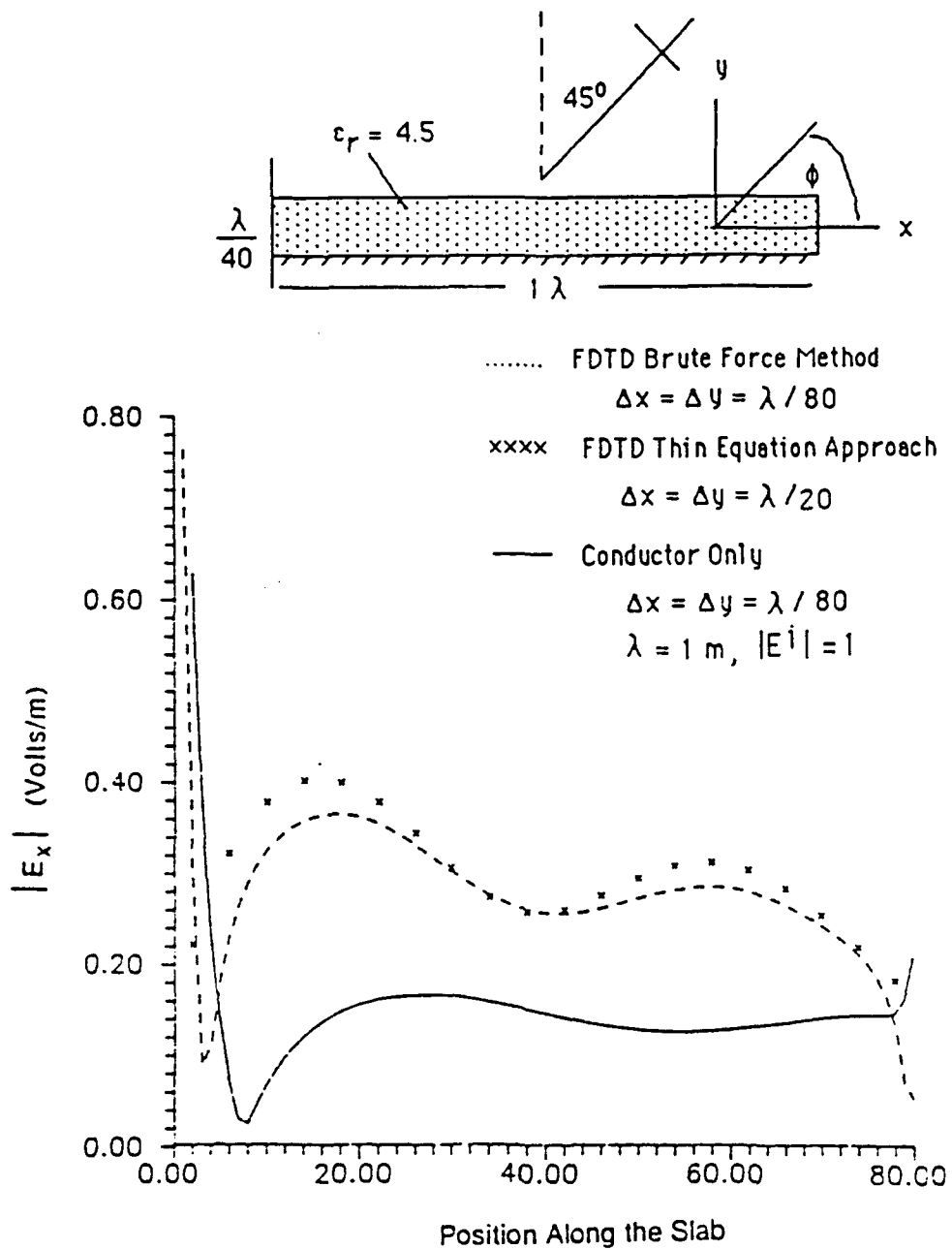


Figure 5.7 Near fields of a lossless dielectric slab backed by a perfect conductor versus the position along the slab. Also shown are the near fields of a bare perfect conductor sheet (TE Polarization).

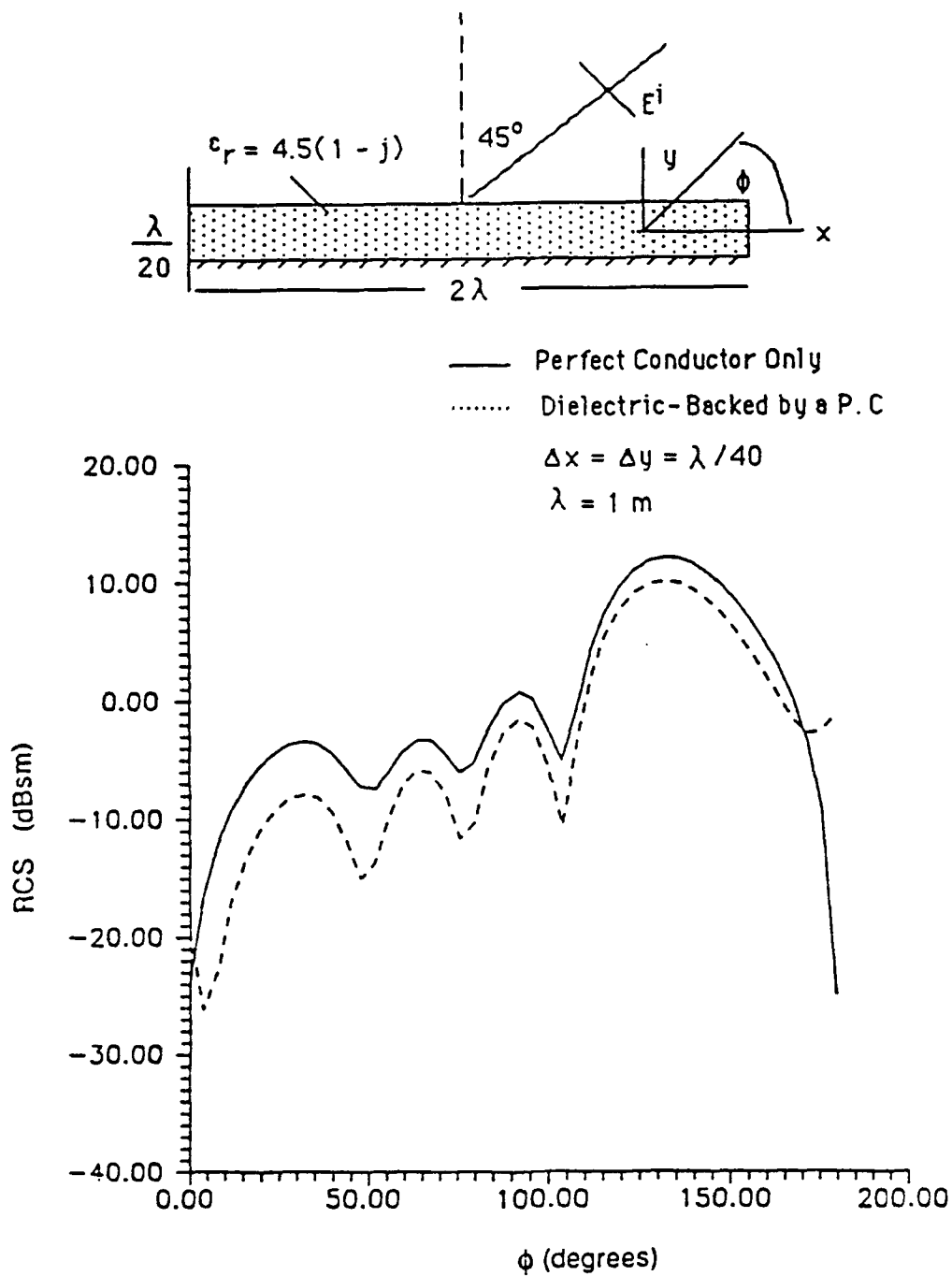


Figure 5.8 RCS of a lossy dielectric slab backed by a perfect conductor, with and without the dielectric coating versus the observation angle (TE Polarization).

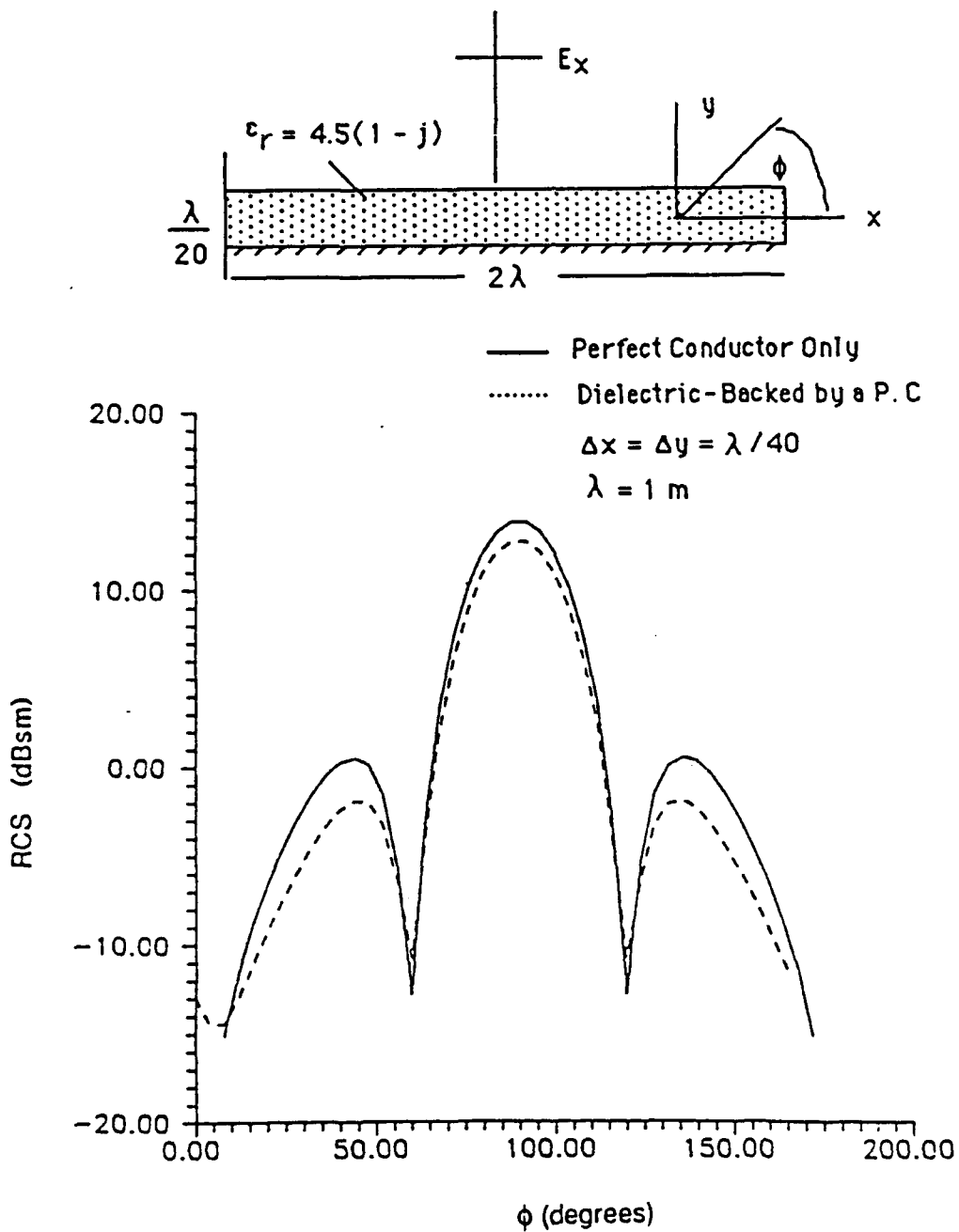


Figure 5.9 RCS of a lossy dielectric slab backed by a perfect conductor, with and without the dielectric coating versus the observation angle (TE Polarization).

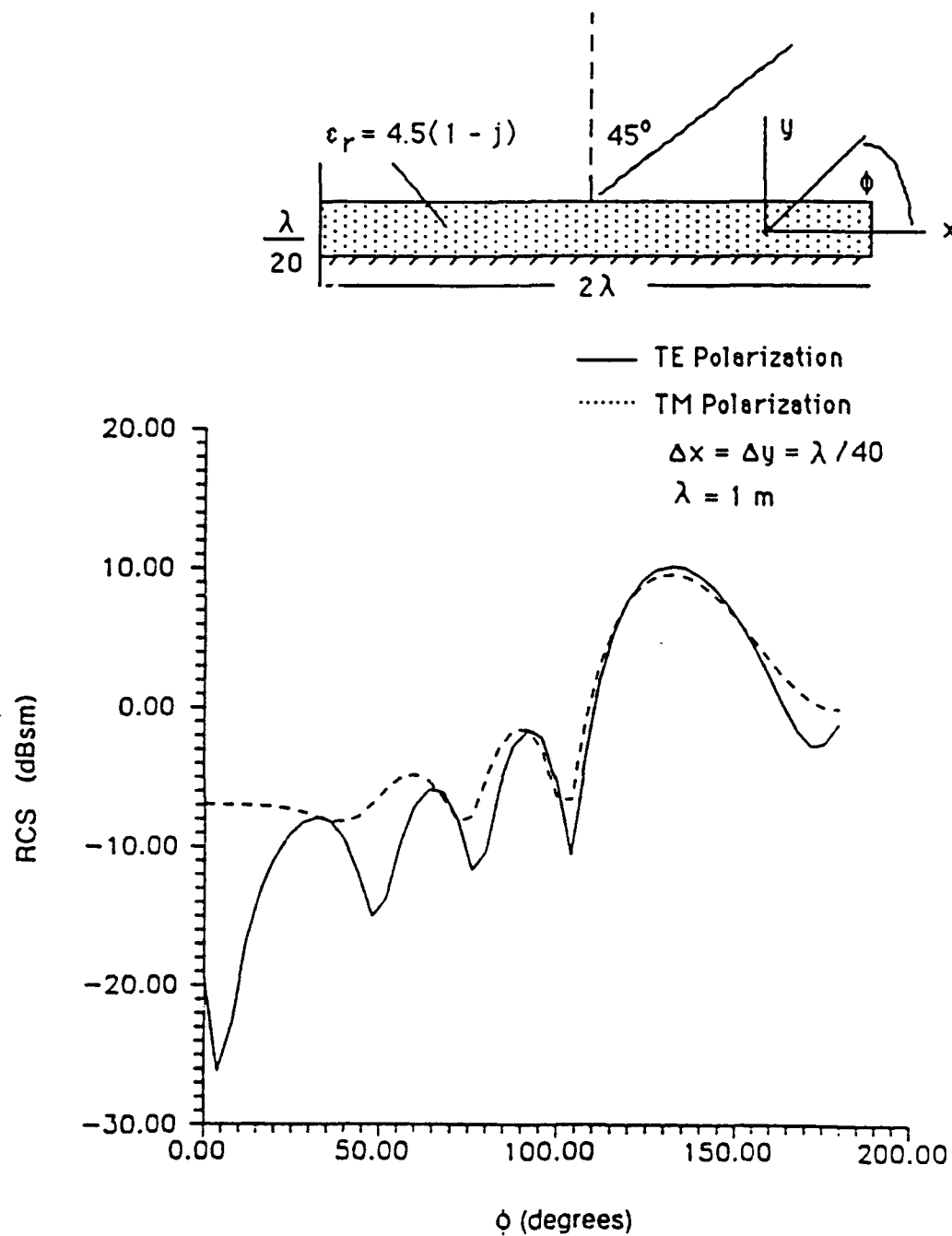


Figure 5.10 RCS of a lossy dielectric slab backed by a perfect conductor for TE and TM polarizations.

Chapter 6: Conductor-Backed Dielectrics With Cracks

6.1 Introduction

The problem of modeling a dielectric slab backed by a perfect conductor with a thin crack in the dielectric presents a challenge when using any electromagnetic technique. This difficulty arises from the relatively complex field distribution in the vicinity of the crack. These fields exhibit a severe localized perturbation from their smooth behavior away from the crack due to the collection of bound charges across the crack. The bound charge distribution can be thought of as arising from the disruption of polarization currents flowing within the dielectric since the crack presents an open circuit to these currents.

In this chapter, the scattering properties of such structures are analyzed using the FDTD technique in two different ways. First, the "brute force" method is applied, whereby the crack in the dielectric material is modeled using very small unit cells. This approach is applied only to two-dimensional structures because of the large computational requirements of three-dimensional analysis. Second, a "thin equation" approach is applied whereby the crack sizes are allowed to be smaller than the size of the unit cell of the FDTD grid. Derivations are first made for two-dimensional structures. Once the validity of the thin equation approach is established, the method is extended to model three-dimensional structures is straightforward.

6.2 Brute Force Modeling of 2-D Cracks

In section 5.2, a brute force method was applied to dielectric sheets backed by a perfect conductor. In this section, a similar approach is applied to dielectric sheets backed by perfect conductors with cracks in the dielectric material. Figure 6.1 shows the orientation of such a structure in the FDTD grid. In this figure, the dielectric material is represented by the shaded region, whereas the perfect conductor is shown as the line beneath the dielectric. The crack is assumed to be a "clean" cut in the dielectric sheet. The width of the crack is equal to a unit cell of the FDTD grid.

Using this method, any crack size, as well as dielectric thickness, can be selected by the user. Also, the dielectric material to be modeled can be either lossless or lossy. All these advantages, however, are obtained at the expense of bigger storage requirements and execution time. This is due to the fact that this model requires very fine resolution cells in order to analyze relatively thin cracks.

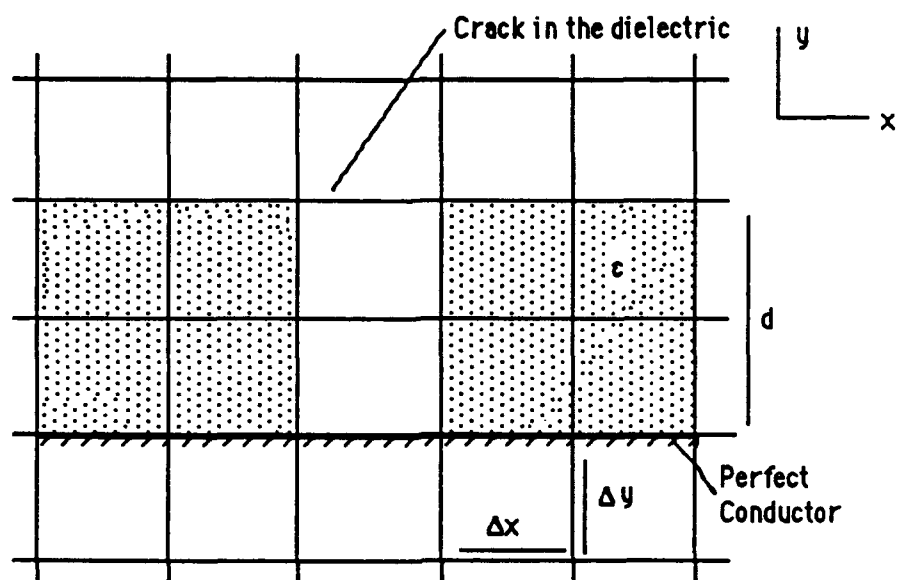


Figure 6.1 Orientation of a dielectric backed by a perfect conductor containing a crack in the dielectric material.

In order to study the effect of a relatively large crack (with respect to the free space wavelength) on the radar cross section of a conductor-backed dielectric slab, the simulation shown in figure 6.2 is performed. The thickness of the crack is equal to the thickness of the dielectric coating, i.e., $\lambda/5$, whereas its width is $\lambda/10$. The overall length of the conductor-backed dielectric slab is $2l$. TE polarization, at oblique incidence, is used. The RCS obtained with and without the crack in the dielectric is shown in this figure. A large perturbation in the RCS pattern is obtained when the crack is present in the dielectric material. In particular, a drop in the RCS is observed within the mainlobe of the pattern. On the other hand, a higher RCS within the sidelobe of the pattern is seen when the crack present.

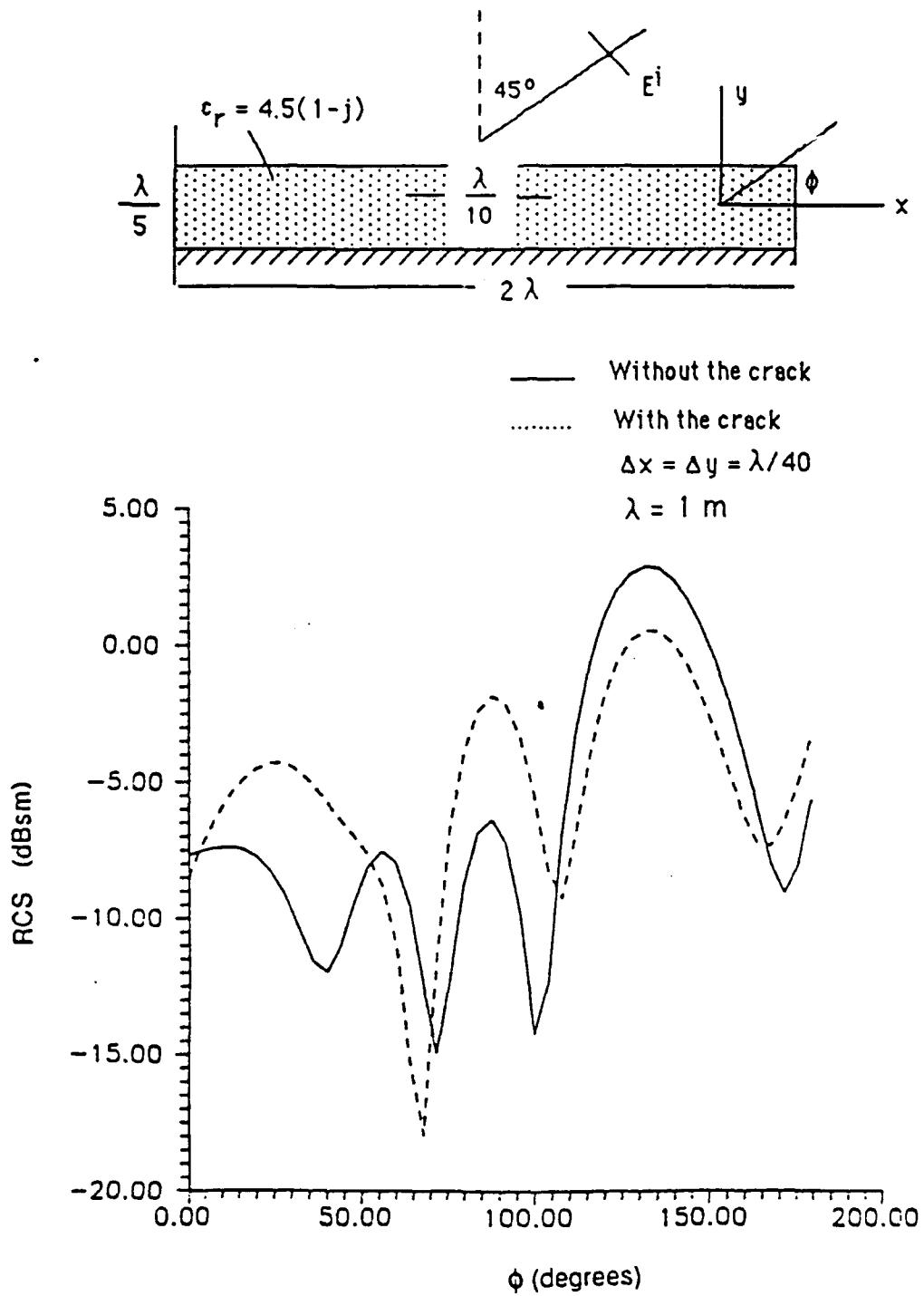


Figure 6.2 RCS of a conductor-backed dielectric slab with and without a crack in the dielectric material (TE Polarization).

In figure 5.8, the maximum RCS of a bare conductor of the same electrical size as the one used in this simulation is found to be 13 dBsm. When a lossy dielectric material of thickness $\lambda/20$ is deposited on its surface, it is found that the RCS of the structure is reduced by 3 dB at the maximum return point. In figure 6.2, where the thickness of the lossy dielectric coating is $\lambda/5$, the RCS is reduced by 10.5 dB. Furthermore, when a crack is artificially inserted in the dielectric material, the RCS is reduced by 12.5 dB. From this example it is reasonable to expect that there is an optimum crack width, and thickness, as well as an optimum number of cracks that can be used in a certain structure that will make the reduction in RCS maximum. Such an analysis is possible with the present FDTD code.

A second simulation is performed where the dielectric thickness, and hence the crack thickness, is decreased from $\lambda/5$ to $\lambda/20$. In the same way the width of the crack is decreased from $\lambda/10$ to $\lambda/20$. The results of the RCS pattern obtained with and without the crack in the dielectric are shown in figure 6.3. Absolutely no difference between the two curves is obtained in this case — the reason being the inability of the relatively small crack to contribute significantly to the far fields of the overall conductor-backed dielectric structure.

However, the fact that there is little effect in the RCS pattern of a 2-D conductor-backed dielectric slab because of the presence of a small crack in the dielectric material does not guarantee the absence of any effect in the near-field distribution of the tangential electric field along the surface of the dielectric. Indeed, when the amplitude distribution of the x-component of the electric field along the surface of the dielectric coating is compared with and without the crack, the effect of the crack is evident. This effect is shown in figure 6.4. A field perturbation is observed within the vicinity of the crack. This perturbation in the electric field is localized and does not contribute to the far-field radiation of the overall structure.

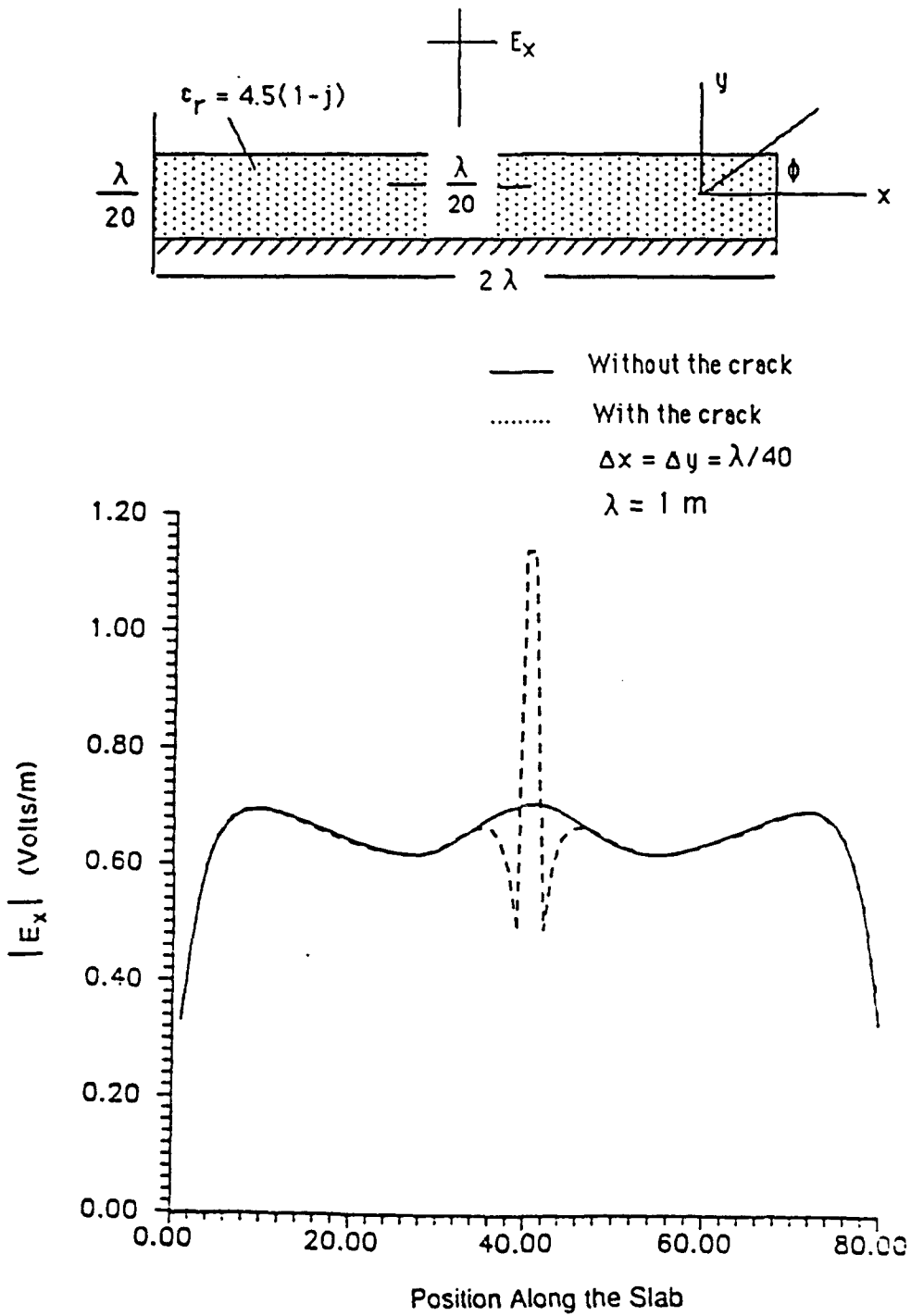


Figure 6.3 RCS of a conductor-backed dielectric slab with and without a crack in the dielectric material (TE Polarization).

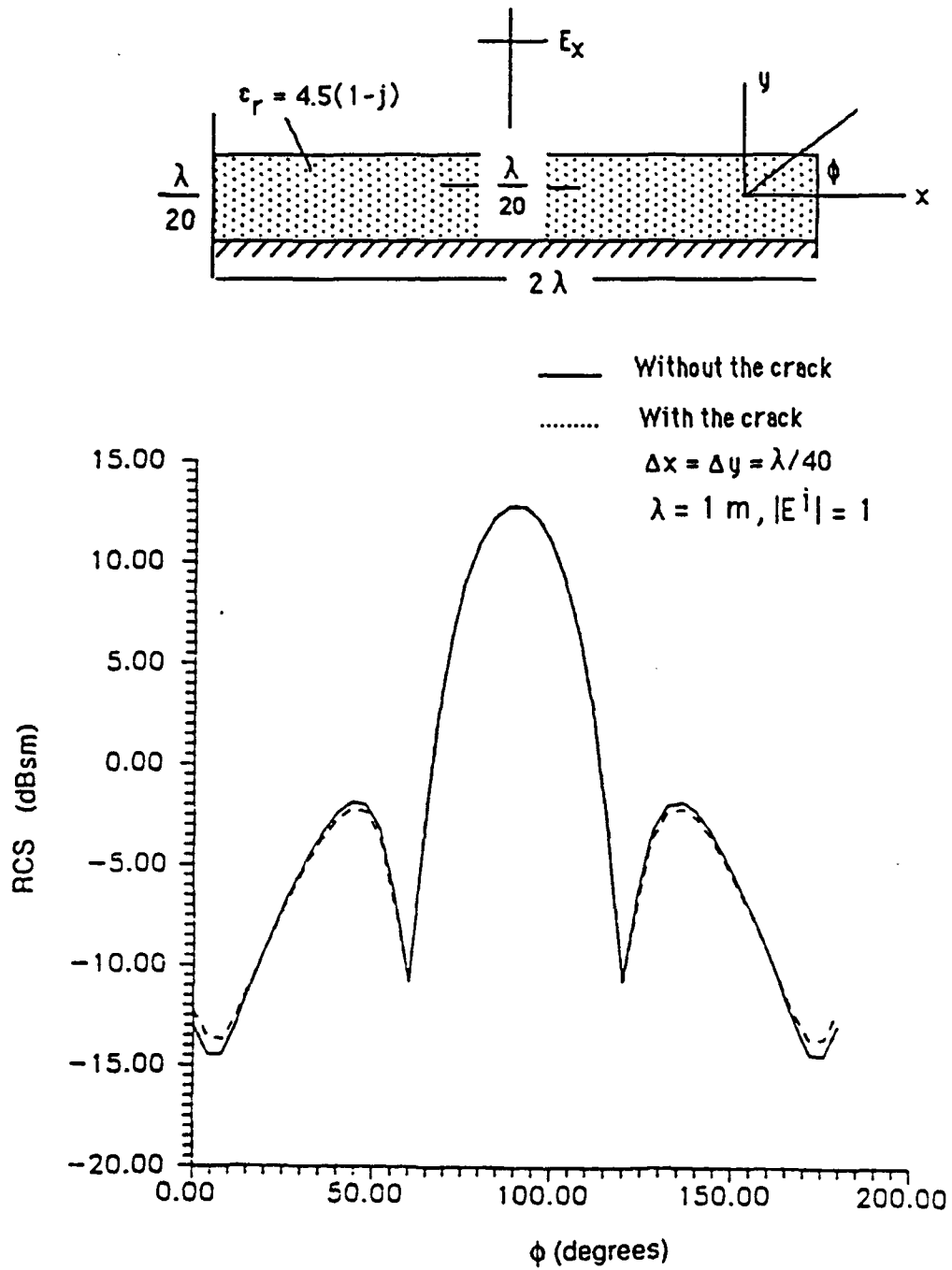


Figure 6.4 Near fields of a conductor-backed dielectric slab with and without a crack in the dielectric material (TE Polarization).

6.3 Two-Dimensional Thin Crack Model

A FDTD model of a dielectric slab backed by a perfect conductor with a narrow crack is shown in figure 6.5. Here, it is assumed that the air/dielectric interface lies along a grid coordinate axis, and the perfect conductor lies below at a depth d ($d < D_y$). The crack is assumed to be a "clean" cut in the dielectric, of width w ($w < D_x$), that extends through to the conductor surface. This alignment is such that the top of the crack coincides with the evaluation point of E_x . This particular orientation of the crack within the FDTD lattice has been chosen so that the effect of the crack can be most accurately modeled for situations where the incident field produces strong fields across the crack (i.e., TE polarization).

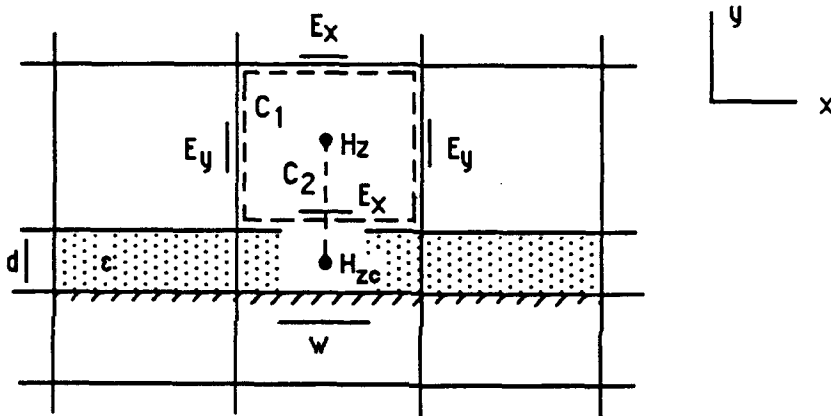


Figure 6.5 Orientation of a thin, conductor-backed dielectric slab with a narrow crack in the dielectric material.

Since the dielectric is non-magnetic, it can be assumed that the magnetic fields in its vicinity vary linearly throughout the cell. On the other hand, this assumption cannot be made about the tangential electric field in the vicinity of the crack since it is expected that this field component will be enhanced inside the crack and exhibit a disruption similar to a static dipole. This effect was shown in the previous section where the brute force method was used to analyze the near-fields of a crack (see figure 6.4).

This static dipole effect gives rise to two difficulties: 1) the nonlinear behavior of the field will change the way that the right-hand side of Ampere's law (equation 2.4a) is evaluated to calculate the field in the lattice point given a knowledge of its surface integral and, 2) it is not the value of $E_x(I,J)$ at the lattice point that is needed in Faraday's law when updating the magnetic

fields, but rather its line integral over the length of the respective cell wall. Thus, the nonlinear behavior of E_x along the x-direction must also be correctly modeled in order to calculate the magnetic fields accurately.

As was observed when using the brute force method, a relatively thin crack produces a localized perturbation in the tangential electric field in the vicinity of the crack. Since the perturbation is localized, a quasi-static approach can be followed to describe the nonlinear behavior of the tangential electric field.

The orientation of the crack, as well as the coordinate system used for the derivation of the crack model, is shown in figure 6.6. The center of the crack is defined as the origin of the coordinate system. The crack walls are at a distance $w/2$ away from the center. The perfect conductor lies at a distance d below the origin. The length of the conductor underneath is assumed to be much larger than the dimensions of the crack. A TE polarized incident field will produce x-directed polarization currents in the dielectric material. The intensity of these currents (i.e., $j\omega\epsilon_0(\epsilon_r-1)E$) will vary from a maximum value at the top surface of the dielectric to a zero value at the surface of the perfect conductor. Once these currents encounter the crack walls, they deposit bound charges on the respective walls of the crack. The charge distribution that is created will perturb the tangential electric field in the vicinity of the crack.

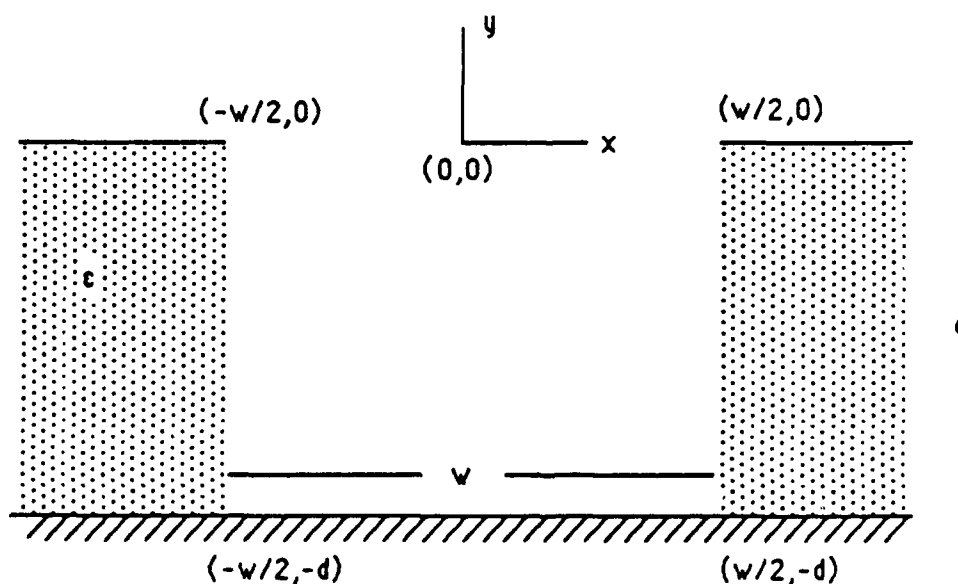


Figure 6.6 Enlarged geometry of a crack in the dielectric material.

Now that we have a physical understanding of the nonlinear behavior of the tangential electric field above the crack, we can assume a mathematical model that will describe this nonlinear behavior. This model is

$$E_x(x,y) = E_{xL} \left(1 + \frac{y}{d} \right) + E_{xNL} f(x,y) + Ax \quad , \quad (6.1)$$

where E_{xL} and A represent the linear behaviors of the field associated with the conductor-backed dielectric slab without the crack, in the y and x directions, respectively. The middle term, however, models the highly nonlinear dipole term. Here, $f(x,y)$ is a dimensionless dipole pattern function of the positive and negative charges on opposite sides of the crack, including the image due to the presence of the perfect conductor. E_{xNL} is the strength of this nonlinear field in volts/m.

Since the crack is located symmetrically about $x = 0$, the last term of equation (6.1) drops out when integrated across the cell from $-\Delta x/2$ to $\Delta x/2$. This, however, does not occur with the remaining two terms, leaving the apparent dilemma that the field model in the cell containing the crack is not uniquely specified since it contains two constants. This dilemma can be resolved, however, by realizing that the strength of the dipole term is directly related to the magnitude of the polarization charges deposited on the crack walls, which is in turn dictated by the electric field strength at the walls.

Starting with the relationship between the x -component of the total electric field just inside the left wall of the crack and the induced polarization current one obtains

$$J_{px}(-w/2^-, y) = (\epsilon - \epsilon_0) \frac{\partial}{\partial t} E_x(-w/2^-, y) \quad , \quad (6.2)$$

where $E_x(-w/2^-, y)$ is the electric field intensity just inside the left wall. Relating this polarization current to the surface charge density on the crack results in

$$J_{px}(-w/2^-, y) = \frac{\partial}{\partial t} \rho_s(-w/2^-, y) = (\epsilon - \epsilon_0) \frac{\partial}{\partial t} E_x(-w/2^-, y) \quad . \quad (6.3)$$

Dropping the time derivative from both sides of equation (6.3) results in

$$\rho_s(-w/2^-, y) = (\epsilon - \epsilon_0) E_x(-w/2^-, y) \quad (6.4a)$$

The line charge distribution on the crack wall can be found by integrating the surface charge distribution over the length of the crack wall in the y direction. Evaluating this integral results in

$$\begin{aligned} \rho_s(-w/2^-) &= \int_{-d}^0 (\epsilon - \epsilon_0) E_x(-w/2^-, 0) dy \\ &\approx \frac{1}{2} (\epsilon - \epsilon_0) [E_{xL} + E_{xNL} f(-w/2^-, 0)] \quad (6.4b) \end{aligned}$$

Here, it has been assumed that the functional behavior of $f(-w/2^-, y)$ with respect to y within the crack varies as $(1 + y/d)$, just as the linear field component. Also, we note that $f(x, y)$ is continuous at $y = 0$. Therefore, the surface charge distribution is proportional to the total electric field just inside the crack walls. But the nonlinear dipole strength, E_{xNL} , is also proportional to the charge distribution on the crack, and thus is also proportional to the quantity $[E_{xL} + E_{xNL} f(-w/2^-, 0)]$. Choosing the constant of proportionality between the nonlinear dipole strength and the total electric field just inside the wall to be unity (this forces E_{xNL} to be the total electric field just inside the crack wall) and evaluating these quantities at $y=0$, one obtains

$$E_{xNL} = E_x(-w/2^-, 0) \quad (6.5)$$

Substituting $E_x(-w/2^-, 0)$ in equation (6.5) in terms of E_{xL} and E_{xNL} , we can relate the constants E_{xNL} and E_{xL} as follows:

$$E_{xNL} = \frac{E_{xL}}{1 - f(-w/2^-, 0)} \quad (6.6)$$

Replacing (6.6) into (6.1), one obtains

$$E_x(x,y) = E_{xL} \left[1 + \frac{y}{d} + \frac{f(x,y)}{1 - f(-w/2^-, 0)} \right] \quad (6.7)$$

We have now expressed the functional behavior of $E_x(x,y)$ above the crack with respect to one unknown only.

Realizing that the FDTD technique updates average values of electric and magnetic fields, we must express the unknown constant E_{xL} in terms of the average value of $E_x(x,0)$. Now, the average value of $E_x(x,0)$ from $-Dx/2$ to $Dx/2$ is defined as

$$\begin{aligned} \langle E_x(x,0) \rangle &= \frac{1}{\Delta x} \int_{-\frac{\Delta x}{2}}^{\frac{\Delta x}{2}} E_x(x,0) dx \\ &= E_{xL} \left[1 + \frac{\langle f(x,0) \rangle}{1 - f(-w/2^-, 0)} \right] \end{aligned} \quad (6.8)$$

$$\text{where } \langle f(x,0) \rangle = \frac{1}{\Delta x} \int_{-\frac{\Delta x}{2}}^{\frac{\Delta x}{2}} f(x,0) dx$$

Solving (6.8) for E_{xL} and replacing E_{xL} in (6.7), the following final equation for $E_x(x,y)$, in terms of the average value of $E_x(x,0)$, is obtained:

$$E_x(x,y) = \frac{\langle E_x(x,0) \rangle}{1 + \frac{\langle f(x,0) \rangle}{1 - f(-w/2^-, 0)}} \left[1 + \frac{y}{d} + \frac{f(x,y)}{1 - f(-w/2^-, 0)} \right] \quad (6.9)$$

In order to derive the function $f(x,y)$, we refer to equation (6.4a), which relates the surface charge distribution with the total electric field just inside the crack walls. Since the dielectric

thickness is small ($d < 1/20$), the distribution of $E_x(-w/2^-,y)$ in the y direction can be assumed to be linear with respect to y . This linear behavior is described by the relationship

$$E_x(-w/2^-,y) = E_x(-w/2^-,0) \left[1 + \frac{y}{d} \right] \quad (6.10)$$

where $E_x(-w/2^-,0)$ is the field at the corner. Note that $E_x(-w/2^-,y)$ becomes zero at the surface of the perfect conductor for which $y = -d$.

By evaluating $E_x(x,y)$ using equation (6.1) at $x = -w/2^-$ and $y = 0$ (neglect the term "Ax") and solving the resulting equation for E_{xNL} , it can be shown that: $E_x(-w/2^-,0) = E_{xNL}$. Therefore, the constant E_{xNL} equals the total tangential electric field at the upper left corner of the crack. Substituting (6.10) into (6.4a) results in

$$\rho_s(-w/2^-,y) = (\epsilon - \epsilon_0) E_{xNL} \left[1 + \frac{y}{d} \right] dy \quad (6.11)$$

The same distribution, but of opposite sign can be obtained on the right wall of the crack. The function $f(x,y)$ is the pattern function of the surface charge of strength equal to $(\epsilon - \epsilon_0)(1 + y/d)$ on the walls of the crack (opposite sign on each wall), including the images due to the presence of the conductor. The product of E_{xNL} and $f(x,y)$ represents the total radiated field due to the bound charge on both sides of the crack. For two-dimensional problems it is desirable to express the surface charge distribution in terms of infinite lines of charge to avoid integrating in the z -dimension. Therefore, an incremental line of charge of infinite extent in the z -direction is: $d\rho_L = \rho_s dy$.

The radiated field due to an infinitely long line of constant charge is given by

$$dE_r = \frac{d\rho_L}{2\pi\epsilon_0 r} a_r \quad (6.12)$$

where

$$r = \sqrt{(x-x')^2 + (y-y')^2}$$

$$\text{and } a_r = \frac{(x-x')x + (y-y')y}{\sqrt{(x-x')^2 + (y-y')^2}}$$

In this case the primed coordinates represent the location of the source whereas the unprimed coordinates represent the location of the observer. Since we are interested in the x-component of the radiated electric field, equation (6.12) simplifies to

$$dE_x^r(x,y) = \frac{d\rho_L (x-x')x}{2\pi\epsilon_0 [(x-x')^2 + (y-y')^2]} \quad (6.13)$$

Replacing $dr_L = r_s dy' = (e - e_0)(1 + y'/d) dy'$ into (6.13) and rearranging, one obtains

$$dE_x^r(x,y) = E_{xNL} \frac{\epsilon_r - 1}{2\pi} \frac{\left(1 + \frac{y'}{d}\right) (x-x') dy'}{[(x-x')^2 + (y-y')^2]} \quad (6.14)$$

Equation (6.14) can be written in the form

$$dE_x^r(x,y) = E_{xNL} df(x,y) \quad (6.15)$$

$$\text{where } df(x,y) = \frac{\epsilon_r - 1}{2\pi} \frac{\left(1 + \frac{y'}{d}\right) (x-x') dy'}{[(x-x')^2 + (y-y')^2]}$$

In order to find the total radiated field along the cell wall that contains the crack, the function $df(x,y)$ has to be integrated over the whole charge distribution, including the charge images due to the presence of the perfect conductor. The functions $f(x,0)$ and $f(0,y)$ are required to implement equation (6.9) in the FDTD code. These functions can be derived in closed form by integrating $df(x,0)$ and $df(0,y)$ over the whole charge distribution. The derivation of these functions is included in the appendix. Also, another important parameter that is required by the FDTD code is the value of $f(-w/2,0)$ at the upper left corner of the crack. This parameter is also derived in the appendix.

$E_x(x,y)$ can now be updated in FDTD by applying Ampere's law over contour C_2 of figure 6.5. The final equation for updating the x-component of the electric field along the crack is

$$E_x^{n+1}(I,J) = E_x^n(I,J) + \frac{\Delta t}{\epsilon_0} (\text{Factor}) [H_z^{n+1/2}(I,J) - H_{zc}^{n+1/2}(I,J)] \quad (6.16)$$

$$\text{where Factor} = \frac{1 + \frac{\langle f(x,0) \rangle}{1 - f(-w/2,0)}}{\frac{\Delta y}{2} + \frac{\Delta y^2}{8d} + \frac{3d}{8} + \frac{\langle f(0,y) \rangle \left(\frac{\Delta y + d}{2} \right)}{1 - f(-w/2,0)}}$$

$$\text{and } \langle f(0,y) \rangle = \frac{2}{\Delta y + d} \int_{-d/2}^{\Delta y/2} f(0,y) dy$$

$H_{zc}(I,J)$ is the value of the magnetic field in the center of the crack.

Once the correct average value of E_x is estimated, the application of Faraday's law over contour C_1 (see figure 6.5) will correctly update the x-component of the magnetic field above the crack. The remaining fields are updated as in the conductor-backed dielectric case.

In order to check the validity of this thin equation approach, two simulations of conductor-backed dielectric slabs containing narrow cracks in the dielectric coating are performed. The first simulation models a dielectric coating of thickness $\lambda/50$, containing a crack of width $\lambda/100$. The overall length of the slab is 0.95λ . These dimensions are selected such that the crack lies exactly in the center of the slab. The plot shown in figure 6.7 represents the amplitude distribution of the tangential electric field on the surface of the dielectric material, obtained using both the brute force method and thin equation approach. The amplitude of the electric field above the crack, as

provided by the thin equation approach, represents the average over the cell containing the crack. This is because every sample point produced by the thin equation approach corresponds to five sample points of the brute force method (the ratio of the respective unit cell sizes is 1:5).

Although it first appears from figure 6.7 that the thin equation approach has failed to correctly predict the behavior of the field in the vicinity of the crack, we note that with a knowledge of the correct value of the average electric field over the cell containing the crack and using equation (6.9), the actual electric field distribution over the unit cell length, Δx , can be obtained. This field distribution, along with the five samples of the brute force method, is shown in figure 6.8. In this case 500 sample points of the function $f(x,0)$ are used and therefore 500 sample points corresponding to one unit cell of length $\lambda/20$ are obtained. To generate five sample points corresponding to the five samples of the brute force method, the actual distribution of figure 6.8 is averaged over every 100 sample points. These 5 samples are compared in table 5.1 with those obtained using the brute force method. The relative error between the values obtained using the two different methods is also tabulated. The maximum relative error obtained is 2.34% indicating that the thin equation approach updates correctly the average value of the tangential electric field above the crack.

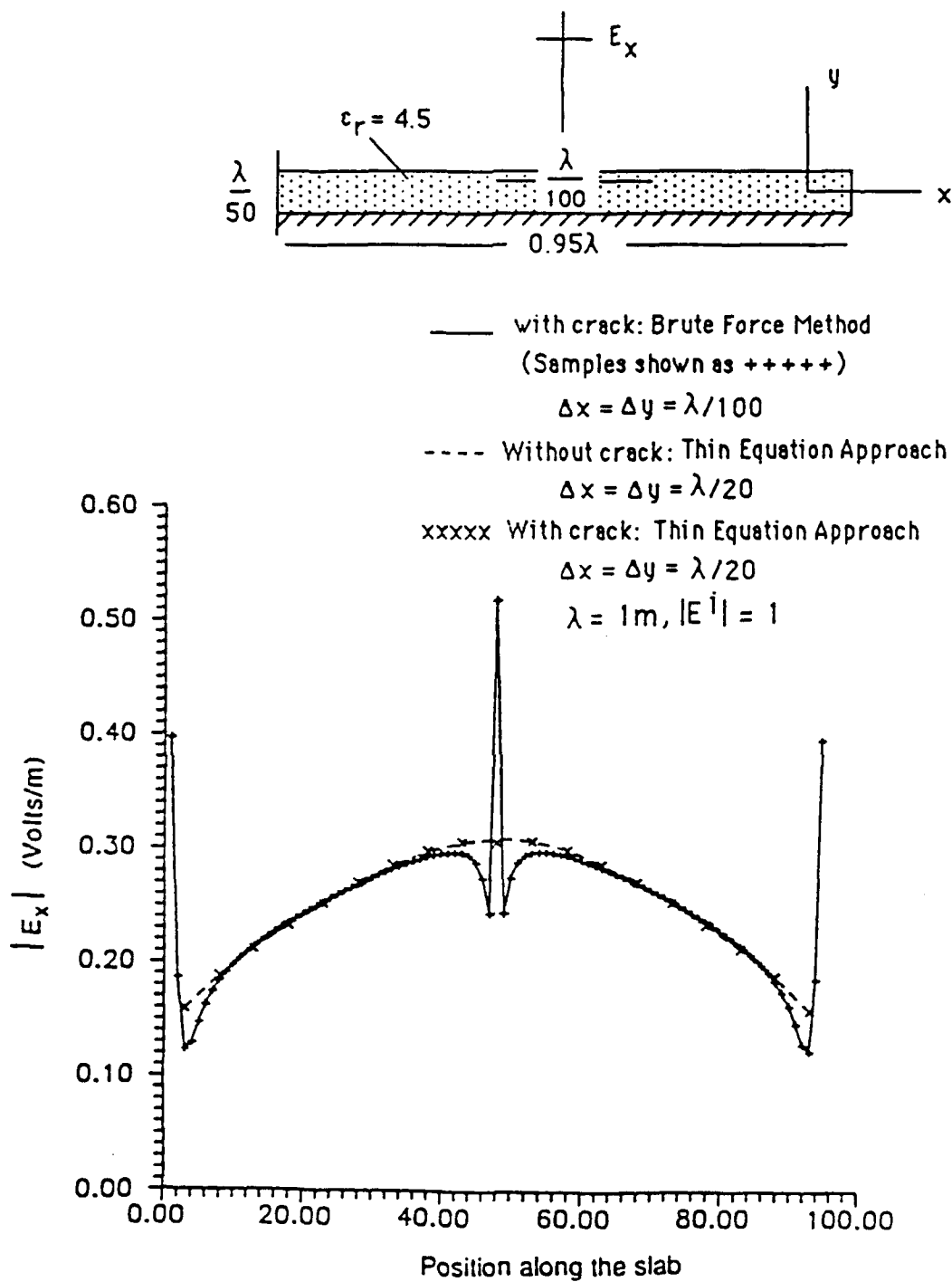


Figure 6.7 Near-field distribution of the tangential electric field along the surface of the dielectric material (TE Polarization)

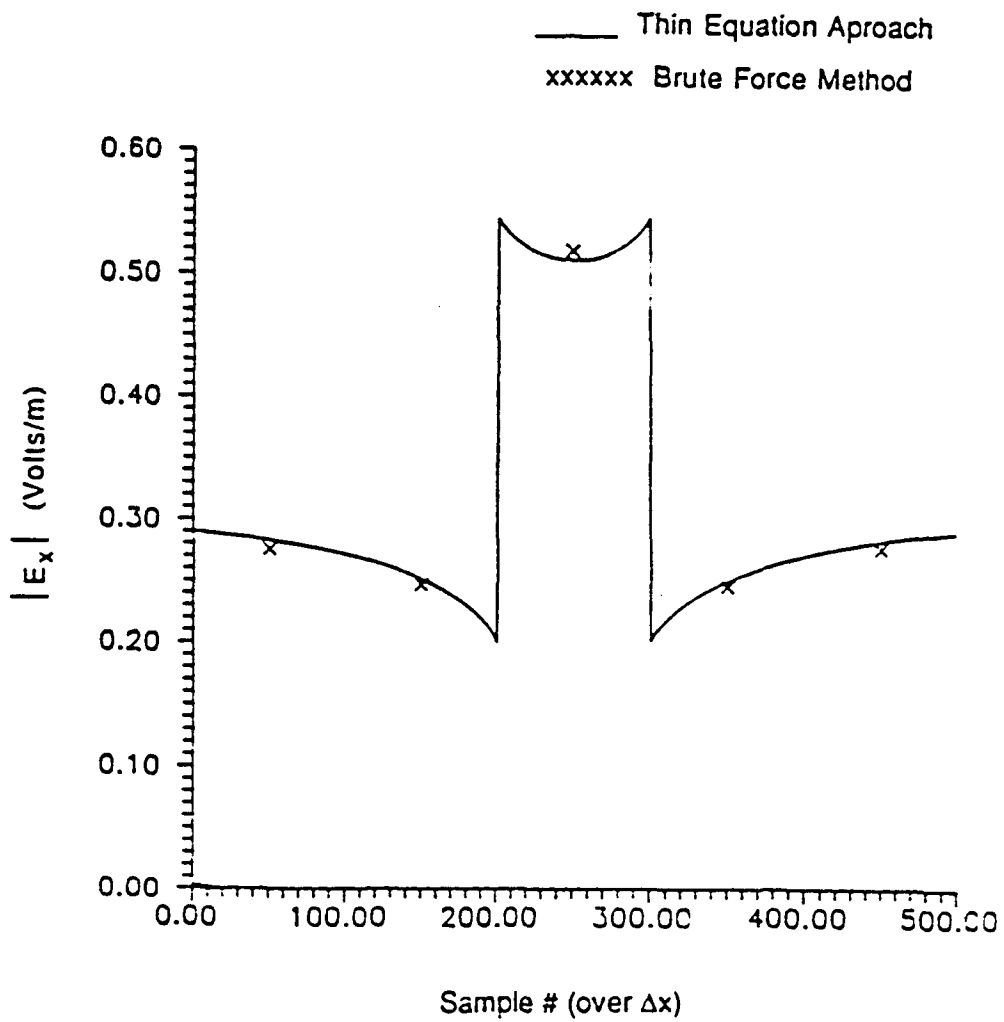


Figure 6.8 Near field distribution of the electric field above the crack predicted by the thin equation approach after relating the coarse cell average value to the total field expression (equation 6.9).

Table 6.1 Sample points of the electric field above the cell (s) of the crack.

Sample #	Brute Force E_x (v/m)	Thin Equation E_x (v/m)	Relative Error %
1	0.2753	0.2816	2.31
2	0.2447	0.2464	0.70
3	0.5190	0.5178	0.22
4	0.2447	0.2457	0.41
5	0.2753	0.2814	2.34

perturbation due to the crack is confined only within the cell containing the crack. To analyze the effect on the numerical error, the width of the crack is now increased and a second simulation is performed. While keeping the other parameters the same as in the previous example, the crack width is increased from $\lambda/100$ to $3\lambda/100$. The crack in this case occupies 60% of the unit cell when modeled using the thin equation approach. The tangential electric field distribution along the dielectric surface is shown in figure 6.9. In figure 6.10, the actual distribution of the field reproduced using its average value, along with the five sample points obtained using the brute force method, is shown. In the same way as in the previous example, 500 samples of the function $f(x,0)$ are used, and hence 500 samples of the field are obtained. When a 100 point averaging is performed on the actual distribution, 5 sample points are produced. These 5 sample points are compared in table 6.2 with the ones obtained using the brute force method. This comparison shows that the error increases as the width of the crack increases. This is so because for larger crack widths, the crack affects field points not only within the cell containing it but also within neighboring cells.

Table 6.2 Sample points of the electric field above the cell(s) of the crack.

Sample #	Brute Force E_x (v/m)	Thin Equation E_x (v/m)	Relative Error %
1	0.2241	0.2309	3.03
2	0.4091	0.3653	10.70
3	0.3752	0.3429	8.60
4	0.4091	0.3648	10.83
5	0.2241	0.2317	3.80

In conclusion, it has been shown that the thin equation approach can be applied to correctly model conductor-backed dielectric slabs containing cracks in the dielectric material as long as the crack width is confined to at least less than 40% of the length of the unit cell of the FDTD grid. To produce the actual distribution of the electric field above the crack, knowledge of the average value of the field, as well as the function $f(x,0)$ is required.

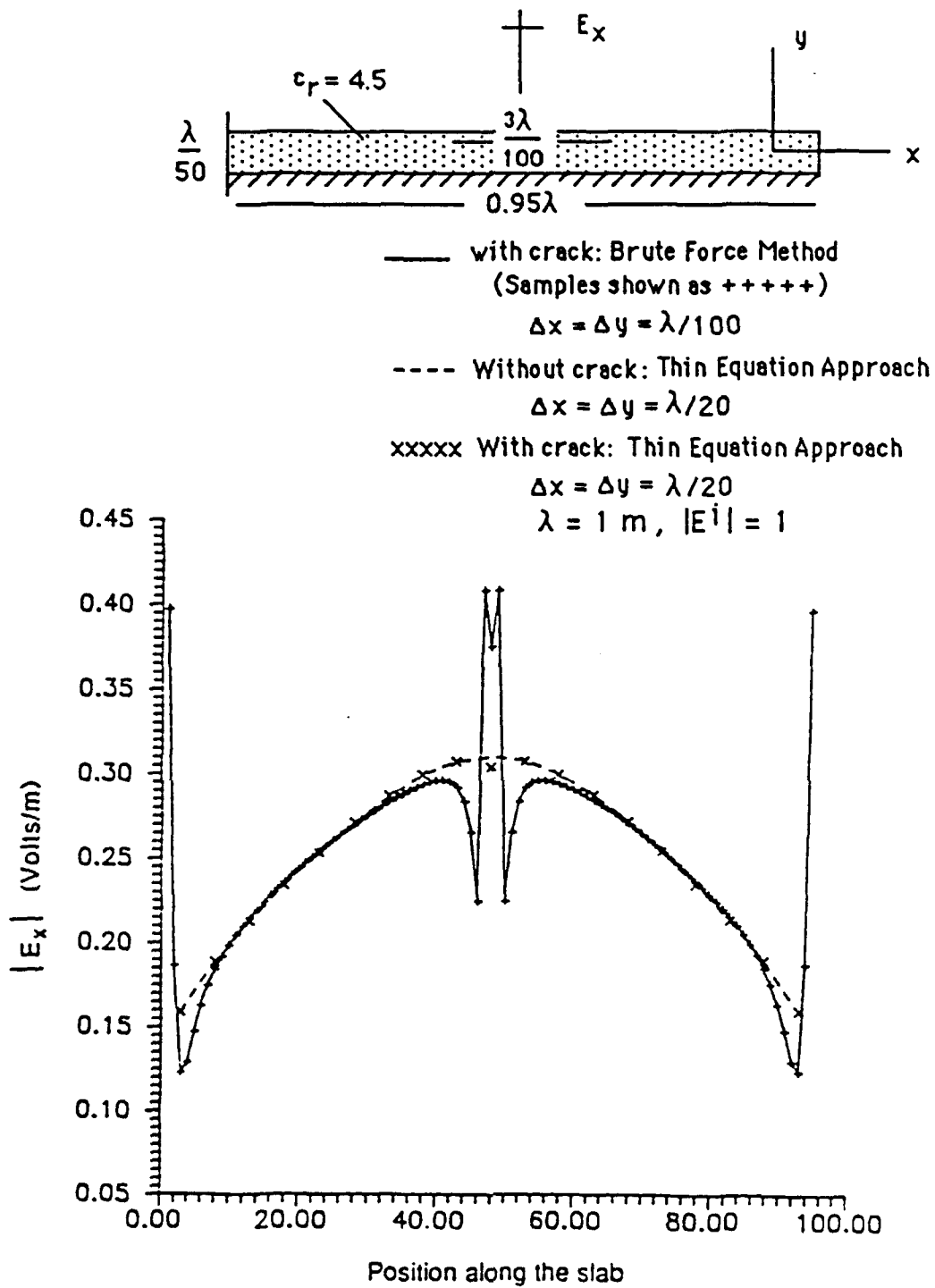


Figure 6.9 Near-field distribution of the tangential electric field along the surface of the dielectric material (TE Polarization).

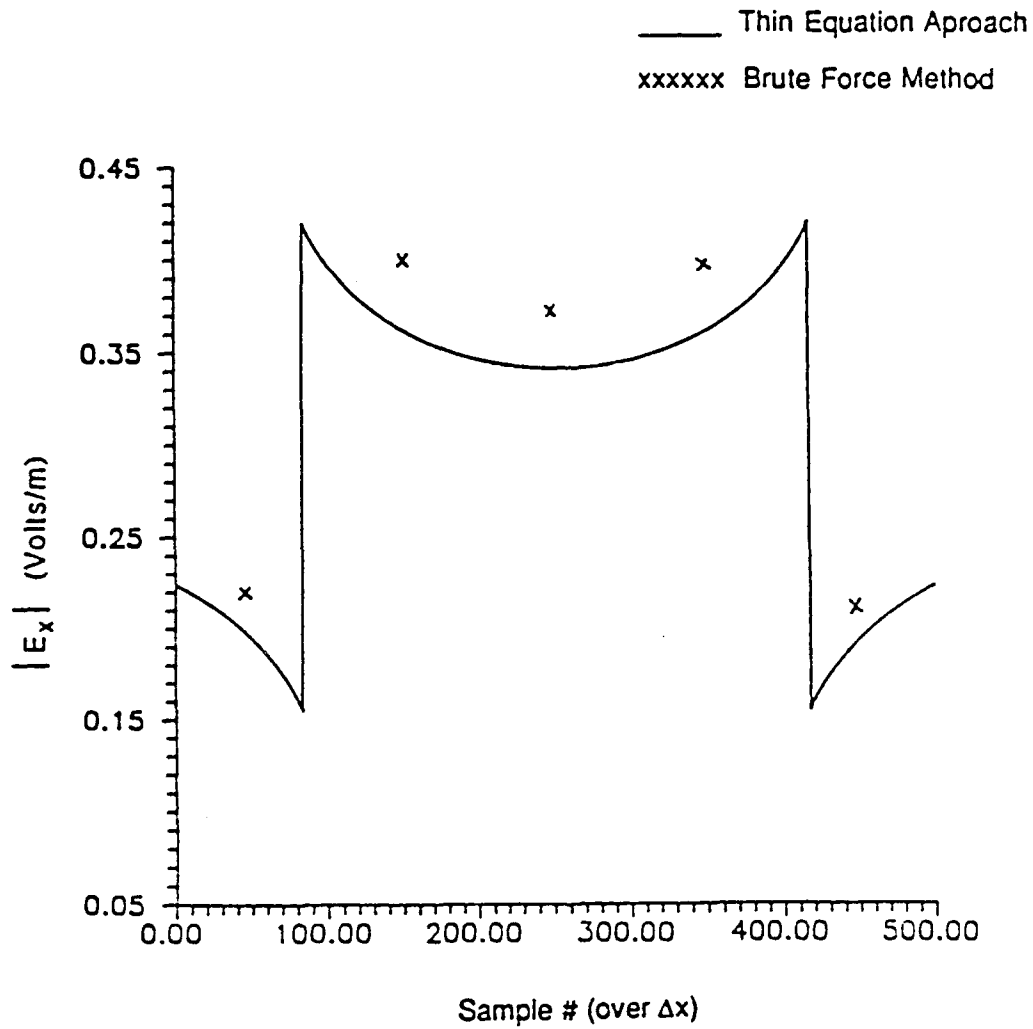


Figure 6.10 Near field distribution of the electric field above the crack predicted by the thin equation approach after relating the coarse cell average value to the total field expression (equation 6.9)

6.4 Three-Dimensional Thin Crack Model

A model of a three-dimensional dielectric plate backed by a perfect conductor with a long narrow crack in the dielectric material is illustrated in figure 6.11.

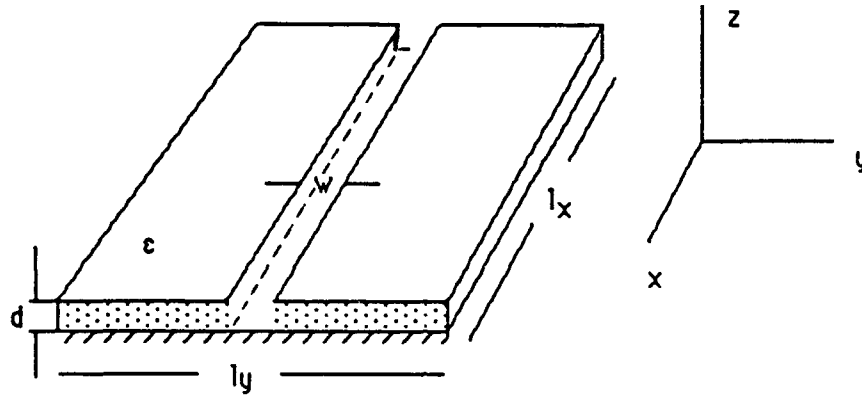


Figure 6.11 Three dimensional conductor-backed dielectric plate with a long narrow crack in the dielectric material.

A two-dimensional cut in the y - z plane of the conductor-backed dielectric plate with a crack is shown in figure 6.12. Also shown in this figure is the orientation of the structure with respect to the FDTD grid. Note that the plate and the crack are positioned in the same manner as in the two-dimensional case.

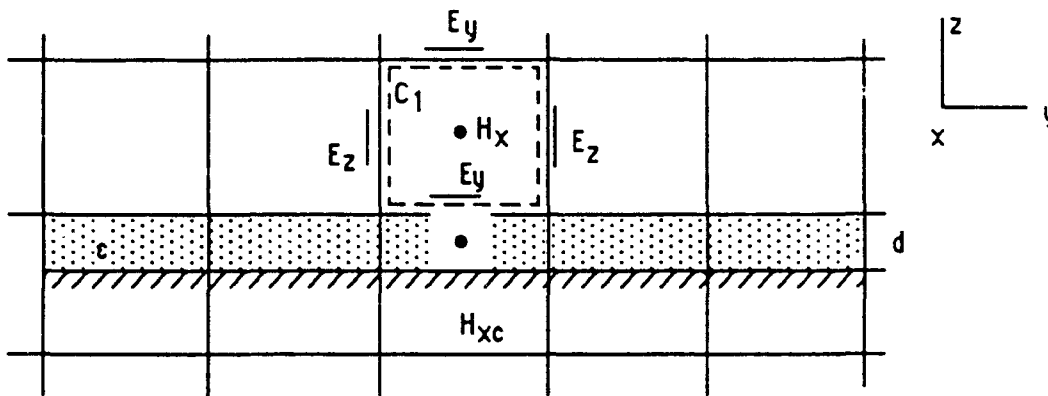


Figure 6.12 Orientation of a thin conductor-backed dielectric plate containing a crack in the dielectric material.

The mathematical model used for the y -component of the electric field above the crack is similar to the one derived for the two-dimensional crack. This model can be expressed as

$$E_y(x,y,z) = E_{yL} \left(1 + \frac{z}{d} \right) + E_{yNL} f(x,y,z) + Ax + By \quad (6.17)$$

It is expected that the same static dipole effect across the crack will be observed in this case also. The width of the crack is assumed to be at least less than 40% of the length of the unit cell. In this way, the perturbation in the electric field due to the crack is confined within the cell containing the crack (in the y direction). An enlarged pictorial representation of the three-dimensional crack with the coordinate system that is used for the derivation of the function $f(x,y,z)$ is shown in figure 6.13. Note that the length of the plate is l_x and l_y meters in the x and y direction respectively. The thickness of the crack is d , and its width is w .

Although the model used for the tangential component of the electric field across the three-dimensional crack is the same as that of the two-dimensional case, the derivation of the function $f(x,y,z)$ is done in a slightly different manner. This is because the dimensions of the crack are finite. Therefore, the infinite line of charge representation that was used in the two-dimensional case cannot be used here. The charge distribution over the finite area of the crack walls ($dA = dz dx$, see figure 6.13) will have to be integrated numerically in order to derive the function $f(x,y,z)$. The numerical integration that is introduced will significantly add to the overall cpu time required

to solve a given problem. In the two-dimensional case, because one dimension was of infinite extent, we were able to use the infinite line of charge representation and, hence, solve the problem by integrating over one dimension only.

A second problem is that image theory cannot be applied in this case because of the finite dimensions of the slab in the x direction. Image theory was used to find the image of the charge distribution due to the presence of the perfect conductor.

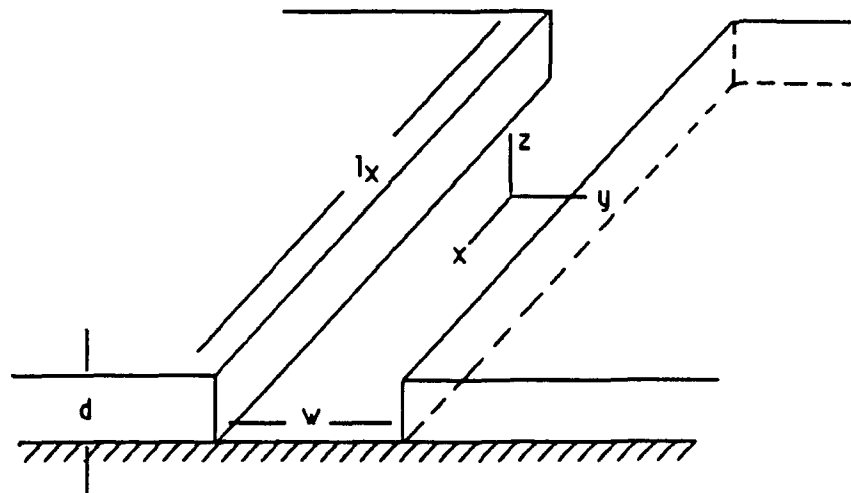


Figure 6.13 Enlarged geometry of a three dimensional crack.

A study concerning the first problem showed that for a unit cell size of the FDTD grid bigger than one meter, it is not required to integrate over the whole slab dimension (in the x direction) in order to get the exact radiated electric field over a unit cell. Integrating over a unit cell only is enough to provide the exact distribution of the radiated electric field. This is because the radiated electric field is inversely proportional to r^3 , r being the distance from the charge. For distances greater than one meter the radiated field becomes very small and hence insignificant. This observation simplifies the derivation of the function $f(x,y,z)$, and also reduces the cpu requirements.

Furthermore, if we assume that the charge distribution over a unit cell affects the y -component of the electric field inside that cell only, then image theory can be applied with no problem except at the edges of the slab (in the x -direction). This assumption is correct given that the length of the conductor-backed dielectric slab is much bigger than a unit cell in either the x or y direction. The error though due to the edges can be reduced by increasing the size of the slab in the x direction. This effect was observed in chapter 4 (see figure 4.6).

Therefore, assuming that a unit cell of length greater than one meter is used and that the dimension of the slab in the x direction equals several unit cells, it can be shown that

$$E_y^r(x, y, z) = E_{yNL}(0, -w/2, 0) * f(x, y, z) \quad (6.18)$$

$$\begin{aligned} \text{where } f(x, y, z) &= \int_0^{-2d} \int_{-\Delta x/2}^{\Delta x/2} df(x, y, z) dz' dx' \\ &= \frac{\epsilon_r - 1}{4\pi} \int_0^{-2d} \int_{-\Delta x/2}^{\Delta x/2} \frac{\left(1 + \frac{z'}{d}\right) \langle y - y' \rangle dz' dx'}{\left(\sqrt{(x - x')^2 + (y - y')^2 + (z - z')^2}\right)^3} \end{aligned}$$

Following almost the same procedure as in the two-dimensional case, the final equation for advancing the y-component of the electric field above a cell containing a three-dimensional crack can be shown to be:

$$\begin{aligned} E_y^{n+1}(I, J, K) &= E_y^n(I, J, K) + \frac{\Delta t}{\epsilon_0} (\text{Factor}) * \\ &\quad \left\{ [H_x^{n+1/2}(I, J, K) - H_{xc}(I, J)] \Delta x \right. \\ &\quad \left. + [H_z^{n+1/2}(I-1, J, K) - H_z^{n+1/2}(I, J, K)] \Delta z \right\} \quad (6.19) \end{aligned}$$

$$\begin{aligned} \text{where Factor} &= \frac{1 + \frac{\langle f(0, y, 0) \rangle}{1 - f(0, -w/2, 0)}}{\frac{\Delta y + d}{2} + \frac{\Delta z^2}{8d} + \frac{3d}{8} + \frac{\langle f(0, 0, z) \rangle \left(\frac{\Delta z + d}{2}\right)}{1 - f(0, -w/2, 0)}} \end{aligned}$$

Once the correct value of the E_y field is estimated in the FDTD code, then application of Faraday's law over contour C_1 (see figure 6.12) will correctly update the x-component of the magnetic field above the crack. The remaining of the fields are updated as in the conductor-backed dielectric case.

The implementation of the three-dimensional crack equations in the FDTD code is a topic of ongoing research, as well as improvements in the existing theoretical model. Other methods that can be used to validate the crack results are also being considered. Among these are the brute force FDTD method for three-dimensional structures, and the geometrical theory of diffraction (GTD). Also, experimental results (measurements) from three-dimensional dielectric structures is another possibility.

Chapter 7: Conclusions

The intent of this work was to use the Finite-Difference Time-Domain (FDTD) technique to model scattering of relatively thin dielectric structures. These structures included thin dielectric sheets, conductor-backed dielectric sheets, and conductor-backed dielectric sheets containing cracks in the dielectric material.

The near-fields given by the FDTD technique were extrapolated to far-fields using a frequency-domain near-field to far-field transformation. The amplitude and phase of the fields were estimated using a least squares estimation method. The maximum error of the near-field to far-field transformation was found to be 2.0%. This error, corresponding to a standard FDTD cell size of $\lambda/10$, was found by simulating the far field radiation of an infinitely long filament of constant a-c current. As the cell size of the FDTD grid decreases, the numerical error decreases.

Two approaches were applied to model dielectric structures. First, the FDTD was applied in a brute force method whereby very small unit cells are used to model relatively thin dielectric structures. When compared to the MoM, the brute force method was very accurate in modeling lossless and lossy, thin dielectric sheets. In order to improve the computational efficiency of the brute force method, the thin equation approach was used.

In modeling thin dielectric sheets, the thin equation approach produced fair agreement with the MoM results for TM polarization. The results for TE polarization using the thin equation approach compared well with the brute force method results. The two methods demonstrated excellent agreement both in the near-fields and far-fields.

Modeling of conductor-backed dielectric slabs is done accurately using both the brute force method and the thin equation approach. This is mainly due to the fact that the dominant scatterer in this case is the perfect conductor whose effect is accounted for exactly by both methods. But the fact that good results were obtained in the near-fields of the thin conductor-backed dielectric slab prompted us to extend this analysis to structures that contain cracks in the dielectric material. New equations were derived to model the tangential electric field perturbation within the cell containing the crack, while retaining the same equations as in the conductor backed dielectric case for the rest of the FDTD unit cells.

The effect of a crack on the overall RCS pattern of a two-dimensional conductor backed dielectric slab was examined using the brute force method. It was observed that when the sizes of the crack are bigger than $\lambda/20$, the crack affects the RCS pattern. A crack in the dielectric

material of thickness $\lambda/5$ and width $\lambda/10$ can reduce the RCS by at least 2 dBsm, when TE polarization at oblique incident angle (45 degrees) is used. While the RCS pattern decreased at the mainlobe, the opposite effect was exhibited at its sidelobes. If the crack is very small, its effect on the far field radiation of the conductor backed dielectric structure is insignificant. However, a large perturbation in the near fields is obtained. Particularly, the crack enhances the tangential electric fields exactly on top of it and produces a static dipole effect in its vicinity. For some crack geometries, the tangential electric field on the top of the crack was found to be twice the amplitude of the field that is produced when the crack is not present.

Using the thin equation approach, it was found that the near fields of a conductor backed dielectric slab containing a crack can be modeled with an error of as little as 2.34% when the crack is relatively thin compared to the unit cell of the FDTD grid. The small error found in this case prompted us to extend this analysis to model three-dimensional conductor backed dielectric slabs with cracks.

In this way, scattering from dielectric structures up to 25λ in extent can be examined using the two-dimensional FDTD code. The thickness of the dielectric coating can extend from few wavelengths to as little as $\lambda/100$. Cracks of very small size in the dielectric can be modeled with the thin equation approach. If the cracks become large, the brute force method is applied to study their scattering behavior. For three-dimensional structures smaller electrical sizes can be handled because of the increased requirements for storage and execution time.

Appendix

A. Derivation of the Functions $f(x,0)$, $f(0,y)$, and $f(-w/2,0)$

For a two dimensional crack the function $df(x,y)$ was defined as:

$$df(x,y) = \frac{\epsilon_r - 1}{2\pi} \frac{\left(1 + \frac{y'}{d}\right) (x - x') dy'}{[(x - x')^2 + (y - y')^2]} \quad (A.1)$$

In order to find $f(x,y)$, the function $df(x,y)$ must be integrated over the charge distribution on the walls of the crack, including the images due to the presence of the perfect conductor.

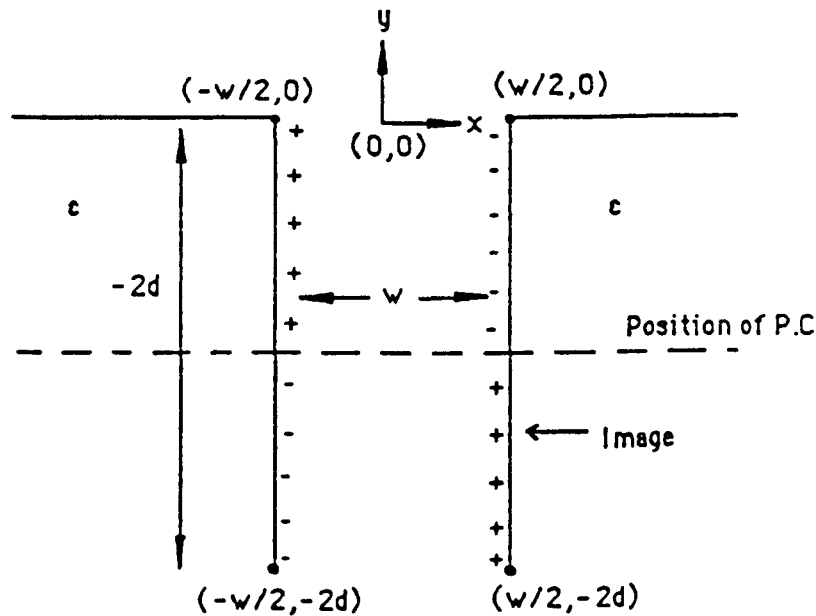


Figure A.1 Integration region for the calculation of $f(x,y)$.

Therefore, in an integral form the function $f(x,y)$ can be expressed as follows:

$$f(x,y) = \int_{\text{over charge}} df(x,y) dy' \quad (\text{A.2})$$

The charge distribution, including the images due to the perfect conductor, is shown in figure A.1. To find the function $f(x,0)$, we integrate $df(x,0)$ as described by equation A.1 over the charge distribution of figure A.1. Expressing the integral in two parts, one corresponding to the distribution on the left crack wall, and the other to the right crack wall, one obtains:

$$f(x,0) = \frac{\epsilon_r - 1}{2\pi} \left\{ \int_0^{-2d} \frac{\left(1 + \frac{y'}{d}\right) \left(x + \frac{w}{2}\right)}{\left(x + \frac{w}{2}\right)^2 + (y')^2} (-dy') - \int_0^{-2d} \frac{\left(1 + \frac{y'}{d}\right) \left(x - \frac{w}{2}\right)}{\left(x - \frac{w}{2}\right)^2 + (y')^2} (-dy') \right\}. \quad (\text{A.3})$$

$$\begin{aligned} \text{Let, } I_1 &= \int_0^{-2d} \frac{\left(1 + \frac{y'}{d}\right) \left(x - \frac{w}{2}\right)}{\left(x - \frac{w}{2}\right)^2 + (y')^2} (dy') \\ &= \left(x - \frac{w}{2}\right) \left\{ \int_0^{-2d} \frac{dy'}{\left(x - \frac{w}{2}\right)^2 + (y')^2} + \frac{1}{2d} \int_0^{-2d} \frac{2y' dy'}{\left(x - \frac{w}{2}\right)^2 + (y')^2} \right\} \\ &= \left(x - \frac{w}{2}\right) \left\{ \frac{1}{x - \frac{w}{2}} \tan^{-1} \left(\frac{y'}{x - \frac{w}{2}} \right) + \frac{1}{2d} \ln \left[\left(x - \frac{w}{2}\right)^2 + (y')^2 \right] \right\} \Bigg|_0^{-2d} \\ &= \left(x - \frac{w}{2}\right) \left\{ \frac{1}{x - \frac{w}{2}} \tan^{-1} \left(\frac{-2d}{x - \frac{w}{2}} \right) + \frac{1}{2d} \ln \left[\frac{\left(x - \frac{w}{2}\right)^2 + 4d^2}{\left(x - \frac{w}{2}\right)^2} \right] \right\}. \end{aligned}$$

Similarly,

$$I_2 = \int_0^{-2d} \frac{\left(1 + \frac{y'}{d}\right) \left(x + \frac{w}{2}\right)}{\left(x + \frac{w}{2}\right)^2 + (y')^2} (-dy')$$

$$= \left(x + \frac{w}{2}\right) \left\{ \frac{1}{x + \frac{w}{2}} \tan^{-1} \left(\frac{-2d}{x + \frac{w}{2}} \right) + \frac{1}{2d} \operatorname{Ln} \left[\frac{\left(x + \frac{w}{2}\right) + 4d^2}{\left(x + \frac{w}{2}\right)^2} \right] \right\}$$

Replacing I_1 and I_2 into equation (A.3), and simplifying, the resulting equation for $f(x,0)$ is as follows:

$$f(x,0) = \frac{c_r - 1}{2\pi} \left\{ \tan^{-1} \left(\frac{-2d}{x - \frac{w}{2}} \right) + \frac{\left(x - \frac{w}{2}\right)}{2d} \operatorname{Ln} \left[\frac{\left(x - \frac{w}{2}\right) + 4d^2}{\left(x - \frac{w}{2}\right)^2} \right] \right.$$

$$\left. - \tan^{-1} \left(\frac{-2d}{x + \frac{w}{2}} \right) + \frac{\left(x + \frac{w}{2}\right)}{2d} \operatorname{Ln} \left[\frac{\left(x - \frac{w}{2}\right) + 4d^2}{\left(x - \frac{w}{2}\right)^2} \right] \right\} \quad (\text{A.4})$$

The average value of $f(x,0)$, i.e. $\langle f(x,0) \rangle$, over the length of the unit cell can be found using numerical integration. At $x = -w/2$ the function $f(x,0)$ is discontinuous. Its value at this point has to be estimated in closed form using the lefthand limit with x approaching $-w/2$. This value of $f(-w/2,0)$ can be shown to be equal to:

$$f(-w/2,0) = \lim_{x \rightarrow -w/2^-} f(x,0) = \frac{c_r - 1}{2\pi} \left[\tan^{-1} \left(\frac{2d}{w} \right) - \frac{w}{2d} \operatorname{Ln} \left(\frac{w^2 + 4d^2}{w^2} \right) - \frac{\pi}{2} \right] \quad (\text{A.5})$$

The function $f(0,y)$ can be found in a similar manner as $f(x,0)$ by integrating a slightly different function. It can be shown that $f(0,y)$ equals to:

$$f(0,y) = \frac{\epsilon_r - 1}{2\pi} \left\{ 2 \left(1 + \frac{y}{d} \right) \left[\tan^{-1} \left(\frac{y+2d}{\frac{w}{2}} \right) - \tan^{-1} \left(\frac{y}{\frac{w}{2}} \right) \right] + \frac{w}{2d} \ln \left[\frac{\left(\frac{w}{2} \right)^2 + y^2}{\left(\frac{w}{2} \right)^2 + (y+2d)^2} \right] \right\} \quad (\text{A.6})$$

The average value of $f(0,y)$, i.e. $\langle f(0,y) \rangle$, can also be found using numerical integration.

References

1. A. Taflove, K.R. Umashankar, B. Beker, F. Harfoush, "Detailed FD-TD Analysis of Electromagnetic Fields Penetrating Narrow Slots and Lapped Joints in Thick Conducting Screens," IEEE Transactions of Antennas and Propagation, Vol. AP-36, No. 2, pp. 247-257, February 1988
2. K. R. Demarest, "FD-TD Scattering From Apertures", RSL Technical Report 5496-1, Radar Systems and Remote Sensing Laboratory, The University of Kansas, Lawrence, March 1988
3. K. R. Demarest, J. Huang, D. Long, "Scattering From Thin Dielectric Plates Using the Finite-Difference Time-Domain Technique," 1988 URSI Radio Science Meeting, Syracuse, New York, June 6-10.
4. K. R. Demarest, D. Long, and P. Tirkas, "Efficient Modeling of Thin Dielectric Structures Using the Finite-Difference Time-Domain Technique," The Fifth Annual Review of Progress in Applied Computational Electromagnetics, Naval Postgraduate School, Monterey, California, March 1989
5. P. Tirkas, "Modeling of Thin Dielectric Structures Using the Finite-Element Time-Domain Technique," Ph.D. thesis, The University of Kansas, 1989
6. D. Long, "User's Guide for FDTD-3D ", RSL Technical Report 8090-2, Radar Systems and Remote Sensing Laboratory, The University of Kansas. In preparation.
7. R. F. Harrington, Field Computation by Moment Methods, MacMillan, New York, 1968.
8. K. S. Yee, "Numerical Solution of Initial Boundary Value Problems Involving Maxwell's Equations in Isotropic Media," IEEE Transactions on Antennas and Propagation, Vol. AP-14, No. 3, pp. 302-307, May 1966.
9. D. T. Borruip, D. M. Sullivan, and O. P. Gandhi, "Comparison of the FFT Conjugate Gradient Method and the Finite-Difference Time-Domain Method for the 2-D Absorption Problem," IEEE Transactions on Microwave Theory and Techniques, Vol. MTT-35, No. 4, pp. 383-395, April 1987.

10. K. S. Kunz and L. Simpson, "A Technique for Increasing the Resolution of Finite-Difference Solutions of the Maxwell Equation," IEEE Transactions on Electromagnetic Compatibility, Vol. EMC-23, No. 4, pp. 419-422, November 1981.
11. K. R. Demarest, "A Finite-Difference Time-Domain Technique For Modeling Narrow Apertures in Conducting Scatterers," IEEE Transactions on Antennas and Propagation, Vol. AP-35, No. 7, pp. 826-831, July 1987.
12. R. Holland, and L. Simpson, "Finite-Difference Analysis of EMP Coupling to Thin Struts and Wires," IEEE Transactions on Electromagnetic Compatibility, Vol. EMC-23, No. 2, pp. 88-97, May 1982.
13. G. Mur, "Absorbing Boundary Conditions for the Finite-Difference Approximation of the Time-Domain Electromagnetic Field Equations," IEEE Transactions on Electromagnetic Compatibility, Vol. EMC-23, No. 4, pp. 377-382, November 1981.
14. Allen Taflove, and Korada Umashankar, "The Finite-Difference Time-Domain (FDTD) Method for Electromagnetic Wave Scattering and Interaction Problems," Draft Report to Lawrence Livermore National Laboratory, March 1987.
15. Roger F. Harrington, Time-Harmonic Electromagnetic Fields, McGraw Hill Book Company, New York, 1961.
16. Charles L. Britt, "Solution of Electromagnetic Scattering Problems Using Time Domain Techniques," Final Report, Contract NAS1-17639 to NASA, Langley Research Center.
17. Peter Bloomfield, Fourier Analysis of Time Series: An Introduction, John Wiley & Sons , New York, 1976.
18. M. G. Andreasen, "Scattering from Bodies of Revolution," IEEE Transactions on Antennas and Propagation, Vol. AP-13, No. 3, pp. 303-310, March 1965.
19. J. H. Richmond, "Scattering by a Dielectric Cylinder of Arbitrary Cross Section Shape," IEEE Transactions on Antennas and Propagation, Vol. AP-13, No. 3, pp. 334-341, March 1966.
20. J. H. Richmond, "TE Wave Scattering by a Dielectric Cylinder of Arbitrary Cross Section Shape," IEEE Transactions on Antennas and Propagation, Vol. AP-14, No. 7, pp. 460-464, July 1966.

21. T. K. Sarkar, E. Arvas, and S. Ponnappalli, "Electromagnetic Scattering from Dielectric Bodies," *IEEE Transactions on Antennas and Propagation*, Vol. AP-37, No. 5, pp. 673-676, May 1989.
22. D. E. Livesay and K. M. Chen, "Electromagnetic Fields Induced Inside Arbitrarily Shaped Biological Bodies," *IEEE Transactions on Microwave Theory and Techniques*, Vol. MTT-22, No. 12, pp. 1273-1280, December 1974.
23. D. H. Schaubert, D. R. Wilton, and A. W. Glisson, "Tetrahedral Modeling Method for Electromagnetic Scattering by Arbitrarily Shaped Inhomogeneous Dielectric Bodies," *IEEE Transactions on Antennas and Propagation*, Vol. AP-32, No. 1, pp. 77-85, January 1984.
24. K. Umashankar, A. Taflove, and S. M. Rao, "Electromagnetic Scattering by Arbitrary Shaped Three Dimensional Homogeneous Lossy Dielectric Objects," *IEEE Transactions on Antennas and Propagation*, Vol. AP-34, No. 6, pp.758-766, June 1986.
25. R. J. Pogorzelski, "On the Numerical Computation of Scattering from Inhomogeneous Penetrable Objects," *IEEE Transactions on Antennas and Propagation*, Vo. AP-26, No. 7, pp. 616-618, July 1978.
26. Asoke K. Bhattacharyya, and S. K. Tandon, "Radar Cross Section of Planar Structure Coated With a Lossy Dielectric," *IEEE Transactions on Antennas and Propagation*, Vol. Ap-32, No. 9, pp. 1003-1007, September 1984.
27. C. H. Tang, "Bascattering from Dielectric-Coated Infinite Cylindrical Obstacles," *Journal of Applied Physics*, Vol. 28, No. 5, pp. 628-633, May 1957.
28. G. T. Ruck, Ed., Radar Cross-Section Handbook, Vol. 2, New York, Plenum, 1970.
29. M. A. Ricoy and J. L. Volakis, "Integral Equations With Reduced Unknouwns for the Simulation of Two-Dimensional Composite Structures," *IEEE Transsactions on Antennas and Propagation*, Vol. AP-37, No. 3, pp. 362-372, March 1989.
30. Jack Richmond, "Scattering by Thin Dielectric Strips," Technical Report 711930-7, Contract No. NSG 1613, Electroscience Laboratory, The Ohio State University, August 1983
31. Jian-Ming Jin and Valtis Liepas, "Application of Hybrid Finite Element Method to Electromagnetic Scattering from Coated Cylinders," *IEEE Transactions on Antennas and Propagation*, Vol. AP-36, No. 1, pp. 50-54, January 1988.



MISSION
of
Rome Air Development Center

RADC plans and executes research, development, test and selected acquisition programs in support of Command, Control, Communications and Intelligence (C³I) activities. Technical and engineering support within areas of competence is provided to ESD Program Offices (POs) and other ESD elements to perform effective acquisition of C³I systems. The areas of technical competence include communications, command and control, battle management information processing, surveillance sensors, intelligence data collection and handling, solid state sciences, electromagnetics, and propagation, and electronic reliability/maintainability and compatibility.